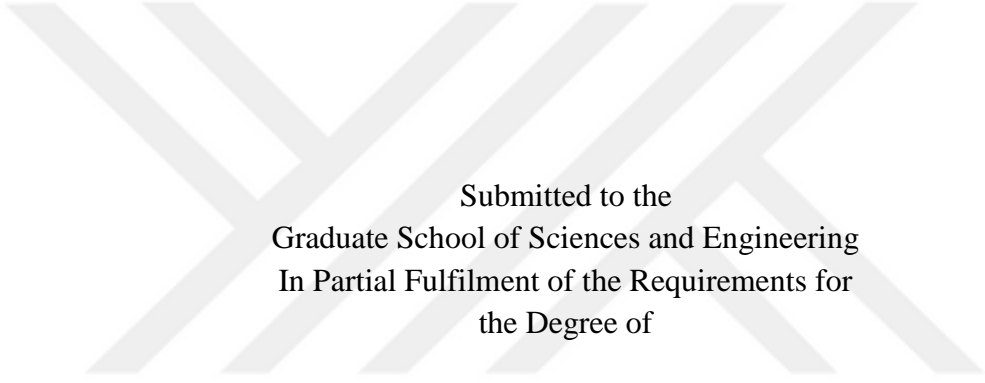


DETERMINING THERMAL COMFORT IN BUILT ENVIRONMENT USING COMPUTATIONAL FLUID DYNAMICS SIMULATIONS

A MSc Thesis

by

Güven Fidan



Submitted to the
Graduate School of Sciences and Engineering
In Partial Fulfilment of the Requirements for
the Degree of

Master of Science
in the
Department of Mechanical Engineering

Özyeğin University

June 2017

Copyright© 2017 by Güven Fidan

DETERMINING THERMAL COMFORT IN BUILT ENVIRONMENT USING COMPUTATIONAL FLUID DYNAMICS SIMULATIONS

Approved by:

Professor M. Pınar Mengüç, Advisor
Department of Mechanical Engineering
Özyeğin University

Assoc. Prof. Özgür Ertunç
Department of Mechanical Engineering
Özyeğin University

Assoc. Prof. Şule Kapkın,
Department of Mechanical Engineering
İstanbul University

Date Approved: 08 June 2017

DEDICATION



To my family and Azadeh

ACKNOWLEDGEMENTS

This work was not possible without the help and support of many people in my life. First, I would like to express my gratitude to my supervisor, Prof. M.P. Mengüç for believing in me and supporting me very patiently during all years of my studies.

I would also like to thank my friend, Dr. Azadeh Didari for motivating me in the final stages of my thesis, and for her help with the edition of the thesis.

I would also like to thank my family for all of their support and love during my MSc studies.

ABSTRACT

In this thesis, three-dimensional time-dependent Thermal Comfort (TC) conditions in an occupied room is investigated and determined. The room is considered with furniture of varying materials (i.e. steel, wood, etc.) and under incident solar radiation. A Computational Fluid Dynamics (CFD) method, FloEFD software was used to enable designers to perform accurate and fast analysis. This computational tool allows detailed 3D visualizations and inclusion of geometrical details of the diffusers of the HVAC system. To determine the required TC conditions such as the I) air distribution, II) indoor temperature profiles, III) humidity, and IV) the mean radiant temperature profiles, the CFD method is used. This work is significantly different from the earlier works as it includes the spectral surface emissivity of the existing materials in the room and the spectral transmissivity of windows' glasses. In the analyses, both conduction and spectral radiation, which have led to calculate more accurate and detailed TC conditions, are considered. The mentioned analyses reach agreement with the experimental data obtained in the room. The visualization of four parameters is done for different scenarios by evaluation of the change of the window properties inside the room and the HVAC diffuser. Subsequently, these values were interpreted as PMV and PPD for thermal comfort with Fanger method, depending on human clothing and metabolic rate. The completion of the comparison scenarios during the sunshine time of 8 hours allowed considering the warm-up period of the materials in the room. Therefore, it has come to the conclusion that the long-wave radiation of heated materials can affect TC, not just direct radiation of sun. With the new diffuser scenario, the occupant is locally, positively influenced by the thermal comfort due to blowing the incoming air directly into the seating area. However, with this secondary diffuser, it has

been found that the thermal comfort decreases more rapidly in the comfort zone during the 8 hours. The reason for this is that the primary diffuser in which the comparison is made delayed the heating of the material by blowing directly into the glass and the wall. The findings of this research can be used to evaluate TC in big glass façade cladding spaces.



ÖZETÇE

Bu tez çalışmasında, içinde çeşitli eşyaların bulunduğu bir oda için, ısı konfor seviyesinin belirlenebilmesi adına, zamana bağlı olarak üç boyutlu hazırlanmış modelin Hesaplama Akışkanlar Dinamiği (HAD) yöntemi kullanılarak, doğrudan güneşlenmeye maruz kaldığı zaman diliminde, malzemelerin ısı kapasitesi de hesaba katılarak, analiz tamamlanmıştır. HAD hesaplamaları için FloEFD yazılımı tercih edilmiştir. FloEFD tasarımcılar için hızlı ve güvenilir sonuçlar veren, ileri seviye HAD yazılım programıdır. Bu hesaplama aracı, iklimlendirme ve havalandırma cihazlarının oda içinde hava dağıtımında etkin olan kısımlarının modellenerek, akışın üç boyutlu görselleştirmesine imkanı vermektedir. Isı konforun yorumlanması için gerekli parametreler olan, I) havanın dağılımı, II) havanın sıcaklık profili, III) nemi ve IV) ortalama ışınım sıcaklığı bu vasıta ile hesaplamalara dahil edilebilmiştir. Bu çalışmada yapılan önemli farklılık ise ortamdaki malzemelerin yüzey yayıcılık değerlerinin ve camların ışınım geçirgenlik değerlerinin tayfsal olarak ele alınmasıdır. Kullanılan malzemelerin fiziksel özelliklerinin detaylı olarak yazılıma dâhil edilmesiyle, simülasyon sonuçları ve oda içinde belirlenmiş zamanda tamamlanan ölçüm sonuçları, karşılaştırıldığında yüksek tutarlılık göstermiştir. Değişik pencere özelliklerinin ve HVAC elemanı olan difüzörün farklı senaryolar altında değerlendirilmesi dört farklı parametrenin görselleştirilmesiyle yapılmıştır. Akabinde, ısı konfor yorumu için, bu dört parametre insanların giydiği kıyafetlerin bilgisinin ve metabolik üretim değerlerinin Fanger Metod'la PMV ve PPD parametrelerine dönüştürülmesi yapılmıştır. Tamamlanan karşılaştırma analizleri, güneşlenmenin olduğu 8 saat süresince gerçekleştirilerek, oda içindeki malzemelerin sıcaklığının artmasının göz önünde bulundurulması sağlanmıştır. Böylece ısı konforun etkilenmesinin sadece, doğrudan

gelen güneş ışınımına bağlı değil, ısınan malzemelerin uzun dalga boylarıyla yaydığı ışınım sebebiyle de olduğu sonucu çıkarılmıştır. Yeni difüzör senaryosunda, gelen havanın doğrudan oturma alanına üflenmesi sayesinde kullanıcı ısı konfor açısından lokal olarak olumlu etkilenmiştir. Fakat görülmüştür ki, 8 saat süresince konfor zonunda ısı konfor daha hızlı azalmaktadır. Bunun sebebi ise kıyaslamanın yapıldığı birincil difüzörün, doğrudan camalara ve duvara üfleme yaparak, malzemenin ısınmasını geciktirmesidir. Bu çalışmanın sonucunda elde edilenler, büyük cam cephe giydirmeli mahaller için ısı konforun değerlendirilmesinde kullanılabilir.



LIST OF TABLES

Table 1, Physical properties of materials. 17

Table 2, Physical properties of materials. 40

Table 3, Radiative properties of glasses. 44

Table 4, Number of the cell for mesh independency. 58

Table 5, Convective heat transfer coefficient comparison for whole standing body in still air ($<0.1\text{ m/s}$). 62

Table 6, Comparison scenarios are detailed with variable materials. 71

Table 7, Comfort zone general distance from the room boundaries. 73

LIST OF FIGURES

Figure 1.1 , Mechanisms of heat transfer from body to environment.	6
Figure 1.2 , P.O. Fanger thermal sensation range.	6
Figure 1.3 PMV vs. PPD graph. Point A(-1,26) shows that when sensible temperature is slightly cool, 26% of people experienced thermal discomfort. Similarly, at point B(2,76) when the sensible temperature 76% of people reported thermal discomfort.	8
Figure 2.1 , Surface interact with incident radiation.	25
Figure 2.2 , Radiative heat transfer in participating medium.	21
Figure 2.3 , The schematic definition for Q^{net}	28
Figure 2.4 , Absorbing and reflecting the coming radiation in interface point by the medium having absorption; depiction Snell's law.	27
Figure 2.5 Radiation transmission through a transparent medium.	32
Figure 2.6 Reflection of radiation at a given surface.	33
Figure 2.7 Diffuse Reflection from a Lambertian surface.	34
Figure 2.8 Ideal specular reflection.	34
Figure 2.9 Spectrum of solar light on Earth	36
Figure 3.1 Occupant perspective of the room.	40
Figure 3.2 Top view of the room model.	40
Figure 3.3 Sectional view of the room model.	40
Figure 3.4 Three dimensional solid body view of the room.	41
Figure 3.5 Location of the blower diffuser in the room and detail picture.	42
Figure 3.6 Spectral emissivity of surfaces was applied steel sheet metal, brown carpet, wood, the white paint	45
Figure 3.7 From the different perspective, notation of opaque surfaces.	46

Figure 3.8 Glazing from external to internal for the total thickness of glasses is 24mm.....	48
Figure 3.9 Spectral distribution of solar transmissivity for three glasses.	49
Figure 3.10 Spectral distribution of absorption coefficient for three glasses.	49
Figure 3.11 Velocity measurement on diffuser	50
Figure 3.12 Temperature measurement on diffuser.	51
Figure 3.13 Relative humidity measurement on diffuser.	51
Figure 4.1 Flow chart of simulation steps.	52
Figure 4.2 Flow rate boundary condition on diffuser.	54
Figure 4.3 Definition of air flow rate on diffusers.	54
Figure 4.4 Definition of environmental pressure on door surface.	55
Figure 4.5 Boundary conditions on walls.	56
Figure 4.6 Outside wind speed data measured on March 3.	56
Figure 4.7 Solar heat flux direction and orientation in the analysis room	57
Figure 4.8 Solar heat flux data which was collected by the device on the roof of the building on horizontal plane. It was obtained by the university weather data station. .	57
Figure 4.9 Solid, fluid and solid-fluid cells in the computational domain.	59
Figure 4.10 Cross-sectional mesh distribution in the room. Results of mesh dependency were tested and this mesh size accepted for analysis in the room and close to the diffuser blades.	60
Figure 4.11 The cross-sectional view of the mesh and surface mesh distribution of diffuser. From coarse mesh to very fine mesh, number of cells were increased between the diffuser blades. Validation study shows the importance of this improvement to obtain meaningful velocity consistency between experimental and simulations results.	61

Figure 4.12 The convective heat transfer coefficient on human body, under the still air condition (air velocity near the body is less than 0.1 <i>m/s</i>) in room environment.	63
Figure 4.13 Measurement of velocity at diffuser level.	64
Figure 4.14 Air velocity measurements at diffuser height.	64
Figure 4.15 Cross-section side view on diffuser and the comparison of velocity distribution with different mesh types, coarse mesh to very fine mesh.	65
Figure 4.16 Measurement of velocity at the seat location.	66
Figure 4.17 Cross-sectional side view on diffuser, comparison of velocity distribution with different mesh types.	67
Figure 4.18 Comparison of experimental and simulation results for temperature of the surface of glasses.	69
Figure 5.1 Time period of applied flow freezing approach. It shows with short lines, 5 minutes for solving the all governing equations and long lines 30 minutes for solving only the governing of energy equations. This loop was repeated during the 8 hours in all scenarios.	71
Figure 5.2 Maximum, minimum and average long term outdoor air temperature for Istanbul from 2009 to 2017.	72
Figure 5.3 Comfort zone virtual boundaries in the test room.	73
Figure 5.4 There are two chairs in this room and occupants generally stay in these locations. One of them is Zone 1 and other is the Zone 2.	74
Figure 5.5 New diffuser type and air flow distribution. The angle of blades of diffuser gives advantages to blow the air directly to occupant's zone.	76
Figure 5.6 Results of four different scenarios with average velocity fluctuation in comfort Zone 1 from 09:00 to 17:00. Velocity fluctuations of first three scenarios' are close to each other, but intensity of new designed diffuser is higher	77

Figure 5.7 Results of four different scenarios with average air temperature in comfort Zone 1 from 09:00 to 17:00. 77

Figure 5.8 Results of four different scenarios with average mean radiant temperature in comfort Zone 1 from 09:00 to 17:00. Glass type and diffuser conditions for scenario 3 and 4 generate similar results for mean radiant temperature, but this value is much higher than others. 78

Figure 5.9 Results of four different scenarios with average operative temperature in comfort Zone 1 from 09:00 to 17:00. Operative temperatures have a linear relationship with mean radiant temperature in the scenario 1 and 2. 78

Figure 5.10 Results of four different scenarios with average predicted mean vote in comfort Zone 1 from 09:00 to 14:30. PMV values help to understand sensation range between determined scenarios. Feeling hot in comfort Zone 1 after 14.30 to 17.00 shows that PMV values don't correspond to any meaningful range on TC for Fanger Method. 79

Figure 5.11 Results of four different scenarios with Predicted Percent Dissatisfied in comfort Zone 1 from 09:00 to 14:00. Predicted Percent Dissatisfied show that in comfort Zone 1, 100% of people are not satisfied after 14.00 in all scenarios. 79

Figure 5.12 Results of four different scenarios with average velocity fluctuating in volume of comfort Zone 2 from 09:00 to 17:00. Intensity of velocity in all scenarios are closer to each other. Zone 2 was able to take advantage of speed of air intensity reasonably more than comfort Zone 1. 80

Figure 5.13 Results of four different scenarios with average air temperature in comfort Zone 2 from 09:00 to 17:00. Comparison of scenarios show that results of air temperature is similar in comfort zones with different scenarios. 81

Figure 5.14 Results of four different scenarios with average mean radiant temperature

in comfort Zone 2 from 09:00 to 17:00. Glass type and diffuser conditions for scenario 3 and 4 generate similar results for mean radiant temperature, but these values are much higher than other scenarios. 81

Figure 5.15 Results of four different scenarios with average operative temperature in comfort Zone 2 from 09:00 to 17:00. Operative temperature is lower than comfort Zone 1, especially for the scenarios 3 and 4. 82

Figure 5.16 Results of four different scenarios with average predicted mean vote in comfort Zone 1 from 09:00 to 14:00. Predicted mean vote results are higher than the limit of Fanger comfort range after 14.00 in all scenarios. 82

Figure 5.17 Results of four different scenarios with Predicted Percentage of Dissatisfied in comfort Zone 2 from 09:00 to 14:00. Higher PMV results generate higher dissatisfied sensation in comfort Zone 2 as Zone 1. 83

Figure 5.18 Transmissivity of glass materials and the relative spectrum of solar radiation. It shows that selected Glass 2 and relative solar spectrum have the same level of distribution. 84

Figure 5.19 Variation of the average mean radiant temperature on the wall and glass surface from 09:00 to 17:00 in demonstration room. 86

Figure 5.20 Variation of the temperature on the surface of solid material from 09:00 to 17:00. Comparison of the temperature differences results with the current diffuser and the designed new diffuser. 87

Figure 5.21 Temperature on the inside wall and glass surfaces from 09:00 to 17:00. New design diffuser effects on these surfaces from the perspective of temperature. 88

NOMENCLATURE

u : Fluid velocity [m/s]

ρ : Fluid density [kg/m³]

g : Gravitational acceleration component [m/s²]

h : Thermal enthalpy [kJ]

Q_H : Heat source per unit volume [W/m³]

τ_{ik} : Viscous shear stress tensor [N/m²]

q_i : Diffusive heat flux [W/m²]

δ_{ij} : Kronecker delta function

μ : Dynamic viscosity coefficient [Ns/m²]

μ_t : Turbulent eddy viscosity coefficient [m²/s]

k : Turbulent kinetic energy [J/kg]

y : Distance from the wall [m]

Pr : Prandtl number

Le : Lewis number

ε : Emissivity

σ : Stefan-Boltzmann constant [W/m²K⁴]

T : Temperature of surface [C°]

Q_s^{in} : Incident solar radiation [W/m²]

Q_s^{source} : Radiation arriving at the surface from solar source [W/m²]

\vec{s} : Discrete directions [sr]

\vec{r} : Position vector [sr]

RL : Defined discretization level

I_b : Black body radiation intensity [W/m²]

I_s : Black body radiation intensity [W/m²]

α : Absorption coefficient [m^{-1}]

n : Refractive index

I_0 : Initial intensity [W/m^2]

φ : Azimuthal angle measured about the surface normal

$L_r(\theta_r, \varphi_r)$: Reflected radiance [$\text{W}/\text{sr}/\text{m}^2$]

$L_i(\theta_i, \varphi_i)$: Incident Radiance [$\text{W}/\text{sr}/\text{m}^2$]

$\rho_{bd}(\theta_i, \varphi_i, \theta_r, \varphi_r)$: Bi-directional reflectance distribution function [sr^{-1}]

ρ_d : Diffuse Reflection

ρ_s : Specular Reflectance

I_{λ_i} : Radiation Intensity in the i -th spectrum band

$I_{b\lambda_i}$: Intensity of the blackbody radiation in the i -th spectrum band

$k_{\lambda,i}$: Absorption Coefficient in the i -th spectrum band

M : Metabolic Rate [W/m^2]

W : External Work [W/m^2]

I_{cl} : Clothing thermal resistance [$\text{m}^2\text{K}/\text{W}$]

f_{cl} : Ratio of clothed surface area to nude surface [m^2]

T_a : Air temperature [$^{\circ}\text{C}$]

T_r : Mean radiant temperature [$^{\circ}\text{C}$]

V : Relative air velocity [m/s]

p_a : Water vapor partial pressure [Pa]

h_{cl} : Convective heat transfer coefficient [$\text{W}/\text{m}^2\text{K}$]

T_{cl} : Clothing surface temperature [$^{\circ}\text{C}$]

TABLE OF CONTENTS

DEDICATION.....	iii
ACKNOWLEDGEMENTS	iv
ABSTRACT	v
ÖZETÇE	vii
LIST OF TABLES.....	ix
LIST OF FIGURES	x
NOMENCLATURE	xv
TABLE OF CONTENTS.....	1
CHAPTER I.....	3
INTRODUCTION.....	3
1.1 <i>General Background</i>	3
1.2 <i>Literature Review</i>	5
1.3 <i>Outline of Thesis</i>	17
CHAPTER II.....	19
FUNDAMENTAL AND THEORETICAL ASPECT	19
2.1. <i>Governing Equations for Air Flow and Heat Transfer</i>	19
2.1.1. <i>Turbulence Model k-epsilon:</i>	21
2.2 <i>Thermal Radiative Transfer</i>	24
2.2.1 <i>Discrete Transfer Model (DT)</i>	27
2.2.2 <i>Discrete Ordinates Model (DO)</i>	29
2.2.3 <i>Absorption and Transmission</i>	30
2.2.4 <i>Reflection</i>	32
2.2.5 <i>Radiative Heat Transfer Equation with Radiation Spectrum:</i>	35
2.2.6 <i>Solar Load Model and Environment Temperature</i>	35
2.3. <i>Thermal Comfort Equations of Povl Ole (P.O.) Fanger</i>	37
CHAPTER III	39
MODEL DEVELOPMENT AND NUMERICAL SIMULATIONS	39
3.1. <i>Definition of HVAC System</i>	41
3.2. <i>Details of the Measurement Devices</i>	42
3.3. <i>Types and Physical Properties of Materials Used in a Room</i>	43
3.3.1. <i>Physical Properties of Window Glasses</i>	47
3.4. <i>Experimental Measurements</i>	50

CHAPTER IV.....	52
SIMULATION STEPS	52
<i>4.1. Benchmark Analysis and Boundary Conditions.....</i>	<i>53</i>
<i>4.1.1. Inlet and Outlet Flow Rates</i>	<i>53</i>
<i>4.1.2. Effect of Environmental Pressure.....</i>	<i>54</i>
<i>4.1.3. Effect of Wall Boundary Conditions.....</i>	<i>55</i>
<i>4.1.4. Effect of Solar Radiation and Environment Temperature</i>	<i>56</i>
<i>4.1.5. Assumptions and Mesh Discretization</i>	<i>58</i>
<i>4.2. Results for Benchmark Simulation and Validations</i>	<i>61</i>
<i>4.2.1. Validation of Results</i>	<i>61</i>
<i>4.2.2. Experimental Results and the Error Rate</i>	<i>63</i>
CHAPTER V.....	69
INVESTIGATION OF THERMAL COMFORT	69
IN DIFFERENT SCENARIOS.....	69
<i>5.1. Assumptions for Boundary Conditions in Summer Time.....</i>	<i>71</i>
<i>5.2. Comfort Zone Specifications</i>	<i>73</i>
<i>5.3. New Diffuser Design for Scenario Four</i>	<i>76</i>
<i>5.4. Comparison of the scenarios in Comfort Zone 1</i>	<i>77</i>
<i>5.5. Comparison of the scenarios in Comfort Zone 2.....</i>	<i>81</i>
<i>5.6. Discussions of Comparison Results</i>	<i>84</i>
CHAPTER VI.....	90
CONCLUDING REMARKS	90
<i>6.1 Conclusion</i>	<i>90</i>
<i>6.2. Future Works</i>	<i>93</i>
BIBLOGRAPHY	94
APPENDIX A.....	100
CONFIGURATOR SOFTWARE AND SOLAR PROPERTIES OF GLASSES	100
APPENDIX B	110
CROSS-SECTIONAL IMAGES IN COMFORT ZONE.....	112

CHAPTER I

INTRODUCTION

1.1 General Background

The rapid increase of urban population and the building concentration within city centers, where people spend most of their time either at their houses or offices, has led into the need for careful consideration of multi-comfort concepts in buildings and cities. Based on a recent EU report, in most countries, including Turkey, about 40% of total energy consumption is due to buildings [1]. Within these buildings, Heating, Ventilating and Air Conditioning (HVAC) systems use 50% of the total existing energy [2],[3]. These findings suggest that the new generation buildings should promote comfortable living conditions, with emphasis on energy efficiency both in construction and operation phases, particularly for better heating and cooling of buildings. To this end obtaining a balance between indoor environmental quality and energy consumption is of vital importance.

There are four different factors which define the best living conditions. These factors are: Thermal Comfort (TC), Indoor Air Quality (IAQ), Visual Comfort (VC) and Acoustic Comfort (AC), which are essential in maintaining a healthy life style of people who live in crowded cities. These factors are not discussed in the design and construction phase of most buildings. In addition, their impact on energy efficient operation of buildings is hardly considered at all.

In this thesis, out of the these four factors, we focus only on thermal comfort, TC. TC is defined by Hensen [4] as “a state in which there are no driving impulses to correct the environment by behaviour”. Similarly, ASHRAE (American Society of

Heating, Refrigerating and Air-Conditioning Engineers) defines TC as “the condition of mind in which satisfaction is expressed with the thermal environment” [5].

In order to achieve a better TC, it is best to modify both active (HVAC) and passive (non-automotive) systems. In order to analyze TC, we can employ analytical, numerical or experimental techniques. Each of these methods has its own pros and cons. In the case of analytical techniques, it is difficult to include all the necessary parameters such as spectral surface characteristics, of walls and windows in the calculations. To use experimental techniques to analyze TC, think that the construction of the building needs to be finished first. In addition, experimental techniques are very costly and case specific. However, it can be considered at the design phase, and for this computational/numerical techniques need to be developed to provide a comprehensive analysis of TC. Computational Fluid Dynamics (CFD) and Computational Heat Transfer (CHT) methodologies are proved to be accurate approaches for general modeling of fluid flow and heat transfer in buildings [6]. Through CFD and CHT, we can take into account all the required calculation parameters, and predict building conditions and comfort level to be achieved starting at early design stages of a building. Furthermore, these approaches can account for air and heat flow distribution patterns, which cannot be evaluated by analytical techniques.

CFD technique has been commonly used for flow distribution analyses in different applications. However, CFD, along with CHT, has not been used widely to predict the airflow distribution patterns and thermal parameters to determine TC in buildings. In this thesis, we outline a comprehensive numerical analysis using CFD/CHT techniques, where we explore the effects of modifying different parameters to achieve the desired TC levels. Particularly, we explore the effects of spectral properties of window glasses in passive systems, and the modifications of the design of

diffusers of the HVAC systems, in active systems. In the next section we will provide a detailed literature survey and cite all the references for the statements we made above.

1.2 Literature Review

When investigating thermal comfort conditions, one may approach the problems from human thermoregulation, adaptive approach point of view and by accounting for the surrounding environmental information about it.

Studies on thermoregulation of human body were considered by Lefevre for the first time about 100 years ago [7]. Thermoregulation is the ability of a living body to maintain its temperature within certain range, even when the surrounding temperature is very different. In thermoregulation, body heat is generated mostly in the deep organs, especially the liver, brain, and heart, and in contraction of skeletal muscles. Humans, along with most mammals, have been able to adapt to a great diversity of climates, including extreme conditions. [7]–[14].

Adaptive approach comes from field studies, having the purpose of analyzing the real acceptableness of thermal environment, which particularly is dependent on the context, the manner of people and their expectations. It is outlined in three categories: behaviour, physiological and psychological adaptation. According to the adaptive approach, people cannot be a passive recipient in a living thermal environment. The environment conditions and thermal requirement of a person interact via multiple feedback loops [15]–[24].

Our focus in this thesis is on the TC of a person within his surrounding environmental. The simulation of TC depends on solving the conservation of energy equation between the environment and human body, for which there is a well-accepted approach [25]. The heat gains and losses from body skin occur by radiation, convection,

conduction, respiration and evaporation as shown in Figure 1.1. Energy balance equation can be expressed in simple term as

$$M-W = E+R+C+K+S$$

where, M is metabolic rate, W is the external work and E, R, C and K are the temperature exchange of evaporation, radiation, convection, conduction and S is the stored temperature energy [26]. This simple equation requires many inputs about the human thermo-regulation system and it can be extendable for solving different methods as analytical, numerical and experimental solutions.

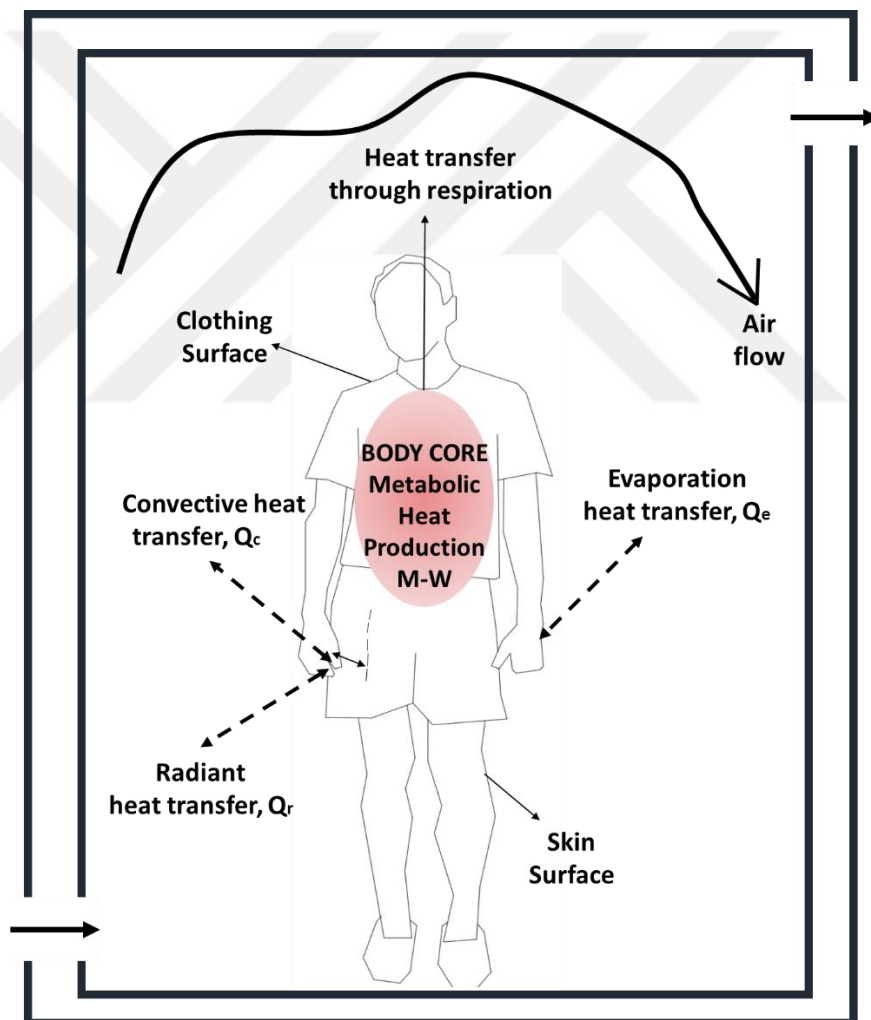


Figure 1.1 Mechanisms of heat transfer from body to environment.

Human body constantly produces heat. While this heat is around 75 W in sleep, it

can rise up to 1000 W during the heavy physical exercises. As this generated heat is transferred to outer environment in a controlled way by radiation, conduction, convection and evaporation, the main aim is to fulfill the requirements for the functioning heat of internal organs. The safe heat difference for the internal organs is maximum 2⁰C. For this reason, human body constantly tries to preserve this heat balance against changes in external environment.

Different methods have been developed for thermal detection and comfort [23]. Along them, Fanger's PMV (Predicted Mean Vote) method is used by the most valid thermal comfort measuring standards (ISO 7730 and ASHRAE 55). The essential differentiating quality of this method is in its capability of static and stable comfort interpretation, solely based on environmental factors. In other words, evaluations are done on the basis of unchanging factors (seasonal clothing; while sitting, walking, sleeping, etc.) as the interactions of the changes in human physiology with the environment are disregarded.

The PMV methodology basically takes six parameters into consideration. While four of them are calculated according to environmental variables (air velocity, temperature, relative humidity and sensible radiation heat), the other two are derived according to human body condition (cloth type and metabolism). Out of these 6 parameters, the environmental variables (4 parameters) are obtained by numerical solutions of CFD/CHT methods. The human body condition parameters (2 parameters), are then added to the computational tools to comply with ISO 7730 universal standards.

Within the framework of ISO 2005, PMV index was obtained for 1300 test subjects by evaluation of how the subjects feel thermally in different indoor environmental condition and body conditions. Here, PMV index corresponds to ASHRAE standard

indicated in Figure 1.2 in which the majority of people in large groups express how they feel from operative temperature (OT) point of view. This OT is within a defined range based on values obtained from PMV results. In case this range is exceeded, the PMV values may interpret the hot environment hotter than it is and the cold environment colder than it is. The results of this test is depicted in Figure 1.3, where horizontal axis Predicted Percent Dissatisfied (PPD) can be calculated using the PMV results. We will discuss this in details in Chapter II.

(-3) (-2) (-1) (0) (+1) (+2) (+3)
 COLD → COOL → SLIGHTLY COOL → NEUTRAL ← SLIGHTLY WARM ← WARM ← HOT

Figure 1.2 P.O. Fanger thermal sensation range.

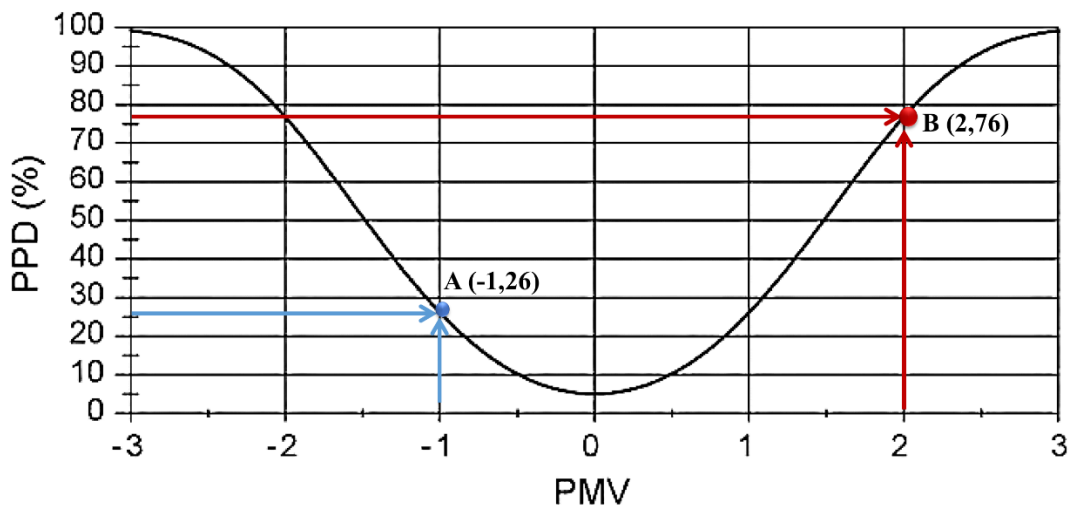


Figure 1.3 PMV vs. PPD graph. Point A(-1,26) shows that when sensible temperature is slightly cool, 26% of people experienced thermal discomfort. Similarly, at point B(2,76) when the sensible temperature 76% of people reported thermal discomfort.

In evaluating thermal comfort by a CFD/CHT tool, the mean air speed cannot directly be obtained. Hence, alternatively velocity profile should be considered. Since

velocity vector magnitude is smaller than the mean air speed, this method may lead to underestimated thermal discomfort levels.

In 2002, a CFD-based correction method was proposed for calculating thermal comfort. In two cases studied, air speed and draught rating values were obtained and the effect of the turbulence correction was investigated [27]. Their results suggested that a significant correction in room areas with high turbulence intensities was achievable. In particular, turbulence intensity is large when considering average values in the occupied zone of room. However, the correction values were found to be smaller for the maximum speed or maximum draught rating (the percentage of people predicted to be bothered by draught) in the room. They also suggested that the turbulence correction should be applied to CFD solutions when estimating air speed, thermal comfort and draught.

In 2006, Treeck et al. [28] addressed the state of the development of a Computational Steering Environment (CSE) for interactive indoor thermal comfort analysis by using high-performance super-computing systems. It was tested on two industrial applications with complex geometries, turbulent natural convection in the separator room of a ferry boat and turbulent convection in a train's passenger carriage. In order to resolve all the physical quantities concerned, a module for computing short and long-wave radiative heat transfer was applied where the latter was based on the radiosity method with a fast visibility check utilizing space tree data structures and a level of detail-dependent view factor calculation.

In 2006, Atmaca et al. [29] conducted a study on the relative humidity effects on skin temperature and skin wettedness for varying OT. They simulated the thermal interactions between human body and environment. They made 16 segments-Gagge 2-

node model analysis. Their findings were compared against the available data in literature and the experimental results, and it was shown that the model is capable of producing accurate results. In addition, it was presented that the relative humidity is not an effective parameter on the skin temperatures and skin wettedness, if the OT is within the acceptable range for the thermal comfort. However, with an increase in the relative humidity, significant increase in skin temperatures and wettedness occurs at high OT.

In 2007, Lampe et al. investigated the applicability of User-Defined-Functions (UDFs) for determination of thermal comfort indices for non-uniform environments. The need for such a work was drawn from the necessity to thoroughly evaluate thermal environments in aircraft cabins. It is common practice by Airbus to explore the initial layout of ventilation systems also on the basis of CFD. When airflow simulations for the A400M cargo hold were performed with CFD, thermal comfort was used in accordance with ISO 7730 standards. The assessment of such environments was approached by computing the PMV and PPD [30]. CFD measurements in strongly non-uniform environments should be performed at different places, at or around the subject to form average quantities (ISO 7726). The study compared indices based on CFD computed parameter quantities averaged over an area or a volume of cells near a human model to indices based on human subject votes. The CFD model offered reality equivalent airflow behavior confirmed when compared with practical experimental data.

TC indices can be successfully computed as surface averaged values by means of CFD/CHT analysis. The accuracy of their results was found to be within +10/-20 percentage points for PPD for all measurement surfaces without special precautions. Based on this study, detailed measurements where performed at surfaces placed 50 cm from the human models resulted in accuracies within ± 10 percentage points PPD. This

means that a proposed alternative approach, which involves UDF calculation that disregards human model induced radiant heat, resulted in accuracy of ± 5 percentage points PPD off target values for the optimal measuring distance to the human models [31]. This order of accuracy is considered acceptable when it is taken into consideration that the surface averaged thermal comfort indices can only be used for initial ventilation layouts and comparison between various ventilation configurations. However, in the future it is desirable to have.

Following their earlier work [29], in 2007, Atmaca et al. investigated the local differences between body segments caused by high radiant temperature, and analyzed the interior surface temperatures for different wall and ceiling constructions with their effect on TC. For the segment-wise thermal interactions between human body and its surrounding, simulations have been conducted by appropriately modifying Gagge 2-node model to multi-segment case to demonstrate the local differences. Simulation results were found to be in good agreement with experimental and simulation results reported in the literature. To calculate the interior surface temperatures of the wall and ceiling, the Sol-air temperature approach is used for convenience. The sol-air temperature (T_e), which is defined as the equivalent outdoor air temperature that provides the same rate of heat transfer to a surface as would the combined solar radiation intensity (I), convection with the outside air, and radiation transfer with the sky and the surrounding surfaces [32]–[34]. It is presented in the paper [35] that the body segments close the relatively hot surfaces are more affected than others and interior surface temperatures of uninsulated walls and ceilings exposed to a strong solar radiation reach high levels, all of which results in thermal discomfort for the occupants in buildings. This research needs further improvements, and is currently being taking by Professor Mengüç and his students at CEEE.

In 2009, Catalina et al. performed a fully experimental study with the support of an extended analysis on the air flow pattern by using CFD [36]. The air cooling using chilled ceiling panels was found to be an interesting alternative to traditional acclimatization system. The air velocity fields obtained from the CFD analysis revealed that a local discomfort at feet/ankle zone was observed but with good values of air velocity for the rest of the test room. In addition, the mean radiant temperature (MRT), a necessary element for the PMV calculations, was determined using a radiosity method by utilizing the view factors in each point of the analyzed planes and with the experimental data. PMV plots showed that the thermal comfort is achieved and is uniformly distributed within the test room. The results presented confirmed that the cooling ceiling has advantages like low vertical air gradient and that a better TC is obtained even for higher metabolic rates or clothing insulation.

In 2012, Wu et al. completed a CFD simulation with TC calculations on a test room which was acclimatized by HVAC system [37]. By CFD method, indoor environment and comfort parameters across the volume were investigated. In particular, around the body surface, accurate meshing was used to examine the effect of the local air flow distribution near the human body on TC. To receive the overall TC indices for a human subject, weighting factors for the body parts were utilized based on the skin blood flow. In the analysis, with the given uniform air flow distribution inside the testing room, the effect of local air flow and heat transfer on the overall TC was not significant as it was affected by mesh quality. They advised to apply the same approach to evaluate TC for occupants in other CFD simulated indoor environmental conditions that have a more complicated ventilation HVAC system. They presented the importance of boundary layer mesh thickness effects on PPD calculations which result in the change of heat transfer coefficient. The boundary layer mesh thickness is 25.4 (1 inch)

mm and has eight layers. Two surface mesh shells that are 12.7 mm and 25.4 mm away from the body surface are generated for the body TC calculation. Different body parts of a manikin were defined by a separate mesh surfaces. The effect of local air flow and heat transfer on the human body TC calculation were demonstrated where it was concluded that especially the local PPD of the back and pelvis is much higher for the 25.4 mm mesh shell when compared against 12.7 mm mesh size.

Prakash et al. investigated a modified equation for the determination of PMV obtained from Fanger's equation [38]. This PMV equation is the function of people's metabolic rate, people's work activity, insulation value of clothings' and indoor temperature. Also, a detailed indoor air flow simulation was performed for a room with window openings at the adjacent wall under the generalized window opening area and its position by CFD method. In addition, the effect of window opening area, position of the opening from the ground level and its orientation in lateral and longitudinal directions on the indoor air temperature distribution were explored. A three dimensional model was created and standard k- ϵ turbulence model was used to account for air-turbulence due to ventilation system. The CFD/CHT simulation results were examined for grid independency and the simulated results were checked against the results from a network model. For the scenarios studied, the average temperature at various planes are calculated. Finally, the regression analysis on the predicted average indoor temperature was performed. The developed modified equation of PMV and the regression models for the average indoor temperature were found to have close agreement with both Fanger's equation and the CFD simulations.

In 2013, Webb [39] investigated Building Energy Simulation (BES) and CFD to estimate and verify that the under floor air distribution (UFAD) design for an office

building in Melbourne, Australia. He showed that it was possible to provide sufficient cooling rates such that the PMV did not surpass 0.5. Both BES and CFD revealed that the suggested UFAD system would provide sufficient cooling during summer design conditions. He also suggested that additional BES and CFD simulations would confirm the sensitivity of PMV to marginal adjustments to flow rates and supply air temperatures. However, during commissioning, the controls must be tuned on to provide reasonable conditions across multiple zones served by the one air handling unit. Therefore, tuning of one individual perimeter office zone is not necessarily a practical choice.

In 2013, Gooje studied TC radiant asymmetry in a space [40]. In order to verify the simulation results, an actual data set from an Adobe house at Carefree, Arizona was used. The validated results from the simulations were used to generate TC model. Fanger's PMV model was employed to find the impact of radiant asymmetry on human comfort. In this study, the demand for the green building industry to focus on the effects of radiant asymmetry on TC in lieu of average space temperature was emphasized.

There was a significant overlap in the trend lines showing stratification along vertical and horizontal plane, discounting the divergence in the roof temperatures from the simulation. Properties of the roof had to be revised to mimic the actual roof characteristics, which would substantially, make the simulations closer to real data. The results of OT were given, where the actual data presents the simplified and uniform temperature conditions while the simulation depicts the OP obtained from non-uniform conditions. The deviation of the OT in stratified condition constitutes that the more surfaces involved in the calculation of mean radiant temperature (MRT) would increase fluctuation. OT that rises above the comfort band afternoon 12:00 and drops below the band at 03:00 could be appropriately moderated by including the proper passive

strategies. It was concluded that the comfort zone could be expanded to one or two °C without giving rise to any discomfort.

In 2015, Bonefacic et al. investigated a three-dimensional case of heat transfer and air flow for indoor space cooling with a wall-mounted Air Conditioning (A/C) unit during the summer in Rijeka, Croatia. A CFD/CHT analysis was carried out to analyze the effect of different air flow angles of the A/C unit on the temperature and air velocity distribution under standard conditions with and without a direct solar radiation source. As parameters of TC conditions, the airflow velocity, indoor temperatures with its gradients, and the MRT were analyzed. Physical processes were modelled using FLUENT CFD/CHT software [41]. Calculations were carried out for an empty room without internal heat sources. When direct solar radiation through the window for an extreme case of summer solstice was included in the calculation, considerable deviations from TC conditions were observed, leading to the conclusion that solar radiation must be included in numerical simulations to properly predict heat balance and thermal comfort parameters in enclosed spaces. “This observation was one of our main reasons for putting additional emphasis on radiation transfer in the present study”.

In this case of Bonefacic et al (32) to eliminate the buoyancy effects, it was essential to increase the air flow velocity from the A/C unit, which could lead to local air velocity distortions resulting in disturbed optimal comfort values. Both the measurements and CFD modeling results revealed a significant temperature increase of the floor area directly exposed to the sun. Although, a relatively small area, it greatly influenced comfort conditions by raising the average temperature of the air and by introducing strong buoyancy. Even though the simulation of the room is simplified by omitting people, furniture, and additional heat sources, it could be concluded that solar radiation is a very important factor in estimating comfortable thermal environments. To

accurately predict heat balance and comfort conditions in the room, solar radiation must be included in CFD analysis. The CFD results can be easily expanded to similar technical problems from the field of heating, ventilation and air-conditioning. It could also include air humidity internal heat sources, such as occupants, computers, and furniture, among others. In addition, Bonafacic et al. suggested that time-dependent boundary conditions could be included as a variable air flow outlet angle achieved by swinging flaps on an indoor A/C unit. Including those factors yielded to more realistic analysis but a major limiting factor in complex problems was the available CPU power, and the calculations were computationally expensive.

In 2015, we started investigating a 3D, time-dependent TC conditions in an occupied room with furniture of varying materials (i.e. steel, wood, etc.), including the heat capacity, under direct solar radiation in Istanbul, Turkey by using a CFD-based FloEFD software. The evolution of CFD brings to designers the capability to numerically analyze 3D physics of air distribution, TC, contaminant dispersion, thermal efficiency of the built environment in a fast and an accurate way. This is a fast computational tool, allowing detailed 3D visualizations and allows us to include geometrical details of the HVAC system's diffusers. We have included the required TC conditions such as the air velocity, indoor temperatures, humidity, and the mean radiant temperature into our analyses. This work was significantly different from the earlier works as it included the spectral surface emissivity of the existing materials in the room and the spectral transmissivity of window glasses. In our analyses, we have taken into account both conduction and spectral radiation analyses, which has led us to calculate more accurate and detailed TC conditions, which were in close agreement with the experimental data obtained in a class room. Furthermore, in the evaluation of heat transfer profiles in the room and on the walls, we have discretized both the fluid and solid volumes. In the

most related previous studies, only the discretization of the fluid flow was considered in the calculations. In these studies, only a surface mesh analysis for the solids presented in the computational domain was considered. However, in our studies, when a solid computational domain is presented within the fluid computational domain, we treat it as a volume and apply volume mesh analysis. In this way, we include all the material physical properties in the calculations which results in a more precise evaluation of CHT.

1.3 Outline of Thesis

In this thesis, we wanted to draw conclusion from all the studies done before and move the thermal comfort up one level higher.

In Chapter I, in general background of indoor environmental qualities with perspective of different comfort assumptions are estimated. The methodology of determining the TC in an environment before the construction phase of building is defined. The literature is reviewed and the approaches to examine TC are discussed.

In Chapter II, first the necessary mathematical formulations are provided and the physics of the problem considered in thesis is explained. The equations of fluid flow (Navier-Stokes) and conservation of energy are discussed next. The spectral radiative heat transfer modeling in simulations with solar load model is utilized in detail. In addition, Fanger's method formulations are mentioned.

In Chapter III, the model considered in this thesis is an office room. The office is in the Engineering Building of Özyeğin University (Office room of CEEE). This room is used for the all simulations. Dimensions and the material properties of the furniture, walls and windows are provided in details.

In Chapter IV, the details of the CFD method is given. Its step by step developmental procedures are provided. Next, these steps are applied to the specific scenarios considered here. The numerical validation is also given in this chapter. Comparisons with the experimental tests are proved.

In Chapter V, we provide a detailed transient analysis for comparison of TC scenarios in the demonstration room. Furthermore, all comparison results for the TC are given in determined comfort zones and seating places of occupants.

In Chapter VI, we have summarized all the necessary steps that need to be considered in the step by step development of TC analysis of a typical space. The details of the numerical evaluation and experimental measurements are reviewed and the possible future extensions of this work are discussed.

CHAPTER II

FUNDAMENTAL AND THEORETICAL ASPECT

In this Chapter, we first provide the discussions of the mathematical formulations and then we state the physics of the problems considered in this thesis. The governing equations of fluid flow (Navier-Stokes equations) and heat transfer (conservation of energy) analyses are outlined in section 2.1. Next, specialized turbulence model (k-epsilon) formulations are given in section 2.2.1 which cover both the equations considered by the FloEFD software and also the physics of fluid mechanics. In section 2.2 and its subsections, radiation heat transfer modelling for simulations, solar load model and environment temperature, discrete transfer model, discrete ordinates model, absorption and transmission, reflection and radiation spectrum is discussed in details. In section 2.2.4, Fanger's method's formulations for TC are given.

2.1. Governing Equations for Air Flow and Heat Transfer

When solving a fluid mechanics problems, Navier-Stokes equations are used, as they govern the conservation of momentum. They need to be coupled with the conservation of mass (continuity equation) and the conservation of energy (first law of thermodynamics) equations, if a heat transfer problem is to be tackled. In order to solve these equations, it is possible to adopt either integral or differential methods. When adopting these numerical techniques, one may always take into considerations the thermodynamics state relation and the required boundary conditions. These conditions are modeled mathematically by integral and differential analyses and are solved by means of computational tools [42-46].

We here provide the full conservation equations for flow, momentum and energy as described below in Cartesian coordinate system:

Continuity Equation:

$$\frac{\partial \rho}{\partial t} + \frac{\partial}{\partial x_i} (\rho u_i) = 0 \quad (1)$$

where u is the fluid velocity, ρ is the density of fluid in Eq. 1,

Momentum Equation:

$$\frac{\partial \rho u_j}{\partial t} + \frac{\partial}{\partial x_j} (\rho u_i u_j) + \frac{\partial p}{\partial x_i} = \frac{\partial}{\partial x_j} (\tau_{ij} + \tau_{ij}^R) + S_i \quad (2)$$

τ stands for the viscous shear stress tensor and S is a mass-distributed external force per unit mass in Eq. (2)

Energy Equation:

$$\frac{\partial \rho H}{\partial t} + \frac{\partial \rho u_i H}{\partial x_i} = \frac{\partial}{\partial x_i} (u_i (\tau_{ij} + \tau_{ij}^R) + q_i) + \frac{\partial p}{\partial t} - \tau_{ij}^R \frac{\partial u_i}{\partial x_j} + \rho \varepsilon + S_i u_i + Q_H \quad (3)$$

$$H = h + \frac{u^2}{2} \quad (4)$$

in Eq. (4) h is the thermal enthalpy, Q_H is the heat source and q_i is the diffusive heat flux. The viscous shear stress tensor for Newtonian fluids is given in Eq. (5):

$$\tau_i = \mu \left(\frac{\partial u_i}{\partial x_i} + \frac{\partial u_j}{\partial x_i} - \frac{2}{3} \delta_{ij} \frac{\delta u_k}{\delta x_k} \right) \quad (5)$$

and δ_{ij} is the Kronecker delta function and μ is the dynamic viscosity coefficient.

2.1.1. Turbulence Model *k-epsilon*:

Some HVAC systems, the flow can be slow and laminar. Some of the HVAC design should include laminar flow especially operating, clean rooms or kitchens [47–49]. However, in many conditioned rooms, the flow can be turbulent. For that reason, we must use a reasonable turbulence model in the calculations. In this study, the Reynolds number is calculated and determined to predict whether the flow in the room is turbulent. The characteristic length is chosen the hydraulic diameter of HVAC diffuser channel.

Table 1 Calculation of Reynolds Number

Density of Air (ρ)	Temperature of Air (T)	Velocity (u)	Characteristic Length (d_h)	Dynamic Viscosity (μ)
1.2041 kg/m^3	20 °C	1.9 m/s	1.2 m	0.0000122
Reynold Number = $\rho u d_h / \mu$				Re=225029

For a flow to be identified as turbulent, the Reynolds number has to be greater than 4000. For the results presented in Table 1, we can identify the flow as turbulent [50]. Throughout this thesis, a *k-epsilon*, two equations model was adapted to solve turbulence effect. The other methods such as Direct Numerical Simulation (DNS) or Large Eddy Simulation (LES) are computationally too expensive and may not be justified to be used in buildings CFD models. DNS applications are practically inapplicable for complex 3D large domains such as the cases considered in this thesis, due to wide spectra of velocity fluctuations and small physical grid size. LES model of turbulence is computationally less expensive compared against DNS. Nevertheless, LES is computationally too expensive for the models considered in this work [51].

In the frame of k-epsilon turbulence model, μ_t is the turbulent eddy viscosity coefficient as shown in Eq. (6), is defined using two basic turbulence properties. One of them is turbulent kinetic energy k and other is turbulent dissipation; ε ,

$$\mu_t = f_\mu \frac{C_\mu \rho k^2}{\varepsilon} \quad (6)$$

Also, turbulent viscosity factor is defined as in Eq. (7),

$$f_\mu = [1 - \exp(-0.0165 R_y)]^2 \cdot \left(1 + \frac{20.5}{R_T}\right) \quad (7)$$

$$R_T = \frac{\rho k^2}{\mu \varepsilon}, \quad R_y = \frac{\rho \sqrt{k} y}{\mu} \quad (8)$$

f_μ is a turbulent viscosity factor and y is the distance from wall. To take into account laminar-turbulent transition, the function which is introduced by Arens and Zhang [11] is quite handy. To this end, two additional transport equations are used to describe the turbulent kinetic energy and dissipation.

$$\frac{\partial \rho k}{\partial t} + \frac{\partial}{\partial x_i} (\rho u_i k) = \frac{\partial}{\partial x_i} \left(\left(\mu + \frac{\mu_t}{\sigma_k} \right) \frac{\partial k}{\partial x_i} \right) + S_k \quad (9)$$

$$\frac{\partial \rho \varepsilon}{\partial t} + \frac{\partial}{\partial x_i} (\rho u_i \varepsilon) = \frac{\partial}{\partial x_i} \left(\left(\mu + \frac{\mu_t}{\sigma_\varepsilon} \right) \frac{\partial \varepsilon}{\partial x_i} \right) + S_\varepsilon \quad (10)$$

The source terms S_k and S_ε are defined as;

$$S_k = \tau_{ij}^R \frac{\partial u_i}{\partial x_j} - \rho \varepsilon + \mu_t P_B \quad (11)$$

$$S_\varepsilon = C_\varepsilon \frac{\varepsilon}{k} \left(f_1 \tau_{ij}^R \frac{\partial u_i}{\partial x_j} + \mu_t C_B P_B \right) - C_{\varepsilon 2} f_2 \frac{\rho \varepsilon^2}{k} \quad (12)$$

We use P_B parameter to calculate the turbulent generation due to buoyancy forces and it can be written as;

$$P_B = -\frac{g_i}{\sigma_B} \frac{1}{\rho} \frac{\partial \rho}{\partial x_i} \quad (13)$$

P_B can be considered as the gradient of density term, which gives rise to natural convection effects. In this expression g_i is component of gravitational acceleration in x_i direction. If P_B is greater than zero σ_B and C_B are constant, respectively, is accepted 0,9 and 1. Otherwise,

$$f_1 = 1 + \left(\frac{0.05}{f_\mu} \right), f_2 = 1 - \exp(-R_T^2) \quad (14)$$

The constant parameters $C_\mu, C_{\varepsilon 1}, C_{\varepsilon 2}, \sigma_k, \sigma_\varepsilon$ are empirically defined [52]. In FloEFD computational software, the following parameters are used:

$$C_\mu = 0.09, C_{\varepsilon 1} = 1.44, C_{\varepsilon 2} = 1.92, \sigma_\varepsilon = 1.3, \sigma_k = 1$$

All the simulations we accept Lewis number $Le=1$ Thus the diffusive heat flux:

$$q_i = \left(\frac{\mu}{Pr} + \frac{\mu_t}{\sigma_c} \right) \frac{\partial h}{\partial x}, i = 1, 2, 3 \quad (15)$$

$\sigma_c = 0.9$ was accepted. All other notations are given in nomenclature.

2.2 *Thermal Radiative Transfer*

Radiative heat transfer is one of the fundamental mechanisms of heat transfer. In comparison to the other modes of heat transfer, conduction and convection, radiative transfer has the following distinct characteristics: I) it can transfer energy with or without an intervening medium, II) the radiant heat flux is not proportional to the temperature gradient, a characteristic which makes significant difference particularly at high temperatures, III) radiation emission is wavelength and temperature dependent; and finally, IV) the radiant energy exchange and radiative properties are direction dependent.

Radiative energy propagation can be modeled using classical electromagnetic wave theory (EM-theory) [53]. The EM-theory may provide conservation equations. For most thermal radiation problems, the Planck's blackbody radiation can be used to relate the temperature of an object with its emission spectrum and radiative energy. The emitted radiative heat flux from an object is a strong function of the temperature of a substance. Materials at higher temperature emit significant radiation. The rate of heat flow per unit surface area emitted by a radiating surface is called its emissive power E (W/m^2).

$$E_b = \sigma T^4 \quad (16)$$

The incident radiative heat flux at any location varies as a function of orientation of the receiver relative to the radiation source. The intensity is the rate of heat flow received per unit area perpendicular to the rays and per unit solid angle and is a quantity with a magnitude that will vary with direction. The ratio of the heat flux emitted by a real surface and a black surface at the same temperature is called the surface emissivity.

Also, the (non-directional) emitted intensity I_s of a real surface is the product of its surface emissivity and the black-body intensity [53] :

$$I_s = \varepsilon I_b = \varepsilon \sigma T_s^4 / \pi \quad (17)$$

Figure 2.1 graphically shows the reflection, absorption, transmission and emission mechanisms from a surface. In this thesis, we assume that air is transparent to the radiation associated with room temperature.

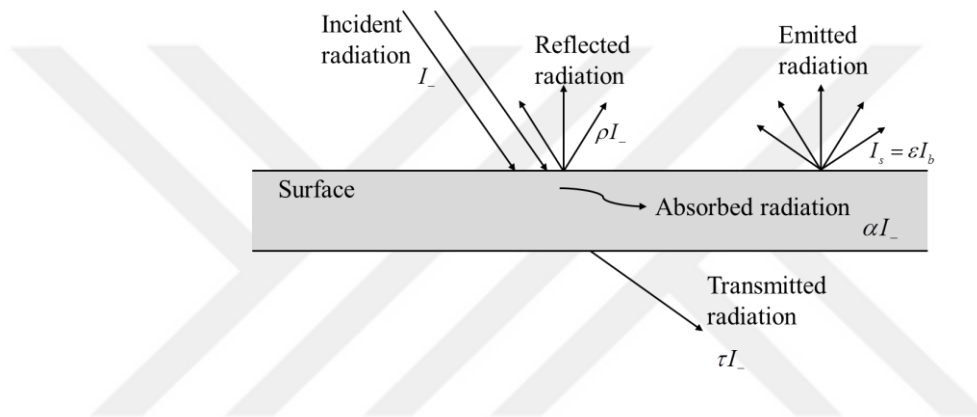


Figure 2.1 Surface interaction with incident radiation.

Absorption and scattering effects in a medium can be calculated by equation of radiative heat transfer in a participating medium. Figure 2.1 shows the treatment of radiation in participating medium.

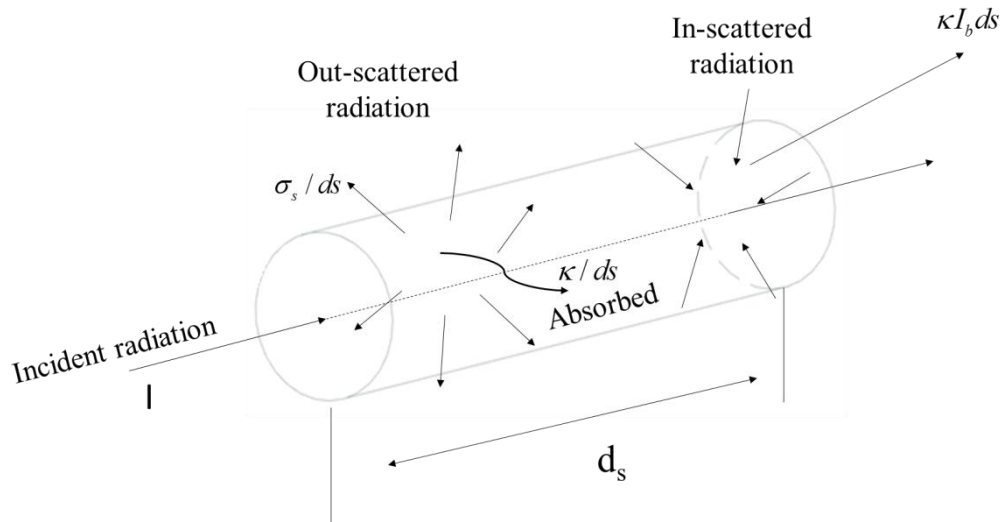


Figure 2.2 Radiative heat transfer in participating medium [46].

When performing a numerical analysis, radiation model should be treated differently for solar calculations, due to the fact that direct solar radiation is collimated in nature. There are two different radiation models in FloEFD software. One of them is Discrete Transfer (DT) method and the other is Discrete Ordinates (DO) method. In thesis, DO model is used since all necessary input parameters for materials can be taken into the account with this method. When evaluating materials such as glasses which are semi-transparent materials, reflection, absorption and transmission can be calculated with DO model. Since, the impact of coating on surfaces cannot be defined in the software, glass material has been accepted as participating medium and instead of DT, DO model is used. The radiation-related methods of calculations, described in this chapter, have used the technical documentation guide of the software FloEFD. We discuss them more in detail below in sub-section.

2.2.1 Discrete Transfer Model (DT)

In this method the radiation leaving the surface element in a certain range of solid angles is considered. The radiation heat is transferred along a series of rays emanating from the radiative surfaces only. When reaching other radiative surfaces, rays are traced as passing through transparent solid and fluid bodies. FloEFD recognizes this method as “ray tracing” which allows "exchange factors or view factor" to be calculated as the fraction of the total radiation energy emitted from one of the radiative surfaces that is intercepted by other radiative surfaces (this quantity is a discrete analog of view factors). Between radiative surface grid elements ‘exchange factor’ are calculated at the beginning of analysis, which help to create coefficients for a system of linear equations which is solved in each iteration.

When using DT model, heat radiation from the solid surfaces (emitted and reflected) is assumed to be diffuse, based on the Lambert Law. These radiative solid surfaces are assumed to be ideal gray bodies. Absorption and reflection of the solar radiation by surfaces happens independently from thermal radiation coming from other heat radiation sources. Note that, DT model cannot account for the absorption of radiation in semi-transparent mediums, for FloEFD software assumption.

The thermal radiation incident on an opaque surface can be reflected and absorbed. Under radiative equilibrium, according to the Kirchhoff’s law, spectral directional absorptivity becomes equal to directional spectral emissivity. For most practical purposes, we can consider the building surfaces as diffuse, although spectral properties need to be considered later in the thesis.

We can define thermal radiation leaving a surface Q_T^{out} as following

$$Q_T^{out} = \varepsilon \cdot \sigma \cdot T^4 \cdot A + (1 - \varepsilon) \cdot Q_T^{in} \quad (19)$$

where Q_T^{in} is the incident thermal radiation, A is the surface area. The emitted radiation flux is obtained depending on material temperature and the heat flux coming from other surrounding surfaces.

Now let us define Q_S^{in} as the incident solar radiation arriving at a surface, Q_S^{source} is the radiation arriving at this surface from solar sources in directional manner. When calculating the directional sun-shine dependent radiation Q_S^{out} we can write

$$Q_S^{out} = (1 - \varepsilon) \cdot (Q_S^{in} + Q_S^{source}) \quad (20)$$

Based on the discussions given above, if we consider thermal radiation from all surfaces and from the sun, we can calculate net radiation as given in Eq.(21):

$$Q^{net} = Q^{out} - Q^{in} = (Q_T^{out} + Q_S^{out}) - (Q_T^{in} + Q_S^{in}) \quad (21)$$

where Q^{net} is the net radiation, Q^{out} is the leaving radiation from the surfaces, Q^{in} is the incident heat radiation arriving the surfaces, as shown in figure 2.3.

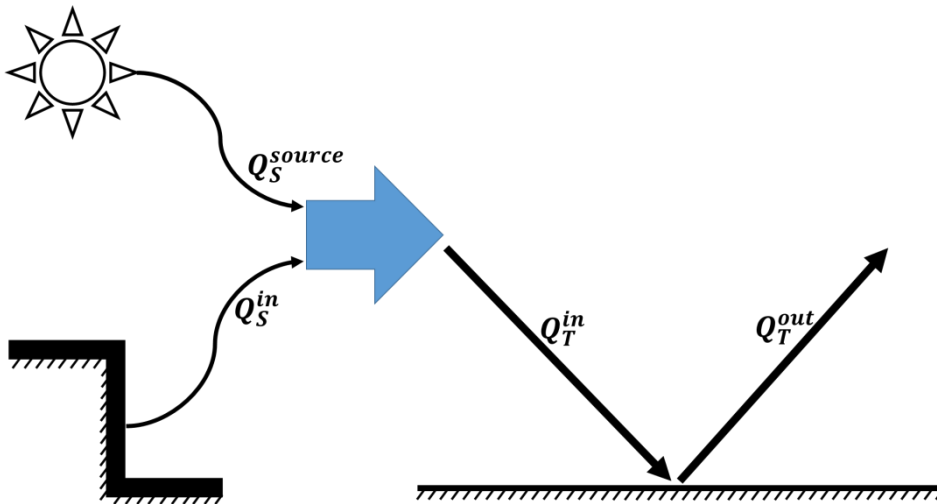


Figure 2.3 The schematic definition for Q^{net} .

2.2.2 Discrete Ordinates Model (DO)

Discrete Ordinates which is the method incorporated in the FloEFD software allows detailed analysis of radiation transfer by including both spectral dependencies and absorption parameters into calculation. DT assumes that semi-transparent materials act as participating medium, and the model is limited in nature. On the other hand, the DO model solves the radiative transfer equation (RTE) for a finite number of discrete solid angles, each associated with a vector direction. Also, number of discrete directions determines the accuracy of the solution, where the discrete directions \vec{s} representing the directional domain of 4π at any position within the computational domain defined by the position vector \vec{r} . The directional domain is broken down into the specified number of equal solid angles or directions. The total number of directions N_{ord} is defined as:

$$N_{ord} = 8 \cdot \frac{RL \cdot (RL + 1)}{2} \quad (22)$$

and discretization level is defined as RL [53]. Inside each direction the radiation intensity is considered constant. FloEFD software does not include scattering coefficient in RTE, so it can be written as:

$$\frac{dI(\vec{s}, \vec{r})}{ds} = \alpha \cdot [n^2 \cdot I_b(\vec{r}) - I(\vec{s}, \vec{r})] \quad (23)$$

where I is the radiation intensity per solid angle, $I_b = \frac{\sigma T^4}{\pi}$ is the blackbody radiation intensity, α is the absorption coefficient and n is the refractive index.

In the FloEFD software, as opposed to DT, when working with the DO method, transparent medium absorb the incident intensity depending on the specified absorption coefficient and the rest of the incident intensity is reflected.

2.2.3 Absorption and Transmission

In FloEFD software, the radiation models for semi-transparent materials are Monte Carlo or DO models. However, the license of the software used in thesis work allows DT and DO models only. Therefore, Monte Carlo model was kept out of examination. Now let us consider a simple explanation of the underlying physics of the problem.

We can write the transfer of radiation along x -axis in a participating medium as follows (see in Fig. 2.2):

$$\frac{dI(x)}{dx} = -\alpha \cdot I(x) \quad (24)$$

Radiation density shall decrease along x -axis along with passing light;

$$I(x) = I_0 e^{-\alpha L} \quad (25)$$

where I_0 is the initial intensity of radiation and L is the length of the medium. At the boundaries, the calculations are made according to Snell's Law, and the incoming radiation changes its direction between surfaces where two full-transparent or semi-transparent materials having different refractive indexes contact with each other [52].

Snell's Law is given in Eq. (26)

$$\frac{\sin \theta_2}{\sin \theta_1} = \frac{n_1}{n_2} \quad (26)$$

where n_1 and n_2 values give refractive indices [53] values of the first and second

medium respectively. θ_1 and θ_2 indicate the angles of the coming and the reflected radiation respectively.

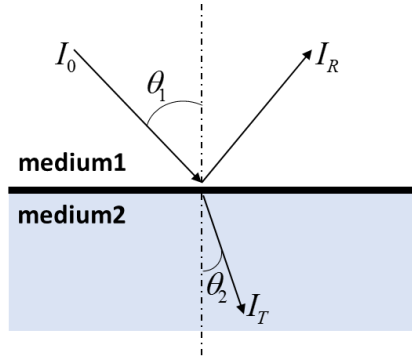


Figure 2.4 Absorbing and reflecting the coming radiation in interface point by the medium having absorption; depiction Snell's law.

With Fresnel's relation for non-polarized light, radiation-dependent reflection of semi-or full-transparent materials having different can be calculated as follows:

$$\rho = \frac{1}{2} \left[\frac{\tan^2(\theta_1 - \theta_2)}{\tan^2(\theta_1 + \theta_2)} + \frac{\sin^2(\theta_1 - \theta_2)}{\sin^2(\theta_1 + \theta_2)} \right] \quad (27)$$

This " ρ " value gives the reflected radiation. Thereby, radiation value remained from reflected radiation (i.e. the value passing through medium) can be defined as follows:

$$\tau = 1 - \rho \quad (28)$$

However, if the beam is perpendicular to the surface, we can calculate reflection and transmission values as following:

$$\rho = \left(\frac{n_1 - n_2}{n_1 + n_2} \right)^2 \quad (29)$$

$$\tau = \frac{4n_1n_2}{(n_1 + n_2)^2} \quad (30)$$

If we calculate the light beam passing through semi-transparent solid material by considering absorption, reflection and transmissivity;

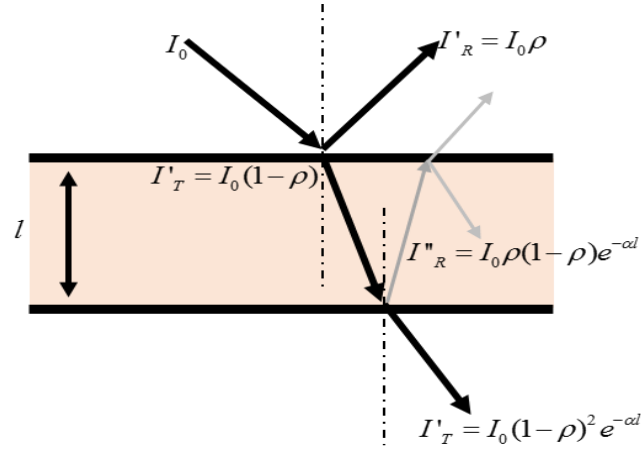


Figure 2.5 Radiation transmission through a transparent medium.

A fraction of incoming radiation I_0 , is transmitted I_T which passes through the surface of the semi-transparent material. If l is the thickness, I_T can be evaluated from Eq. (31)

$$I_T \approx I_0(1 - \rho)^2 e^{-\alpha l} \quad (31)$$

We can calculate absorption coefficient of semi-transparent material as participating medium depending on above equation:

$$\alpha = -\frac{1}{l} \ln \left(\frac{I_T}{I_0(1 - \rho)^2} \right) \quad (32)$$

2.2.4 Reflection

According to assumptions made in FloEFD software, reflection has occurred in one or more ways. It can be expressed as Lambertian (diffusive reflection) and/or diffusive and specular reflection. The reflection can be expressed as a transfer function that records for a given incoming direction, the amount of light that is reflected in a certain outgoing direction. This function – BRDF (bi-directional reflectance distribution function) - can be expressed with four different angles: two of them has been used for

coming radiation and remaining two for reflecting radiation. They are indicated as θ_i, φ_i (incident angle) and θ_r, φ_r reflected angles in the following Figure 2.6:

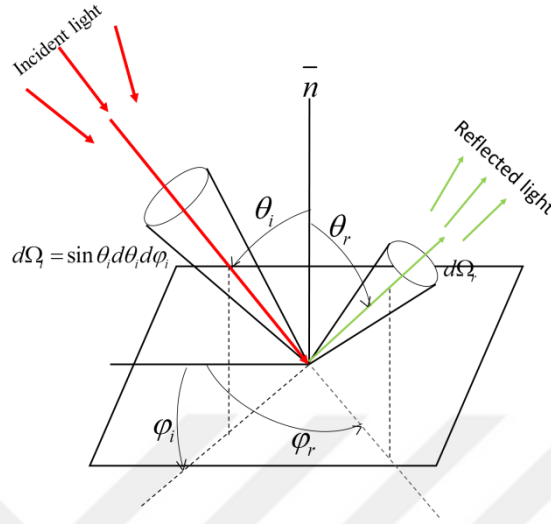


Figure 2.6 Reflection of radiation at a given surface.

The BRDF function $\rho_{bd}(\theta_i, \varphi_i, \theta_r, \varphi_r)$ is defined in terms of incident and reflected radiance by the following integral in Eq. (33)

$$L_r(\theta_r, \varphi_r) = \int_0^{2\pi} \int_0^{\pi/2} L_i(\theta_i, \varphi_i) \rho_{bp}(\theta_i, \varphi_i, \theta_r, \varphi_r) \cos \theta_i \sin \theta_i d\theta_i d\varphi_i \quad (33)$$

Depending on reflection feature of surface, we can also write BRDF function for these situations:

Diffusive (Lambertian) surface:

It is the assumption used in situation where coming radiation diffuses to each point equally without being dependent on direction.

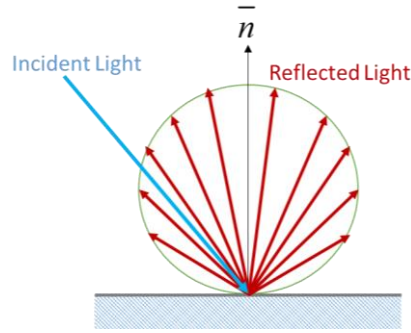


Figure 2.7 Diffuse reflection from a Lambertian surface.

The BRDF of Lambertian surface is constant:

$$\rho_{bd}(\theta_i, \varphi_i, \theta_r, \varphi_r) = \frac{\rho_d}{\pi} \quad (34)$$

and for the ideal specular surface. The surface that reflects all the light coming from the direction (θ_i, φ_i) into the direction $(\theta_i, \varphi_i + \pi)$

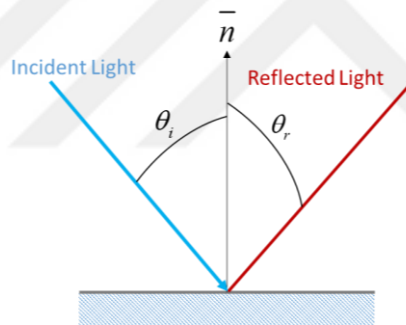


Figure 2.8 Ideal specular reflection.

So the BRDF is zero everywhere except where $\theta_i = \theta_r$ and $\varphi_i = \varphi_r + \pi$. Thus the BRDF is a delta function at direction of ideal mirror reflection:

$$\rho_{bd}(\theta_i, \varphi_i, \theta_r, \varphi_r) = \frac{\rho_s \delta(\theta_i - \theta_r) \delta(\varphi_i + \pi - \varphi_r)}{\cos \theta_i \sin \theta_i} \quad (35)$$

In case of specular and diffusive reflection the BRDF is defined as below:

$$\rho_{bd}(\theta_i, \varphi_i, \theta_r, \varphi_r) = \frac{\rho_d \rho_s \delta(\theta_i - \theta_r) \delta(\varphi_i + \pi - \varphi_r)}{\pi \cos \theta_i \sin \theta_i} \quad (36)$$

2.2.5 Radiative Heat Transfer Equation with Radiation Spectrum:

In this thesis, spectrum of semi-transparent glass material and emissivity of surfaces are the most important part to understand behavior of them under solar load calculation. Utilizing different windows glasses and surface's emissivity of material to generate better TC or to understand effects of it, in the room, we need to change spectrum properties of medium and surfaces. The radiation spectrum is considered as consisting of several bands, which edges are specified by the user. When we consider the radiation spectrum, Eq. (37) takes the following form:

$$\frac{dI_{\lambda_i}(\vec{s}, \vec{r})}{ds} = \left[k_{\lambda_i} \cdot n^2 \cdot I_{b\lambda_i}(\vec{r}) - I_{b\lambda_i}(\vec{s}, \vec{r}) \right] \quad (37)$$

2.2.6 Solar Load Model and Environment Temperature

Calculation of environmental radiation and solar radiation can be performed for both internal flow problems and external flow problems. While environmental radiation is recognized as non-directional heat transfer along with heat transfer formed from other surrounding surfaces, solar radiation is considered as directional with both power flow (intensity) and directional vectors.

In order to determine the direct and diffuse heat transfer rates, which are dependent on solar radiation in FloEFD software, the calculation of intensity is carried out first. In order to calculate intensity, the latitude of the building location in the model should be input into the software. This information is available for some European and American cities; however, it is not documented for Istanbul, Turkey. For this reason, the longitude

of the location of the model considered in this thesis was obtained from Google Earth. Initial hour at which the simulation starts, hemisphere where the model exists, zenith angle and the angle between the model and the north direction should be defined as input parameters in the FloEFD software. In addition, cloudiness value is also included as an input parameter, which varies between 0 and 1. We assume that the value is 1 when the sky is entirely cloudy and 0 in cloud-free situations.

Environment temperature is included into the formulations in order to take into consideration the atmospheric effects. In the case of a heavily cloudy sky the temperature of the environment is set equal to ambient temperature, and in the case of a clear-sky or for sky with low levels of cloudiness, the temperature of the environment is calculated from the formula given in Eq. (38):

$$T_E = T_A (1.34 + 0.0065 \cdot T_{DP}) - 26 \quad (38)$$

where T_A is the ambient temperature, T_{DP} is the dew-point temperature and T_E is the environment temperature. For the spectral distribution, four bands are defined as n1-4: 300, 780, 2500, 10000 as depicted in Figure 2.10.

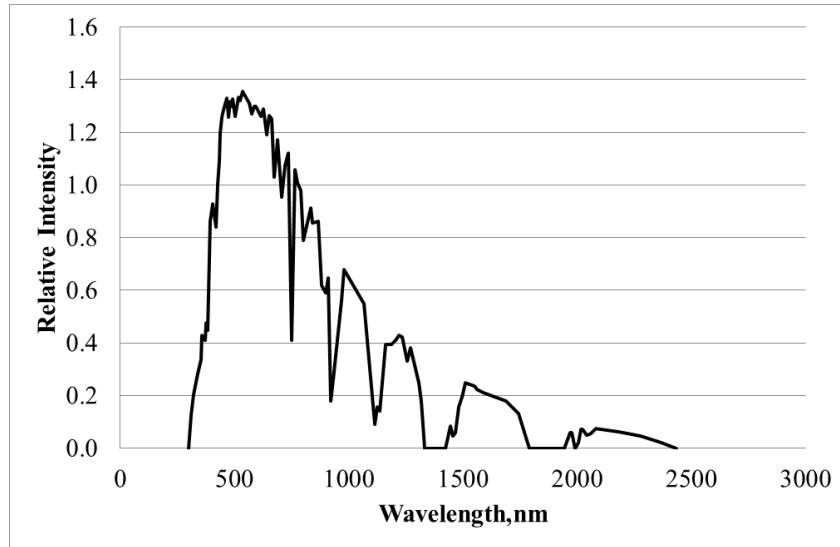


Figure 2.9 Spectrum of solar light on Earth [52].

2.3. Thermal Comfort Equations of Povl Ole (P.O.) Fanger

The equation of physical approach PMV index's calculations depend on is the equalization of the heat produced in body to the heat given to the outer environment.

In its mathematical formulation the equation is;

$$PMV = [0.303 \cdot \exp(-0.036 \cdot M) + 0.028] \cdot \left\{ \begin{array}{l} (M - W) - 3.0510^{-3} \cdot [5773 - 6.99 \cdot (M - W) - \rho_a] - 0.42 \cdot [(M - W) - 58.15] \\ -1.7 \cdot 10^{-5} \cdot M \cdot (5867 - \rho_a) - 0.0014 \cdot M \cdot (34 - t_a) - 3.96 \cdot 10^{-8} \\ \cdot f_{cl} \cdot [(t_{cl} + 273)^4 - (\bar{t}_r + 273)^4] - f_{cl} \cdot h_c \cdot (t_{cl} - t_a) \end{array} \right\} \quad (39)$$

The M" and W are the parameters which indicate metabolic heat generation rate and external work respectively. The external work is taken as zero for many activities.

While ρ_a is defined as partial water vapor evaporation, f_{cl} as the clothing area factor, t_a as the ambient air temperature, \bar{t}_r as the MRT, h_c as the convective heat transfer coefficient, t_{cl} as the surface temperature of clothing.

Fanger's calculation for the surface clothing area factor is done as such:

$$f_{cl} = \begin{cases} 1.00 + 1.29I_{cl} & \text{for } I_{cl} \leq 0.078m^2 \text{ } ^\circ C / W \\ 1.00 + 0.645I_{cl} & \text{for } I_{cl} > 0.078m^2 \text{ } ^\circ C / W \end{cases} \quad (40)$$

Here I_{cl} coefficient includes the thermal resistance value of clothing and h_c the convective heat transfer coefficient is calculated as such

$$h_c = \begin{cases} 2.38(t_{cl} - t_a)^{0.25} & \text{for } 2.38(t_{cl} - t_a)^{0.25} > 12.1\sqrt{v_{ar}} \\ 12.1\sqrt{v_{ar}} & \text{for } 2.38(t_{cl} - t_a)^{0.25} < 12.1\sqrt{v_{ar}} \end{cases} \quad (41)$$

v_{ar} used in the equation shows the value of relative air velocity (relative to human body). The parameter t_{cl} as the parameter that expresses the heat value occurred on the surface of clothing is calculated this way:

$$t_{cl} = 35.7 - 0.028(M - W) - I_{cl} \left\{ \begin{array}{l} 3.96 \cdot 10^{-8} f_{cl} \cdot \left[(t_{cl} + 273)^4 - (\bar{t}_r + 273)^4 \right] \\ + f_{cl} h_c (t_{cl} - t_a) \end{array} \right\} \quad (42)$$

In an environment where thermal conditions are specifically created, quantitative calculations were done for different people in different climate conditions by Fanger.

Besides this, Fanger has calculated the value of PPD which expresses the dissatisfaction of people in their environment in relation to PMV value.

$$PPD = 100 - 95e^{-(0.03353PMV^4 + 0.2179PMV^2)} \quad (43)$$

All the h_c (convective heat transfer coefficient) values that are used in analysis calculations will be obtained by the analysis of air flow in the inner surrounding.

CHAPTER III

MODEL DEVELOPMENT AND NUMERICAL SIMULATIONS

The model considered in this thesis, is the office of Prof. Mengüç, which is located on the 3rd floor of the engineering faculty building in the campus of Özyeğin University. This room is approximately 21 m above the ground level. This room is used on weekdays usually the between 09.00 to 17.00. The height of the room is 3 m floor to the ceiling and the floor area is 20 m².

The most important factor in choosing this office for TC analysis was that about 66% of the facades facing south and west, have windows in this office. The two dimensional room drawings were provided by the architectural design office of Özyeğin University and prior to the CFD analysis, the three dimensional model of the study room was prepared using Solidworks software. The working principle of the HVAC systems and its schematic drawings of the diffusers were obtained from the mechanical installation design office.

General view of room is given in Figure 3.1. The experimental details for the example simulations are shown from the top view of room in Figure 3.2 and sectional view Figure 3.3. In these calculations, chairs and human body were shown only virtually and were not included into the computational calculations.

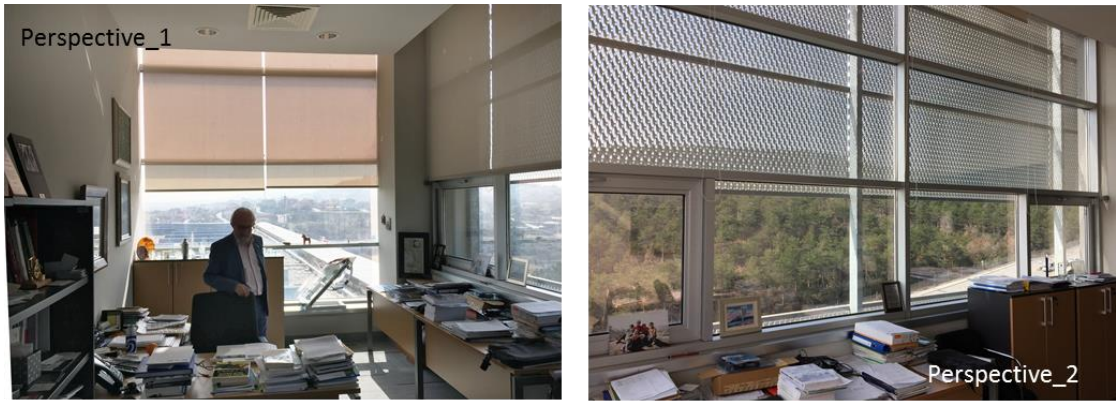


Figure 3.1 Occupant perspective of the room.

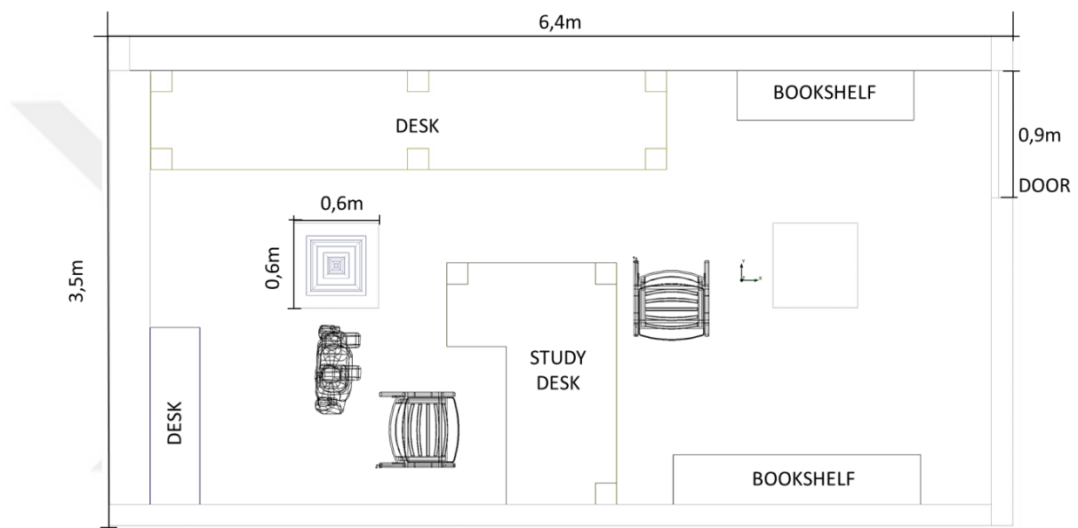


Figure 3.2 Top view of the room model.

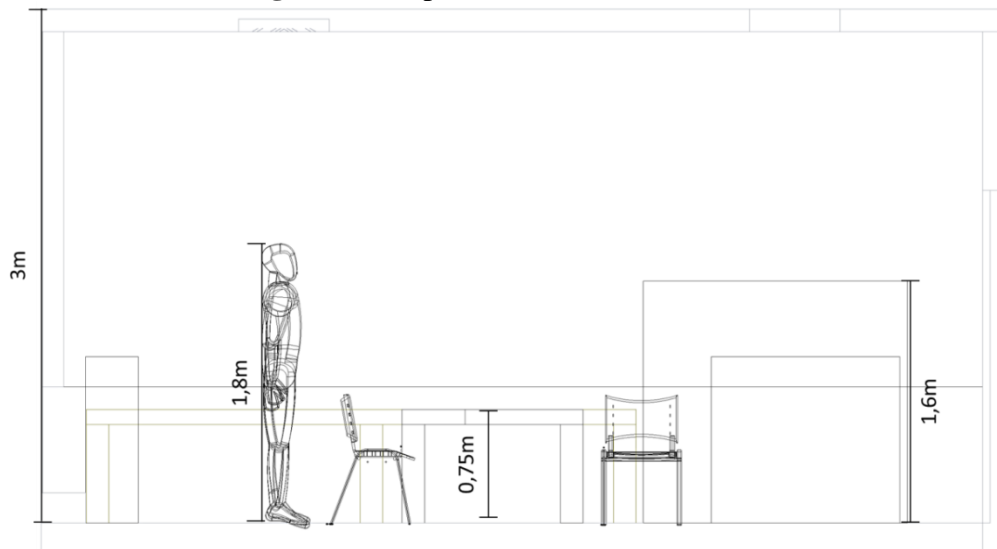


Figure 3.3 Sectional view of the room model.

In order to be able to investigate the temperature distribution on the all surfaces in the room, fluid domains and solid bodies are shown in Figure 3.4.

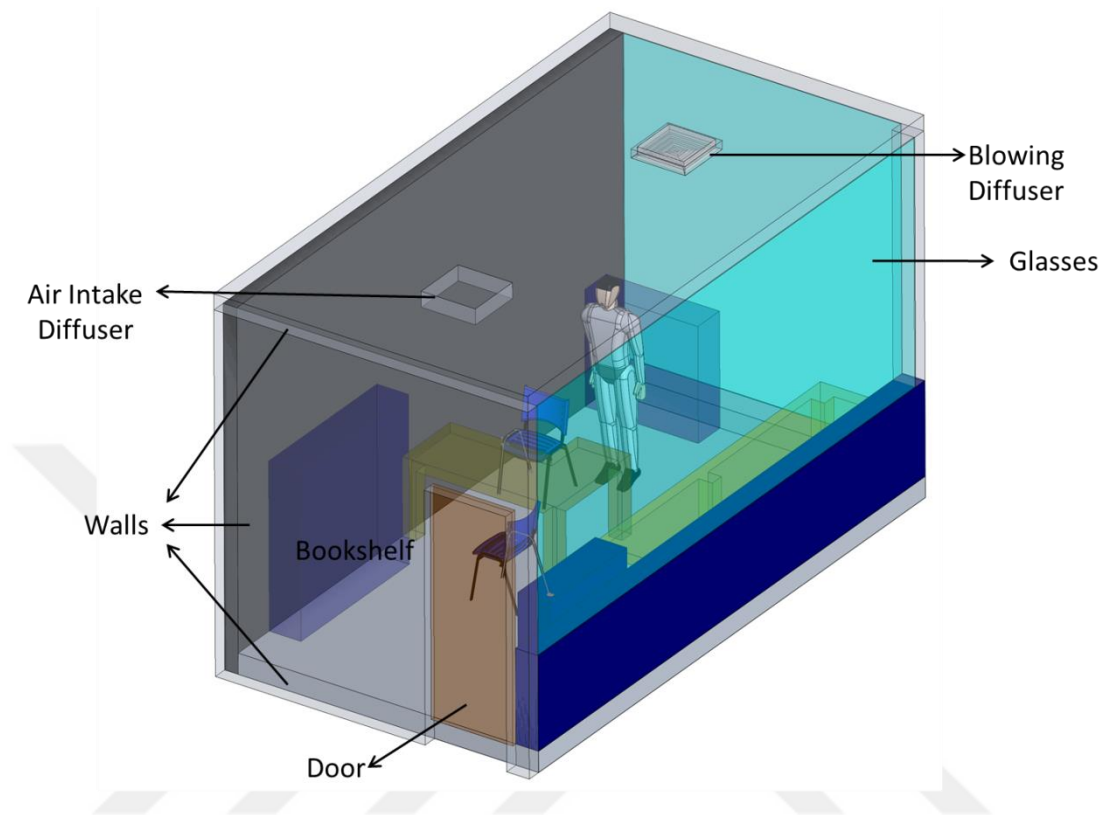


Figure 3.4 Three dimensional solid body view of the room.

3.1. Definition of HVAC System

Fan coil system was used for the acclimatization in this room. This system has a heat exchanger and a fan in the cabinet unit. It can be used in offices, houses or industrial buildings for heating or cooling applications. A fan coil system is a multiform device sometimes using ductwork, and is used to control the temperature in the volume where it is installed, or serve multiple spaces. It is controlled either by a manual on/off switch or by a thermostat, which controls the throughput of water to the heat exchanger using a control valve and/or the fan speed. The room has two fan coil diffusers under

the ceiling surface. Diffusers are designed for the horizontal spreading of air in four directions and provide the even circulation of the air inside a room. One diffuser is placed to blow into the room whereas the second diffuser is positioned to suck the air back from the room. The blades are made from aluminum and are covered with polymeric paint, which allows for use in unfavorable conditions, as depicted in Figure 3.5.

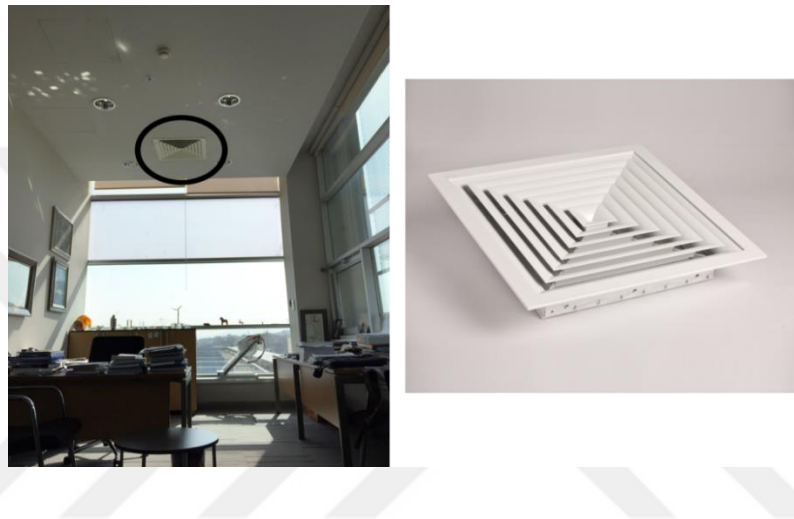


Figure 3.5 Location of the blower diffuser in the room and detail picture.

3.2. Details of the Measurement Devices

Testo 435-1 Multi-Function Climate Measuring Instrument has 3 functions on 1 probe; velocity, temperature and humidity. This probe has a head diameter of 12 mm and can measure the flow in the channel as well as the velocity and volumetric flow rate in front of the diffuser. Measurement speed is between the ranges of 0-20 m/s. In addition, this probe can measure temperature and humidity by hot wire method. The range of temperature measurement is between -20 to 70 °C and tolerance is ± 0.3 °C. The range of the humidity measurements is 0 to 100% with the tolerance, ± 2 %RH (Relative Humidity).

Testo 635-1 Thermocouple and Wireless Radio Probes with Measuring Instrument is ideally equipped for checking the air humidity, temperature and dew point in living areas, offices, in production, storage and server areas and in museums and cold stores. Measurements of the ambient absolute pressure and dew point in compressed air can be carried out with this device. In this work, thermocouples and radio handle probes were used.

Thermocouples were utilized while measuring the temperature differences on the glass and wall surfaces. The range of the temperature for thermocouple is $-50\text{ }^{\circ}\text{C}$ to $400\text{ }^{\circ}\text{C}$.

Radio handle probe can work wirelessly and can measure humidity and temperature. The measurement range for temperature is $-20\text{ }^{\circ}\text{C}$ to $70\text{ }^{\circ}\text{C}$. While the accuracy is $\pm 0.3\text{ }^{\circ}\text{C}$, and resolution is $0.1\text{ }^{\circ}\text{C}$. Testo 635-1 device has the same range of measurement as Testo 435-1 for humidity.

3.3. Types and Physical Properties of Materials Used in a Room

The walls of the room considered in the analysis are made of different layers. The layers are ordered from outside to inside as coating, exterior plaster, insulation stone wool, concrete, interior plaster and paint. In the numerical calculations, the room walls are considered as a single material and the total thermal conductivity coefficient of all existing materials is calculated and added to the calculation as a single layer. The materials used and their physical properties are given in Table 2.

For the opaque surfaces spectral emissivity [54],[55] are shown in Figure 3.6, for (a) steel sheet for desk's legs and bookshelf, (b) brown carpet for ground, (c) wood for upper surfaces of desk, and (d) white paint for walls in Figure 3.7.

Table 2 Physical properties of the materials which are used in the simulations.

No	Materials / HVAC Component	Density (kg/m ³)	Specific Heat Capacity (J/kgK)	Thermal Conductivity (W/mK)
1	Door (Thick Glass)	2900	800	2
2	Window Glasses	2600	670	1
3	Blowing Diffusers	2700	953	155
4	Air Intake Diffuser	2700	953	155
5	Walls (Floor, ceiling, side wall)	850	1000	0,7
6	Desks (wood composites)	650	1200	0,14

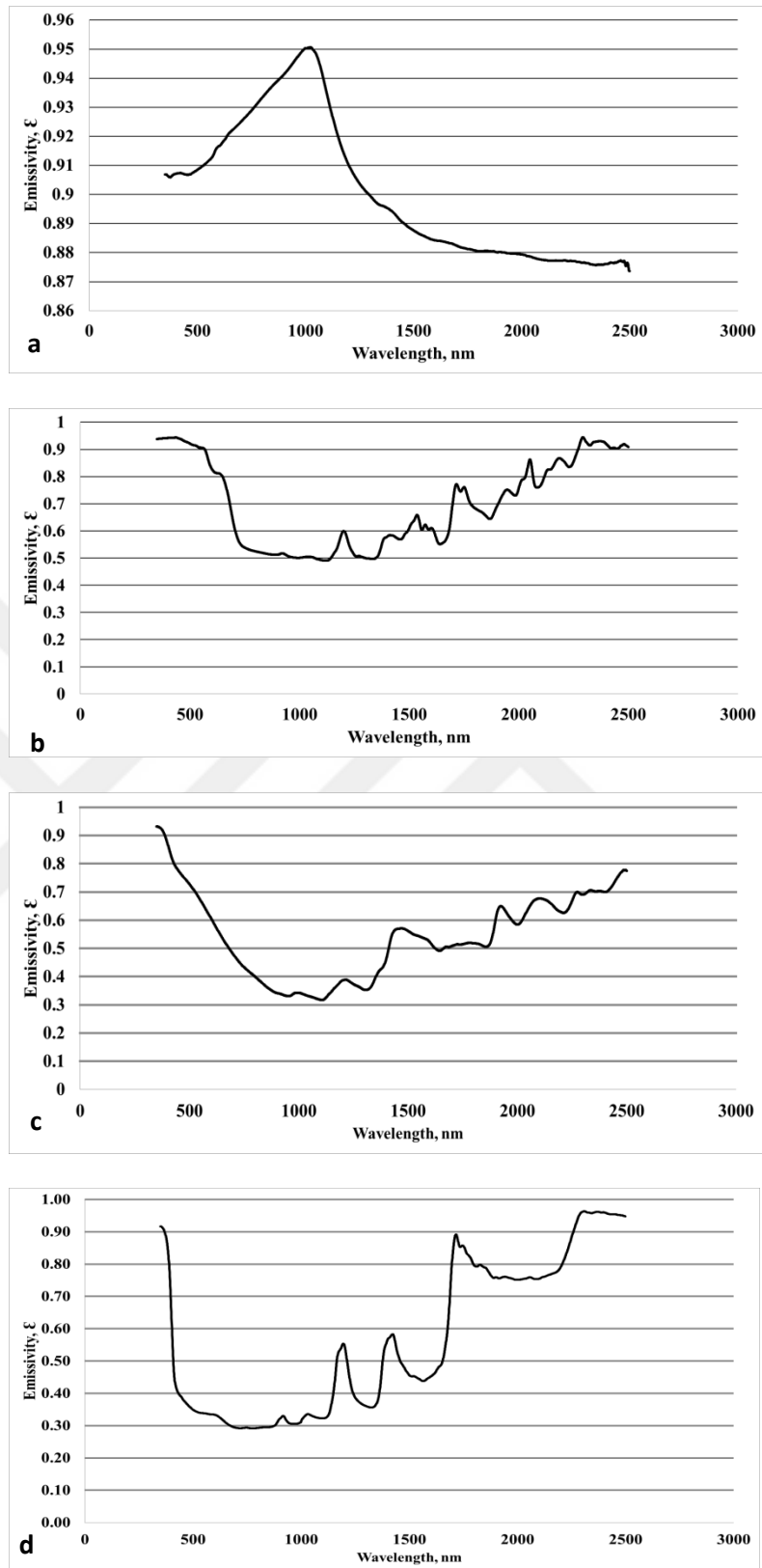


Figure 3.6 Spectral emissivity of surfaces was applied (a) steel sheet metal, (b) brown carpet, (c) wood, (d) the white paint [54],[55].

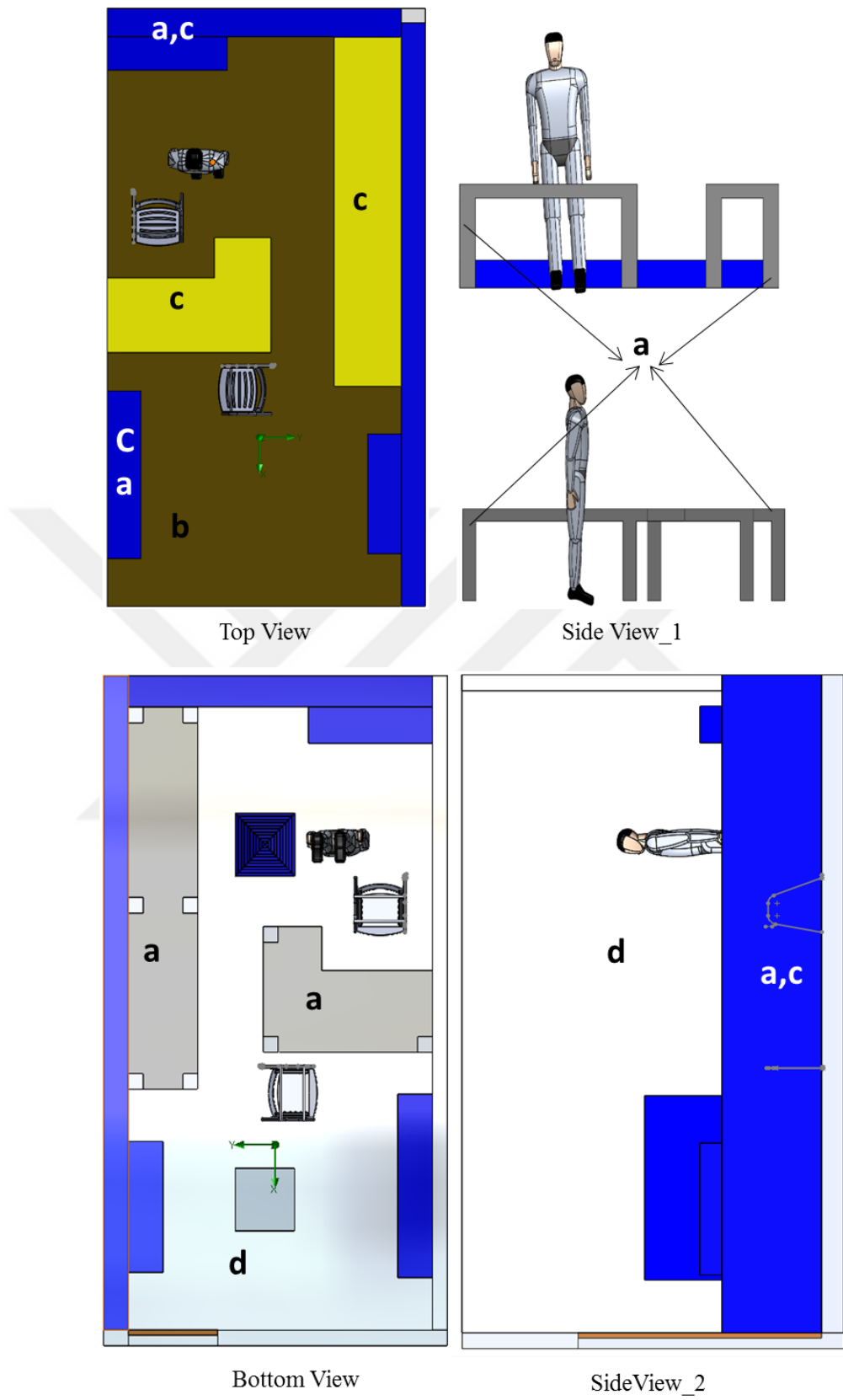


Figure 3.7 From the different perspective, notation of opaque surfaces.

3.3.1. Physical Properties of Window Glasses

Glass is the most important material that affects TC in the room considered in this work. Radiation from the sun or any other source travels in three different ways after reaching the glass. Some of these rays pass through the glass, some are absorbed by the glass, and some are reflected back. The ratio of light which passes through the glass is called transmittance. The spectral range of the light reaching the earth surface from the sun, is between 300 nm and 2500 nm. The spectral range that the human eye perceives as the visible light correspond 380 to 780 nm. About 50% of the energy reaching the earth within this spectral range which we call it as daylight. Therefore, the light that passes through the glass affects both the visual comfort and the TC levels [56]. Considering this effect of solar radiation, it is understood that the glass types used in the buildings are actively involved in energy consumption, TC and visual comfort levels.

In this thesis, simulations have been carried out for the room with three different glass types. Glass2 which is the material currently used in glasses of the windows in the room, is used in both the validation example given in the Chapter 4 and some of the comparison scenarios provided in Chapter 5. Furthermore, we have investigated the effect of the different types of glass on the radiation transmission, and the TC levels.

For the three types of glasses, the outward alignment of the glasses placed on the aluminum frame as double glazing is shown in Figure 3.8.

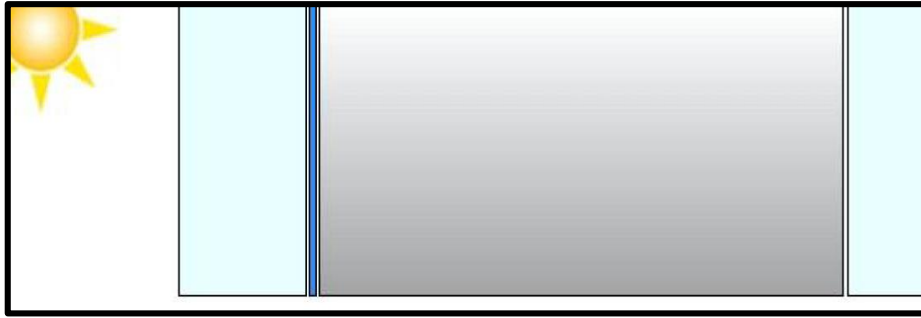


Figure 3.8 Glazing from external to internal for the total thickness of glasses is 24 mm.

Guardian is a software developed by Sun Guard named company and it is the software which calculates the physical properties of glass by making selection for company's own glass types. It has been used here to select glasses for different radiation transmittance. Details about the Guardian software and selected glasses are given in Appendix A.

Glass 2 was used as the benchmark scenario, while the radiation transmittance was ordered from high to low with Glass 1 having the highest and Glass 3 the lowest transmittance respectively. In Table 3, surface absorptions and reflectance values, along with the transmittance of all glasses, are shown, by taking the mean of wavelength range.

Table 3 Radiative properties of glasses

Transmissivity Level	Highest (Glass 1)		Middle(Glass 2)		Lowest (Glass 3)	
	Solar	Light	Solar	Light	Solar	Light
Direct Transmittance [%]	79,3	83,5	54,8	85	12,8	25,3
Direct Absorption [%]	6,5	15,1	26,8	11	47	13,1
Direct Reflectance [%]	14,2	1,4	18,4	4	40,2	61,6

Figure 3.9 shows the variation of the transmittance property of these glasses depending on the wavelength. The spectral distribution of absorption coefficient values calculated by Eq. (38) is depicted in Figure 3.10.

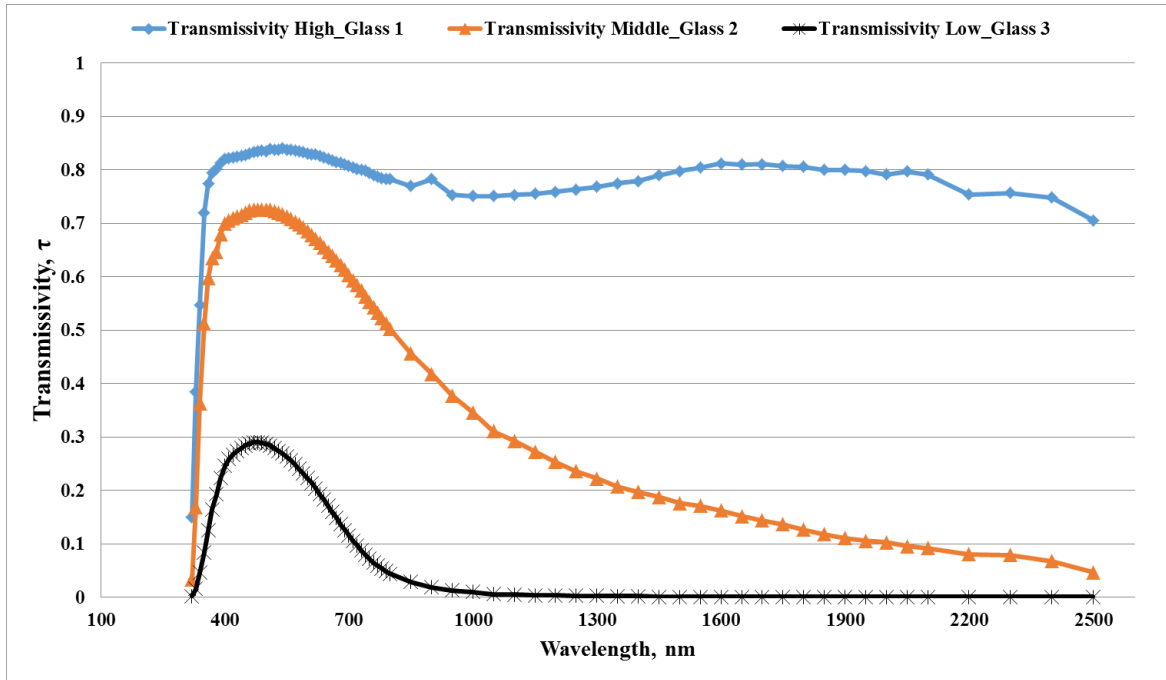


Figure 3.9 Spectral distribution of solar transmissivity for three glasses.

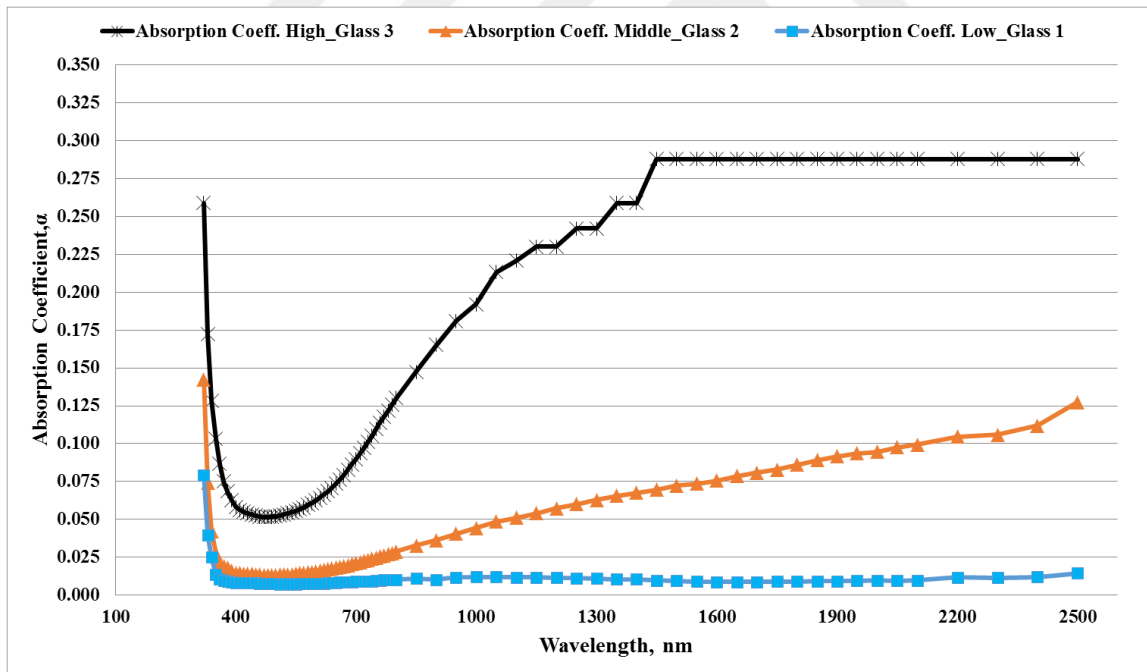


Figure 3.10 Spectral distribution of absorption coefficient for three glasses.

3.4. Experimental Measurements

These analyses focus on basic studies in two different scenarios. The first of these is the analysis of the current situation of the room for the working conditions of the month of March climate condition. The second one, summer time analyses is given for month of July. To analyze the validation scenario, benchmark simulation was performed in March. Also, some measurements were completed for the initial boundary conditions.

The averaged velocity value was measured in front of the diffusers, 1.93 m / s (Figure 3.11), the temperature was 26°C (Figure 3.12) and the relative humidity was around %32 (figure 3.13) at 10.00 am, on March 21.

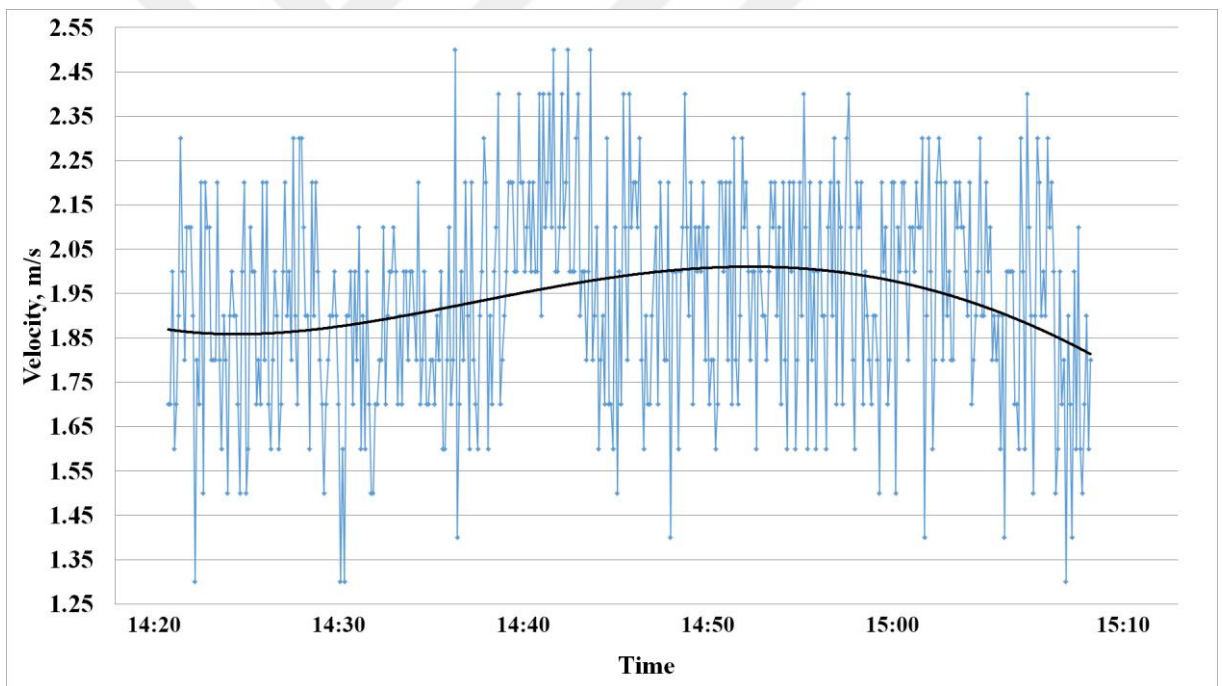


Figure 3.11 Velocity measurement on diffuser.

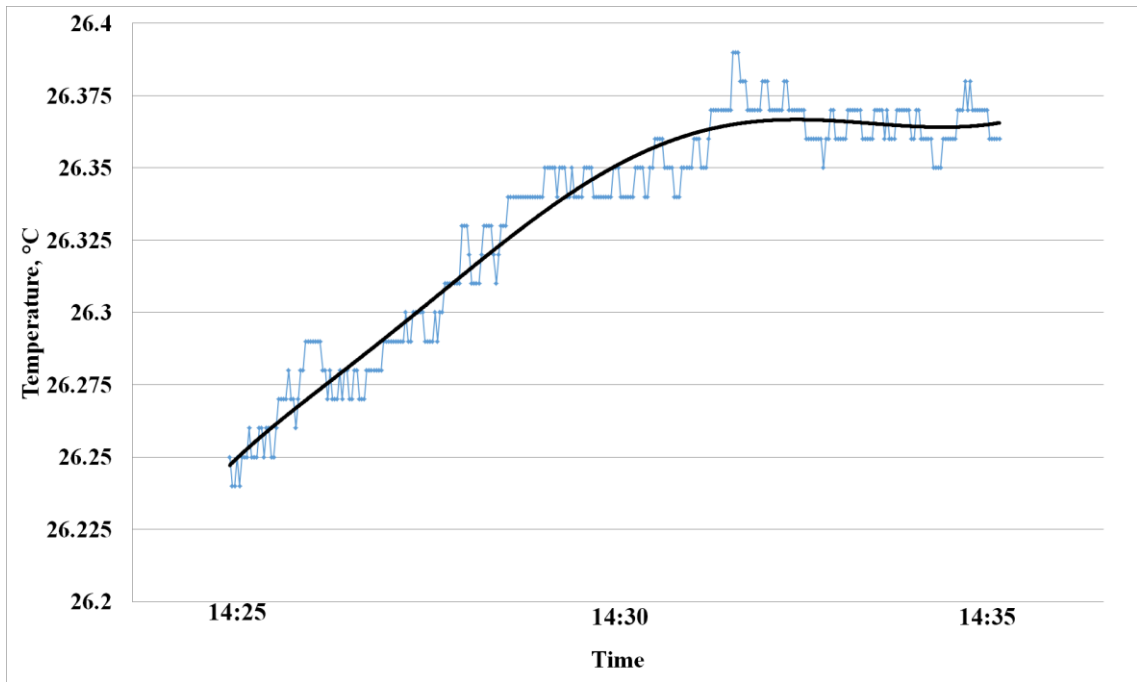


Figure 3.12 Temperature measurement on diffuser.

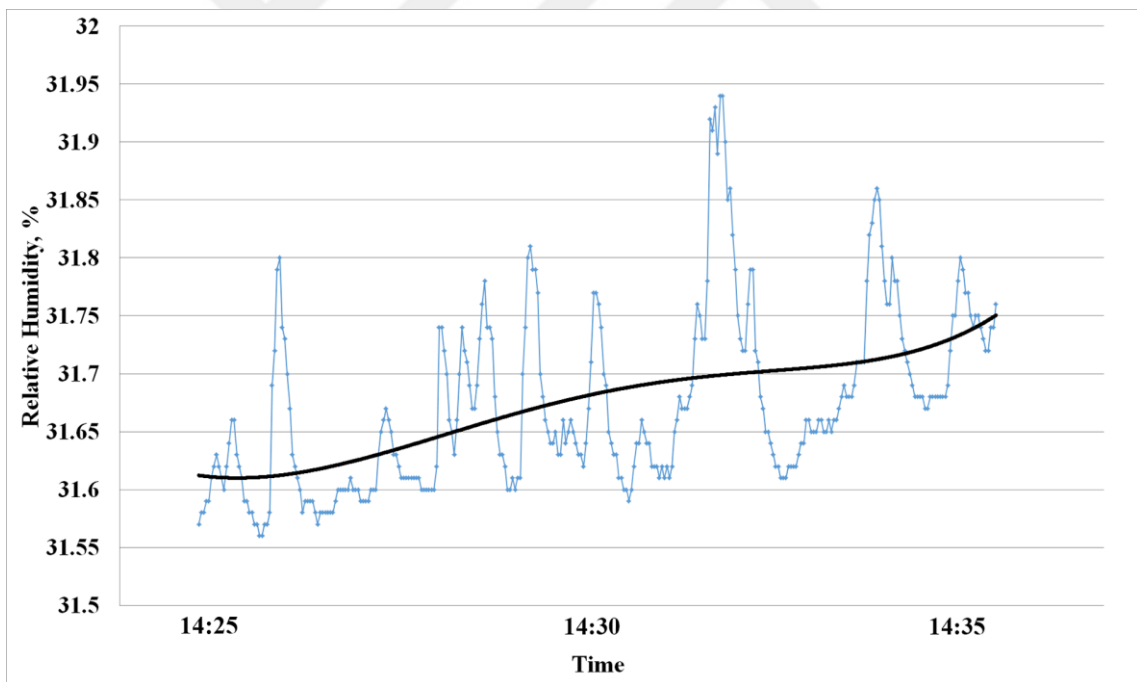


Figure 3.13 Relative humidity measurement on diffuser.

CHAPTER IV

SIMULATION STEPS

There are generally three stages in simulations performed by CFD method; Pre-processing, solving, and post-processing. The CFD simulations conducted in this thesis, also followed the same steps. In this chapter, all simulation steps are shown and discussed. Figure 4.1 depicts a flowchart which demonstrates step by step simulation process of this work.

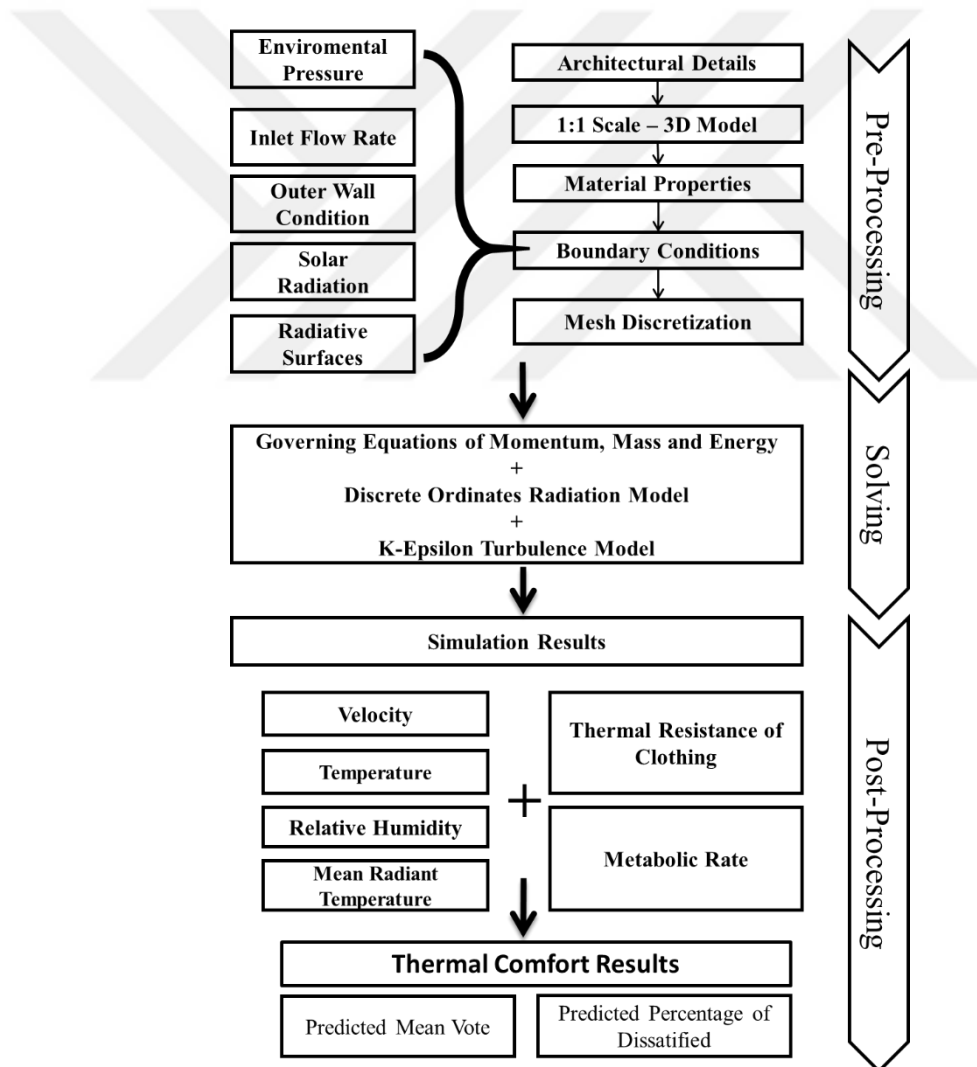


Figure 4.1 Flow chart of simulation steps.

4.1. Benchmark Analysis and Boundary Conditions

The first simulation study was initiated on March 3, with measurements of an indoor wall, glass temperatures and outdoor climate conditions. The definition of materials and surface properties given in the previous sections (3.3) and the boundary conditions for different surfaces are also given. The benchmark analysis was performed at 11.15 am and it was simulated as a steady-state case in order to be able to analyze the distribution of the air from the diffusers. Moreover, the numerical and experimental results will be compared in the following sections.

4.1.1. Inlet and Outlet Flow Rates

The information on the air change per hour which can be conveyed into the room by the fan coil device used in the room air conditioning is obtained from the mechanical installation designer of the building. With this information, in order for the device to work in a 3D simulation model, the air flow rate of $0.148 \text{ m}^3/\text{s}$ is directly defined on the upper surface of the diffuser, as depicted in Figure 4.2. There is a second diffuser at the ceiling height as shown in Figure 4.3, to allow the air blown into the room to reach the fan coil device again. With the negative pressure generated by the fan coil device in the suspended ceiling, the processed air in the room passes through this secondary diffuser and returns to the fan coil device. The blades on the second diffuser surface are not modeled in the simulations since they cannot affect the indoor air flow circulation.

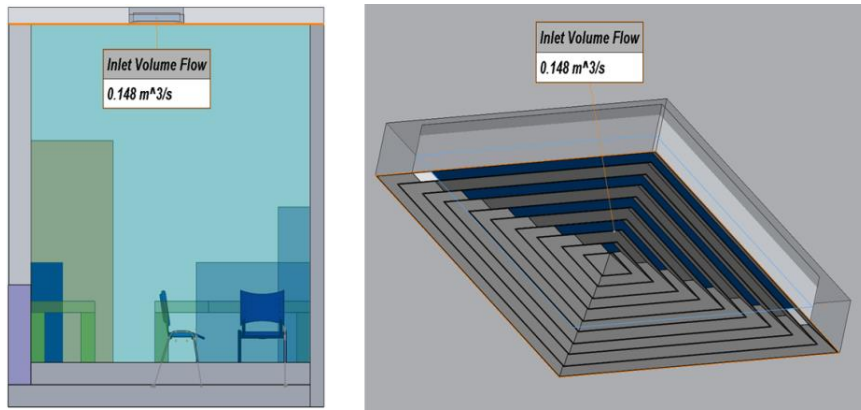


Figure 4.2 Flow rate boundary condition on diffuser.

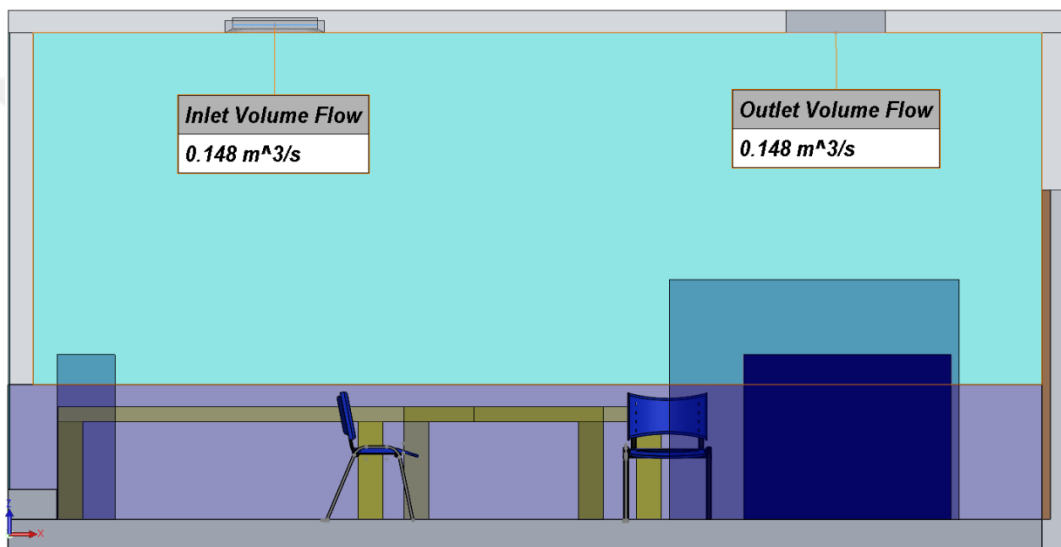


Figure 4.3 Definition of air flow rate on diffusers.

4.1.2. Effect of Environmental Pressure

The door of room considered for our simulations is generally open. In simulations, if there is an inlet or outlet boundary condition, the parameter of the pressure must be defined and it is necessary to solve the conservation of mass equation. In practice, some pressure cracks may exist under the door, filtration from the windows or the adjacent room. For this reason, the door between the room and the adjacent office is considered as an interface in the simulations. Therefore the interior temperature and pressure

conditions of the side offices are defined all over the door surface, as shown in Figure 4.4. In the analysis, the indoor pressure values for the room and the adjacent room were specified as 101325 Pa and the adjacent room temperature was measured as 26°C.

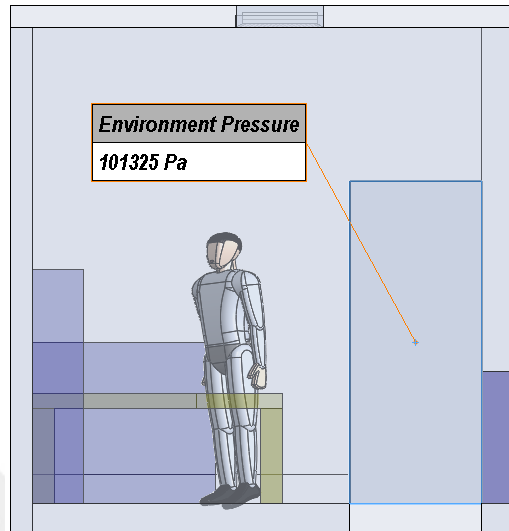


Figure 4.4 Definition of environmental pressure on door surface.

4.1.3. Effect of Wall Boundary Conditions

We have two different boundary conditions associated with walls in our simulations, as shown in Figure 4.5. The first of these is the boundary condition considered for the wall between the analysis room and the adjacent office wall (inside wall) and the second boundary condition is associated with the other walls atmospheric conditions (outside wall). Depending on the outdoor climatic conditions, the temperature is assumed at fixed 15.6 °C temperature is defined on the outside wall surfaces. Measured wind speeds at outside is shown in Figure 4.6 and the heat transfer coefficient is assumed as 5 W/m²K, as discussed in [57].

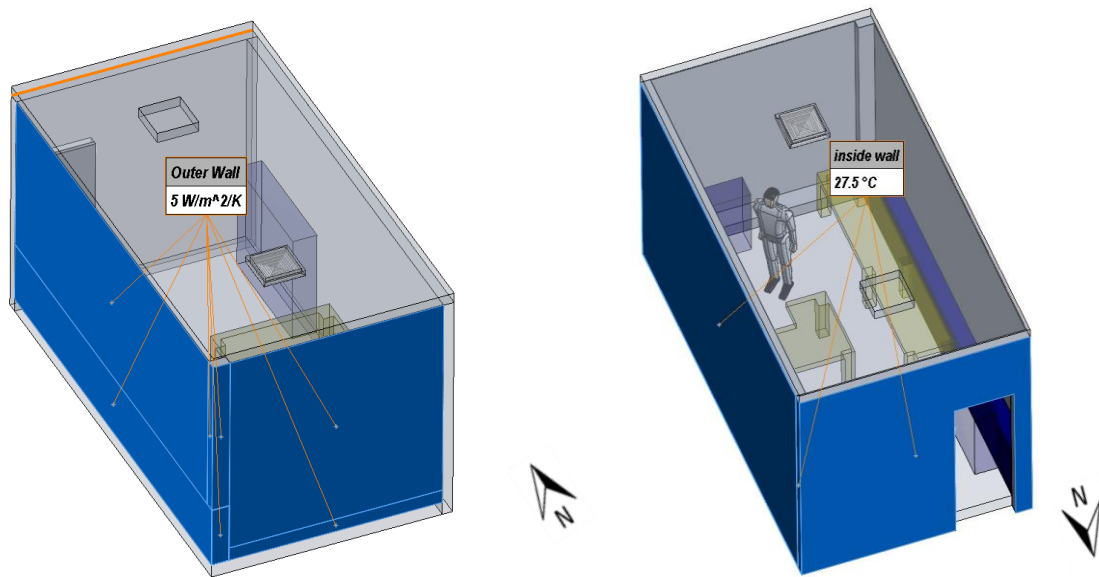


Figure 4.5 Boundary conditions on walls.

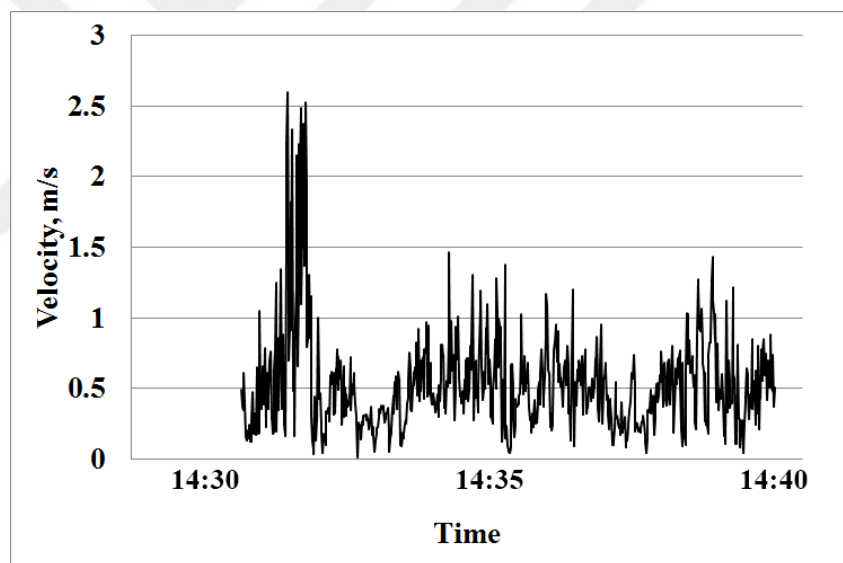


Figure 4.6 Outside wind speed data measured on March 3.

4.1.4. Effect of Solar Radiation and Environment Temperature

General information on calculation of solar radiation is given in section 2.1.1. Location information used in the benchmark analysis of radiation values, latitude; 41°03', date; 03/03/2017, zenith direction (opposite of gravitational direction); Z axis, and angle measured from the north to X axis; -10.98°, can be seen in Figure 4.7.

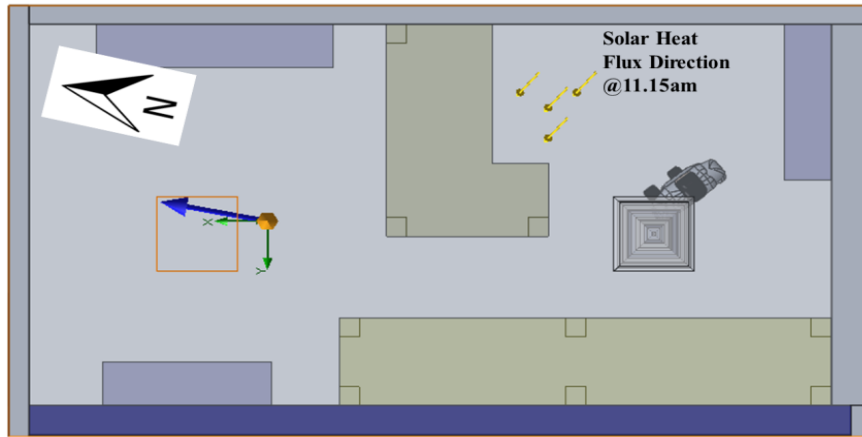


Figure 4.7 Solar heat flux direction and orientation in the analysis room.

When the outdoor environment is completely covered with clouds, cloudiness level is assumed as 1, while in a clear sky, it is counted as 0. In the benchmark analysis, it is assumed that the weather is partially cloudy at 11.15 am. In the literature, the solar heat flux value for a partially cloudy sky in Istanbul has been identified for the month of March [58] and measurements' results for a complete day is shown in Figure 4.8. The results obtained at 11.15 am measures heat flux as 620 W/m^2 .

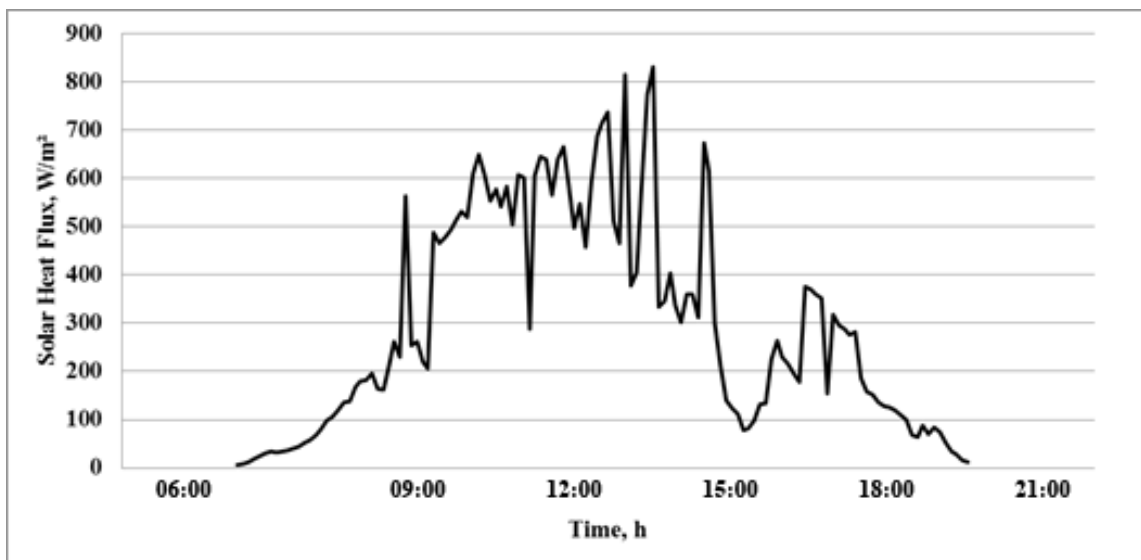


Figure 4.8 Solar heat flux data which was collected by the device on the roof of the building on horizontal plane. It was obtained by the university weather data station.

Environment temperature can be calculated by using the Eq. (23). Ambient air temperature was measured as 16.2°C and relative humidity for outside is 53%. As a result, T_E (environment temperature) was calculated as -3.2°C.

4.1.5. Assumptions and Mesh Discretization

Based on the finite volume approach, the direct discretization of the integral form of the conservation laws was used. It guarantees that basic quantities of mass, momentum and energy remain conserved in the discretized representation. The spatial derivatives were approximated with implicit difference operators of second-order accuracy [52]. The time derivatives were approximated with an implicit first-order Euler scheme. The numerical viscosity generated by the discretization error of the scheme was small and allows obtaining adequately accurate results in the simulations.

Computer program automatically generates a rectangular mesh in the computational domain and separates the fluid and solid domains. The corresponding computational domain was generated in the form of a rectangular parallelepiped, enclosing the model for 3D analysis. In the mesh generation preparation, the computational domain was divided into uniform rectangular parallelepiped-shaped cells (cut-cell mesh), which form a so-called basic mesh. Then, by using data of the geometry model and the specified boundary conditions of the software various mesh refinements were constructed, i.e. splitting of the basic mesh cells into smaller cells, in order to better represent the model and fluid regions. The mesh, which the calculation was started from, so-called initial mesh, was fully defined by the generated basic mesh and the refinement settings. A computational mesh separates the computational domain with a set of planes orthogonal to the Cartesian global coordinate system's axes to form

rectangular parallelepipeds called cells. The original parallelepiped cells containing boundaries were separated few parts that were referred to only one fluid or solid medium. The resulting computational mesh contained cells of the following types; fluid cells in the fluid, solid cells in the solid and solid-fluid cells partly in the solid and partly in the fluid. Some parts of the domain are shown in the Figure 4.9.

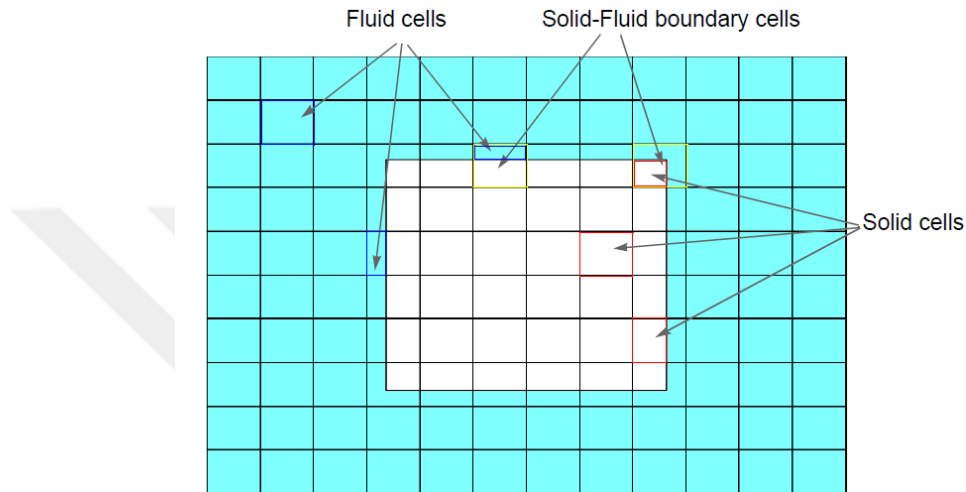


Figure 4.9 Solid, fluid and solid-fluid cells in the computational domain.

Completed for the benchmark analysis, the main reference location to determine the sufficiency of mesh quality, has been set to blown diffuser point. For this reason, the analysis was repeated by applying 3 different mesh options. As the coarse mesh type is changed to a very fine mesh type, the numbers of applied cells were increased. In Table 4, the number of fluid, solid and total elements for the mesh quality applied for each analysis is given.

Table 4 Number of the cell need for mesh independency

Mesh Details	Coarse Mesh (a)	Fine Mesh (b)	Very Fine Mesh (c)
Fluid Cell Number	39145	64886	284762
Solid Cell Number	63792	87945	124240
Total Cell Number	102937	152831	409002

There are different calculation methods in the literature for determining mesh quality [59]–[62]. The verification example in the previous section was completed for this study and the impact of the “very fine mesh” would be directly compared with the experimental results. Also shown in Figure 4.10 is a cross-section view of the mesh, passing through the center of the diffuser. The mesh distribution details over the marked region are depicted in Figure 4.10, and further details are shown in Figure 4.11.

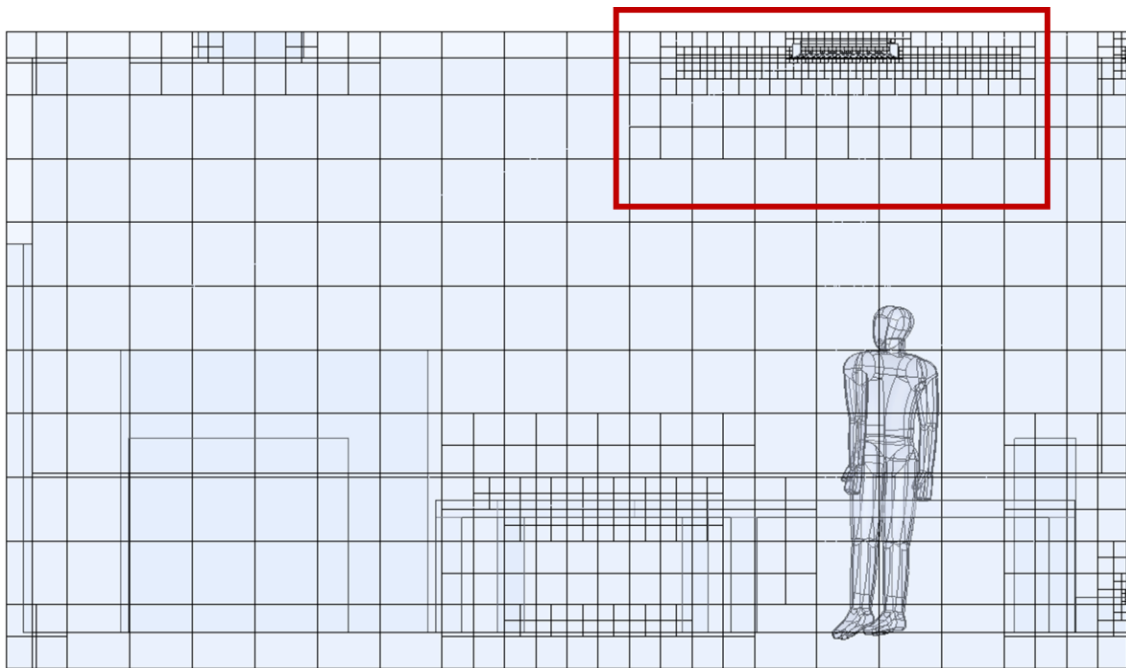


Figure 4.10 Cross-sectional mesh distribution in the room. Results of mesh dependency were tested and this mesh size accepted for analysis in the room and close to the diffuser blades.

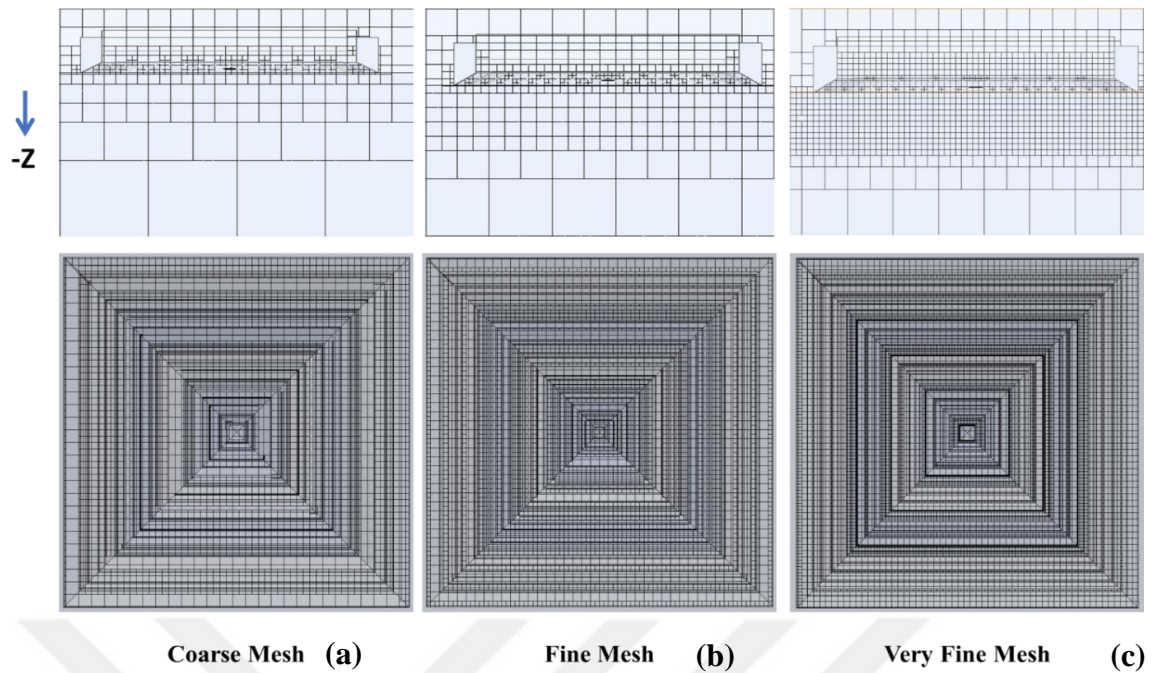


Figure 4.11 The cross-sectional view of the mesh and surface mesh distribution of diffuser. From coarse mesh to very fine mesh, number of cells were increased between the diffuser blades. Validation study shows the importance of this improvement to obtain meaningful velocity consistency between experimental and simulations results.

4.2. Results for Benchmark Simulation and Validations

In the following sections, we will provide two different validation scenarios, one is based on the literature review and one is based on the experimental measurements performed in this work.

4.2.1. Validation of Results

As we know from the literature, a number of experimental and numerical studies have been carried out on the average convective heat transfer coefficient on a completely nude manikin surface. When air velocity is less than 0.1 m/s in an environment, heat transfer with convection from human body to air depends on the on temperature gradient [63]. The human body model considered here has a surface area of 1.83 m^2 and

the height of 1.8 m. In order to compare our numerical results with the existing results in literature, in this validation scenario, solar radiation effect is neglected and all boundary conditions consider very fine mesh option as discussed earlier. In all the other TC simulations, we do not include the human body in heat transfer calculations.

As shown in Figure 4.12, heat transfer coefficient h_c , on the surface of human body is between $1.6 \text{ W/m}^2\text{K} < h_c < 5.5 \text{ W/m}^2\text{K}$. Also, average heat transfer gives $3.58 \text{ W/m}^2\text{K}$ on full body. Table 5 gives the literature data for standing human body convective heat transfer coefficient in still air environment [11], [64].

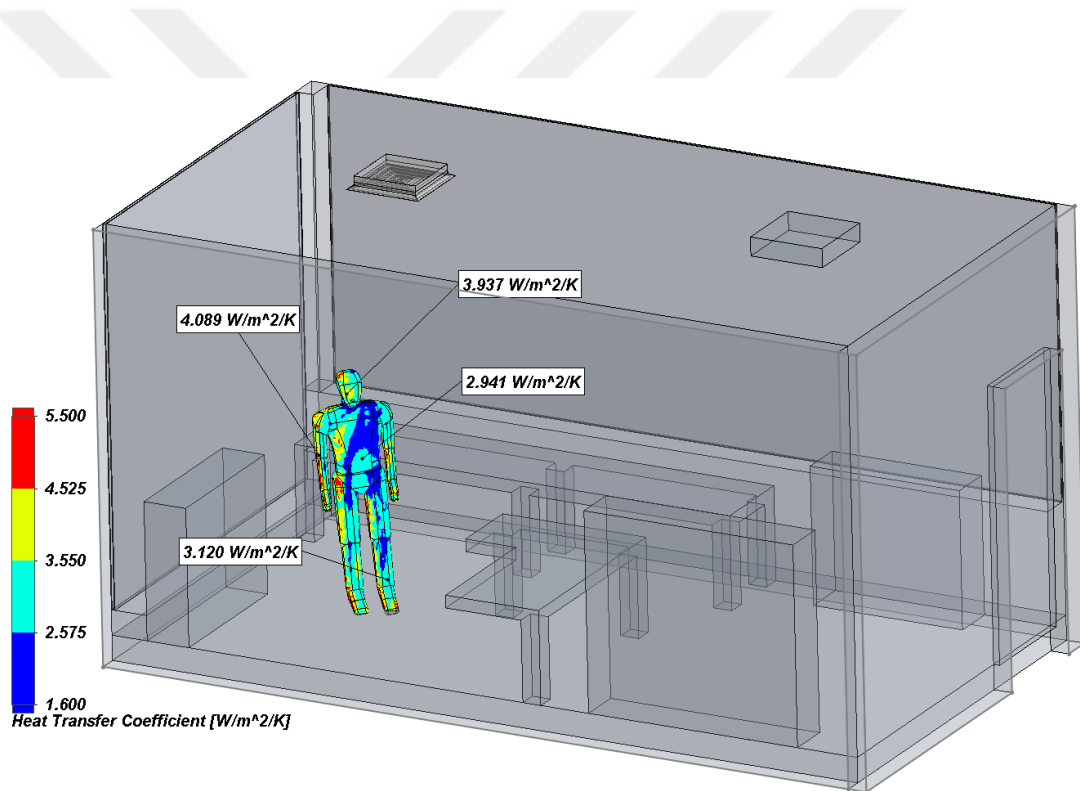


Figure 4.12 The convective heat transfer coefficient on human body, under the still air condition (air velocity near the body is less than 0.1 m/s) in room environment.

Table 5 Convective heat transfer coefficient comparison for whole standing body in still air ($<0.1\text{ m/s}$) [63].

Authors	Method	h_c (W/m^2K)
Stolwijk (1970)	Experiment	3.37
De Dear et al.(1997)	Experiment	3.4
Danielson (1993)	Experiment	3.6
Bolineni et al. (2015)	CFD	3.65
Brohus (1997)	Experiment	3.86
Murakami et al. (1995)	CFD	3.9
Fidan et al. (2017)	CFD	3.58

4.2.2. Experimental Results and the Error Rate

When investigating the results of the three different mesh sizes, out of the three, the numerical results obtained with ‘very fine mesh’ and the experimental results show great agreement. Figure 4.13 shows that the average velocity obtained by experimental measurements (Figure 4.14) at the edge of the diffuser is at 1.9 m/s as shown in Figure 4.14.

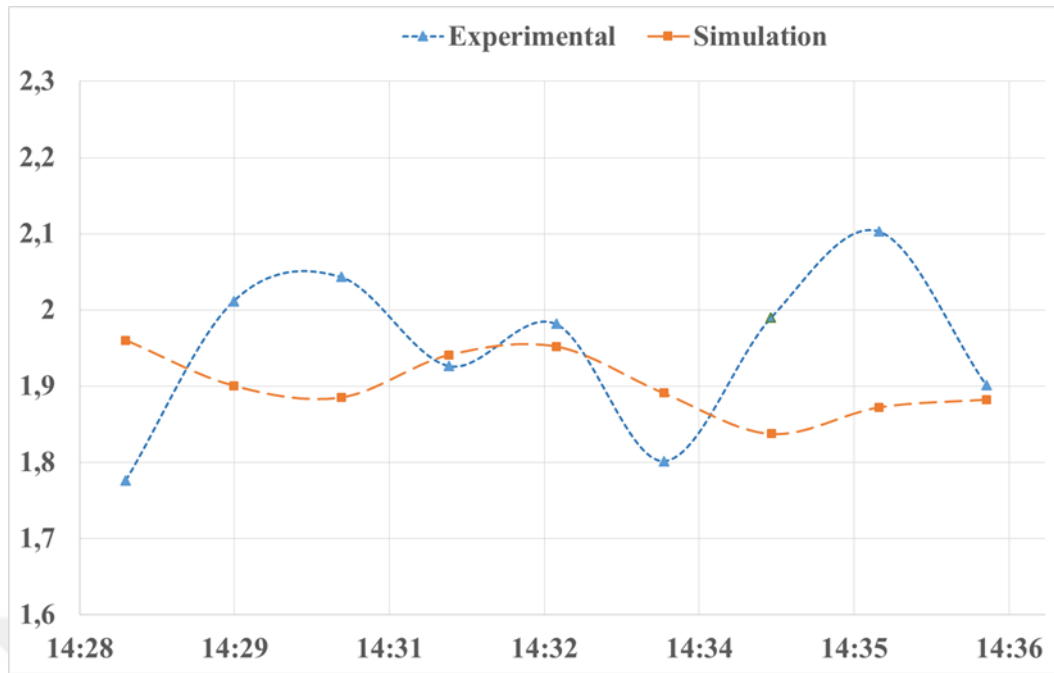


Figure 4.13 Measurement of velocity at diffuser level.



Figure 4.14 Air velocity measurements at diffuser height.

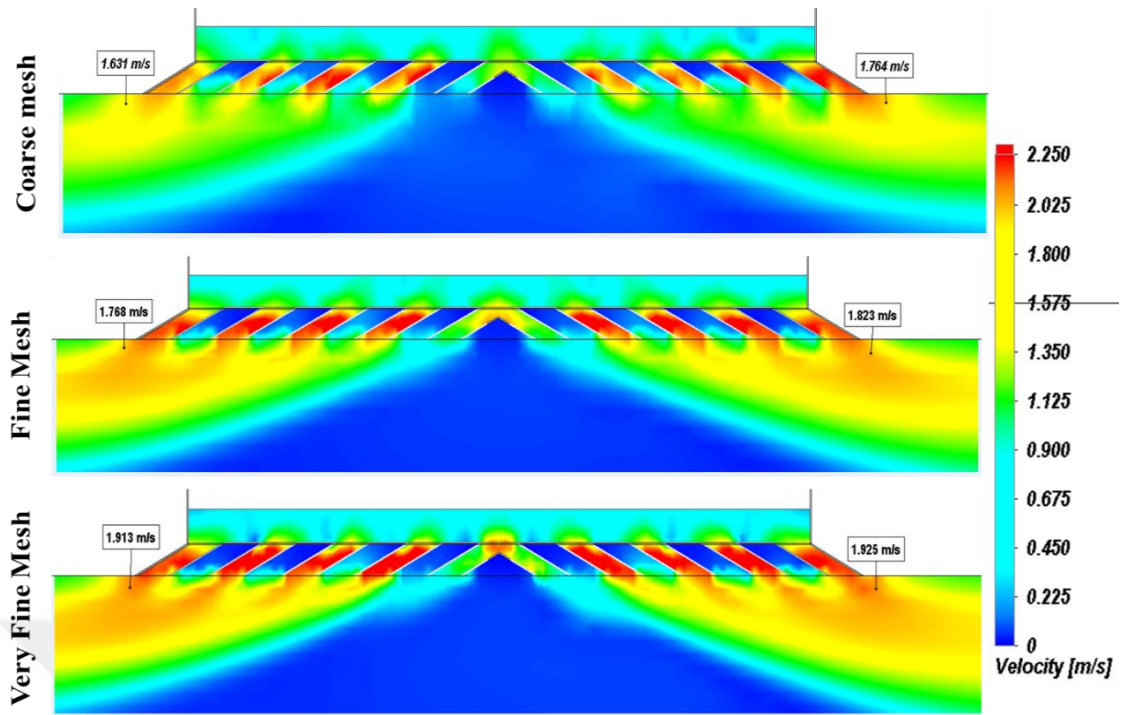


Figure 4.15 Cross-section side view on diffuser and the comparison of velocity distribution with different mesh types, coarse mesh to very fine mesh.

In Figure 4.16, the velocity was measured where the user of the room seats and the numerical results obtained with “very fine mesh” test was in better agreement with each other than the results obtained with other mesh sizes as shown in Figure 4.17.

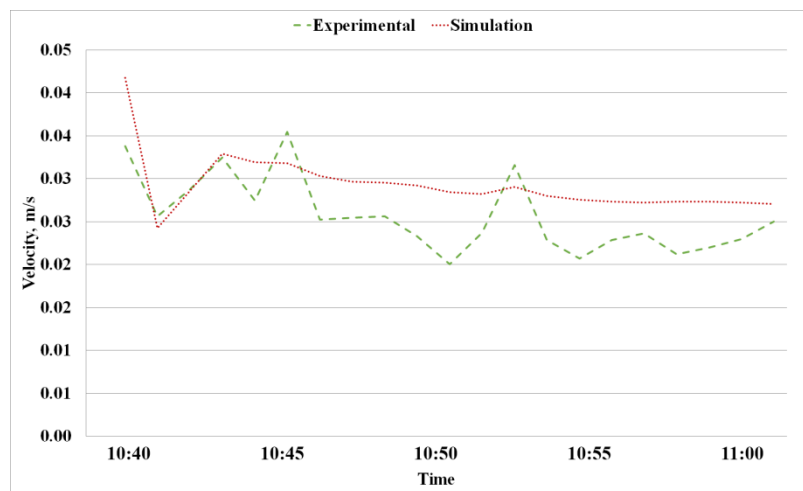


Figure 4.16: Measurement of velocity at the seat location.

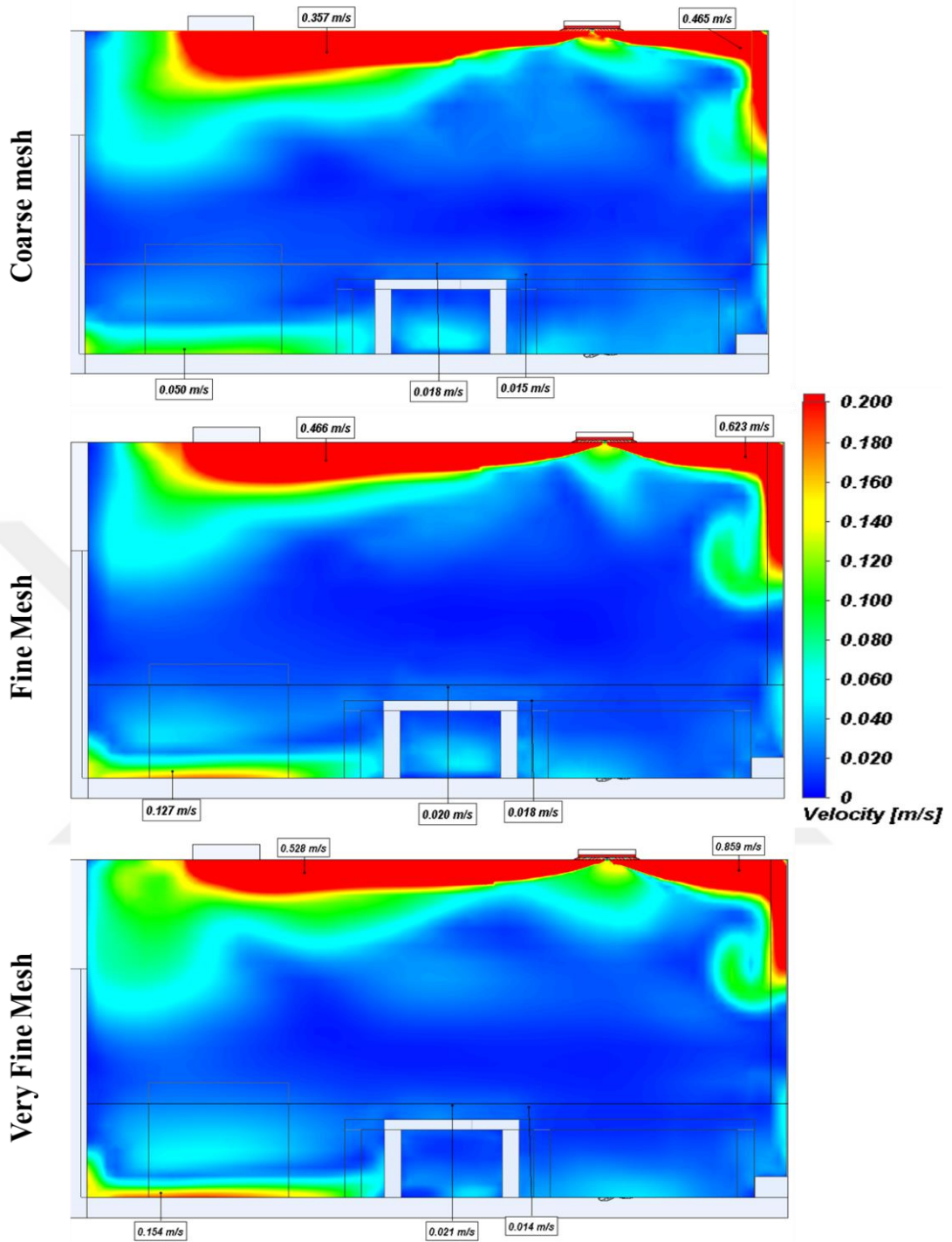


Figure 4.17 Cross-sectional side view on diffuser, comparison of velocity distribution with different mesh types.

The experimental measurements of the temperature of the glass surfaces, compared with the simulation results are shown in Figure 4.18. All completed simulations are based on numerical methods. The error rate calculation were performed to investigate the

correlation between numerical results and experimental studies [65]. Numerical errors can be divided into two categories on truncation errors round-off errors. Truncation errors occur when approximations are used to represent the exact mathematical approaches. The round-off errors happen when numbers having limited significant figures are used to represent the exact numbers. For both types, the relationship between the exact, or true, result and the approximate value can be given as

$$\text{True Value} = \text{approximation} + \text{error} \quad (55)$$

By realigning the equation (47) we find that the numerical error is equal to the discrepancy between the truth and the approximation, as in

$$E_t = \text{true value} - \text{approximation} \quad (56)$$

where E_t is used to denominate the exact value of order. The subscript t is included to designate that this is the “true” error. One shortcoming of this definition is that no account is added to the rank of the value being examined. One way to take into account the order of magnitudes is to normalize the error to its true value, as described below:

$$\text{True fractional relative error} = \frac{\text{true error}}{\text{true value}} \quad (57)$$

where, as itemized by equation (48), we can write

$$\text{error} = \text{true value} - \text{approximation}$$

The relative error can also be multiplied by 100 percent to express it as

$$\varepsilon_t = \frac{\text{true error}}{\text{true value}} 100\% \quad (58)$$

The consistency between the experimental results and the simulation results were examined using the error rate calculation method described above. In comparing the velocity values in the seating area for simulations and experiments, the average error order was calculated to be 14%, (Figure 4.16). When the same comparison was completed for the diffuser height measurements (Figure 4.13), the average error rate was calculated as 5%. The temperature values obtained on the surface of the glass after the simulation were also compared with the results measured by thermocouple on the inner glass surface on the south façade, as depicted in Figure 4.18. The average error order is below 1% when compared to the experimental measurements and numerical analysis of the temperature of the glass surface.

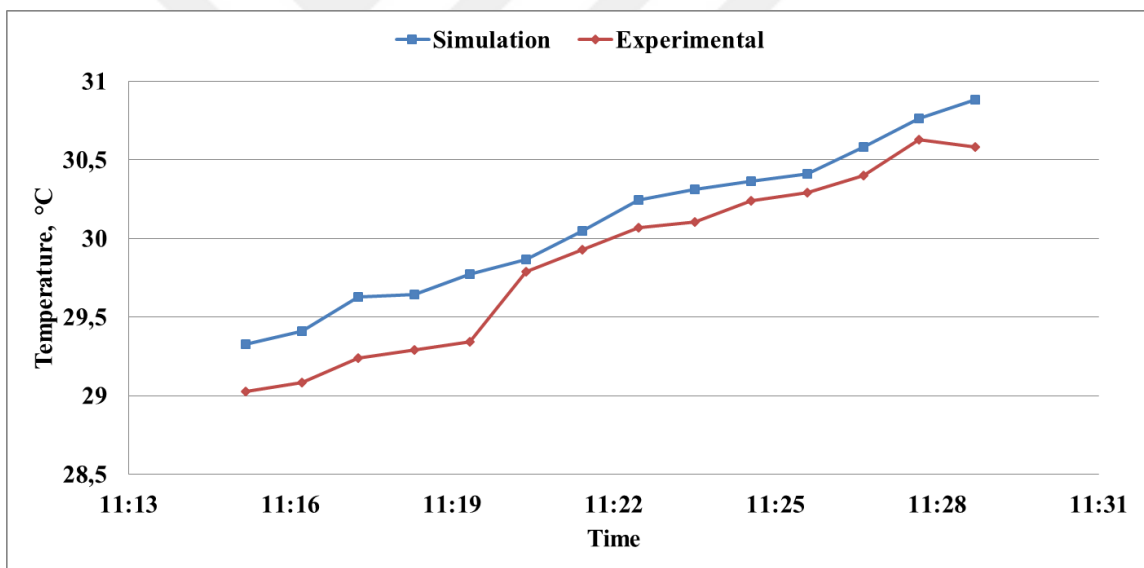


Figure 4.18 Comparison of experimental and simulation results for temperature of the surface of glasses.

CHAPTER V

INVESTIGATION OF THERMAL COMFORT IN DIFFERENT SCENARIOS

In this chapter, we provide a detailed transient analysis for temperature in the demonstration room, assume that the room receives solar radiation between 9:00 to 17:00 and is occupied during these hours. The analyses were performed on 21st of July. The main reason for choosing this summer day is that due to the feedback obtained from the user of the room, the level of thermal discomfort on this day is very high, due to received intense solar radiation. During this period, all outdoor climate and indoor boundary conditions are considered fixed and the only varying factor is the change of the angle of the sun, which changes the intensity of the solar heat flux. These transient analyses should be without interruption to understand the effect of materials' heat capacity on TC. As solved in benchmark scenario, the analyses can be completed solving the processes of convective mass, momentum and energy transport together. However, the computational cost of solving each governing equation together is so expensive for during the time 9:00 to 17:00. Instead of this method, flow freezing approach was applied with these analyses of comparison scenarios.

FloEFD makes available the flow freezing alternative that provides you to freeze, the pressure and velocity field while continuing the calculation of temperature and composition. This approach is particularly functional in solving steady-state problems including diffusion processes that are significant from the user's attitude, e.g. heat propagation in dead zones of the flow. Transient analyses with nearly steady-state velocity fields and diffusion processes developing with time are also samples of this

type of problems. As a result, the CPU time for solving such problems can be considerably reduced by applying the flow freezing approach. Therefore, in the comparison scenarios of this section for the solar radiation time (09:00 to 17:00) flow freezing approach was applied in analyses. During the 5 minutes, the equations of flow and heat transfer were solved together and after than flow was fixed and only heat transfer calculation was continued during 30 minutes. The period was iterated during the 8 hours. The period of flow freezing approach is shown in Figure 5.1.

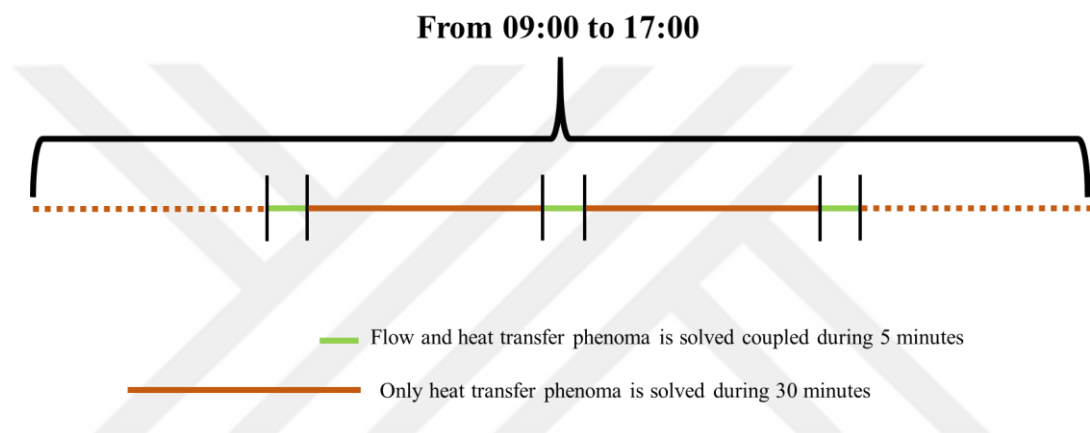


Figure 5.1 Time period of applied flow freezing approach. It shows with short lines, 5 minutes for solving the all governing equations and long lines 30 minutes for solving only the governing of energy equations. This loop was repeated during the 8 hours in all scenarios.

We compare four different scenarios in three of which, three different glass materials (Glass 1, Glass 2, and Glass 3) are used. The difference of the glasses comes from their level of the transmissivity. It is realized that the Glass 1 material has the highest level of transmissivity. Glass 2 material has the middle level of transmissivity and Glass 3 has the lowest level of transmissivity. Among these materials, we have chosen Glass 2 for the benchmark scenario, as discussed previously in Chapter 3. In the fourth scenario, the comfort level is investigated by trying to improve the TC in the entire room, instead of only focusing on the areas where the user is usually present at. In

order to achieve this goal, a new diffuser has been designed to replace the existing diffuser, and the air has been directed towards the users' whereabouts. In the fourth scenario, Glass 3 material is used together with the new diffuser design. Details of the scenarios are given in Table 6. Finally, the comparison of the results is shown by investigating the PMV and PPD.

Table 6 Comparison scenarios are detailed with variable materials.

Scenarios	1	2	3	4
Variable Condition & Material	Glass 1	Glass 2	Glass 3	Glass 3 + New Diffuser

5.1. Assumptions for Boundary Conditions in Summer Time

According to the information received from the mechanical installation design company for this room, the boundary conditions were applied assuming a clear sky on the day of July 21st. We have considered a series of fixed boundary conditions which we list below:

- Diffuser blowing temperature is set to 19 °C.
- Flow rate of fancoil at diffuser inlet surface is 0.148 m^3/s .
- Initial inner surface temperature of inside wall is constantly 28 °C.
- Three different glasses with different transmissivity levels (Glass 1, Glass 2, Glass 3) are used.
- The emissivity values of the material surfaces were applied spectrally as given in the chapter 3.

- Outside air temperature is accepted as 29 °C as suggested in [66], [67]. It's temporal condition shown in Figure 5.2.
- The following simulations are based on “very fine mesh” that results in 409002 total cell number (as provided in Table 4).
- All other initial boundary conditions are considered the same as the validation case scenario given in Chapter 4.
- Metabolic rate of a person is assumed as 60 W/m². Activity definition of this value is “seated quite” from ASHRAE standard about thermal comfort [68].
- Thermal resistance of clothes for summer season is 0.57 clo (0.08835 m²K/W). This clo value corresponds to trousers and short-sleeved shirts [68].

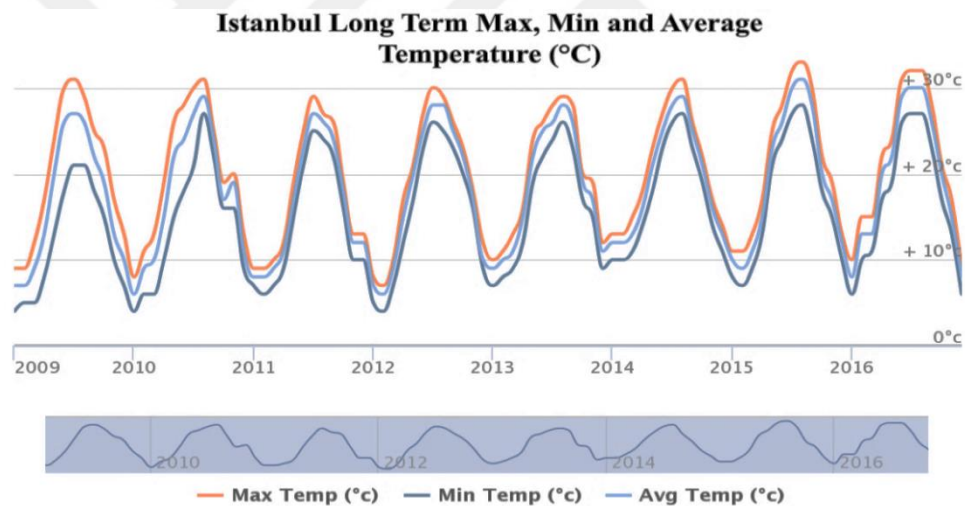


Figure 5.2 Maximum, minimum and average long term outdoor air temperature for Istanbul from 2009 to 2017 [67].

In all completed analyzes in this Chapter, the TC comparisons according to the above listed boundary conditions, applied in the same way, are visually and graphically compared.

5.2. Comfort Zone Specifications

In this section, we first define the area within the test room which is considered as the comfort zone. In non-residential spaces, the requirements for the indoor environment shall be satisfied in the occupied zone. This means that all measurements dealing with comfort criteria should be related to the occupied zone. The total area of a room can be used to evaluate the requirements, but the comfort criteria are not guaranteed beyond this zone. We define this area based on the information provided in Table 7 which assumes a specific distance from the wall, windows and floor, etc. which marks the virtual boundary of the thermal comfort zone [69] as depicted in Figure 5.3.

Table 7 Comfort zone general distance from the room boundaries.

Distance from the inner surfaces	Default Values (m)
Floors (lower boundary)	0.05
Floors (upper boundary)	1.8
External windows and doors	1
HVAC appliances	1
External Walls	0.5
Internal Walls	0.5

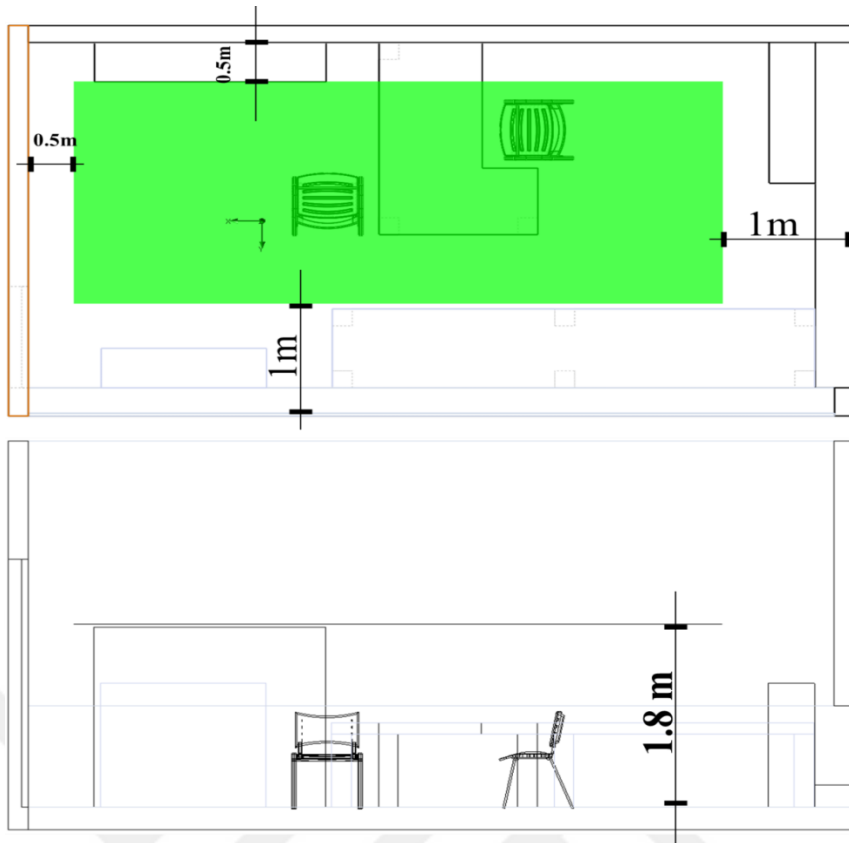


Figure 5.3 Comfort zone virtual boundaries in the test room.

The comfort zone defined here covers two different zones categorized as Zone 1 and Zone 2. Zone 1 is generally used by the room's owner and Zone 2 is used by the guests as shown in Figure 5.4.

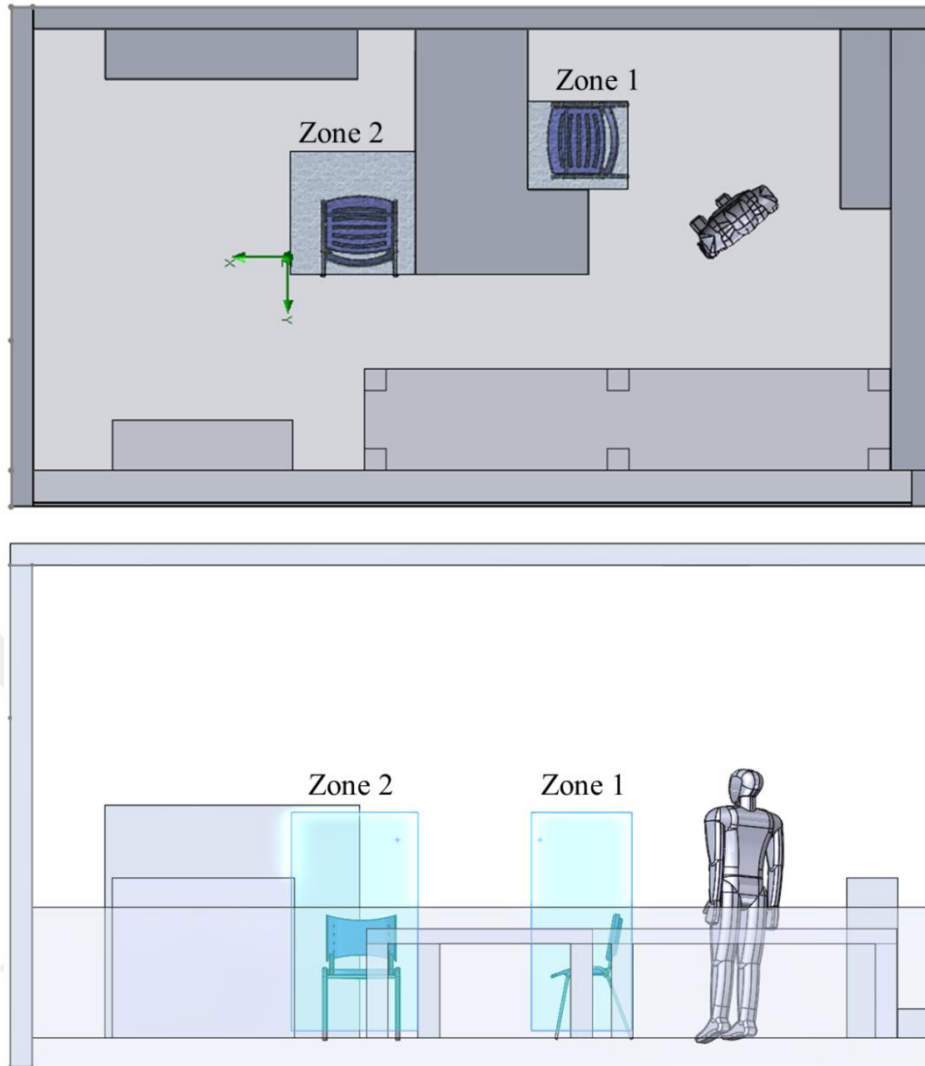


Figure 5.4 There are two chairs in this room and occupants generally stay in these locations. One of them is Zone 1 and other is the Zone 2.

The cross-section images parallel to floor are visualized according to the numerical results obtained at one hour intervals within the comfort zone. Images in the sequence, air temperature, MRT, OT, relative humidity, PMV and PPD distribution are given in Appendix B.

The MRT is calculated from the Equation (59);

$$T_r^4 = \frac{1}{4\sigma} \int I_{diffuse}(\Omega) d\Omega + \frac{1}{4} \sum I_{sun} \quad (59)$$

where $I_{diffuse}$ is the intensity of thermal radiation ($W/m^2/rad$) and I_{sun} is the intensity of the solar radiation (W/m^2). OT is a simplified measure of thermal comfort calculated by air temperature, MRT and air speed which is shown by T_{OT} and calculated as given by Equation (60):

$$T_{OT} = \frac{T_r + T\sqrt{10V}}{1 + \sqrt{10V}} \quad (60)$$

where T_r is the MRT, T is the fluid temperature and V is the air velocity.

5.3 New Diffuser Design for Scenario Four

In this scenario, the effect of the new diffuser design on TC is examined. Instead of a diffuser which blows air into four different directions in the benchmark, a new diffuser is designed to blow air directly to the whereabouts of the occupants. The new diffuser can be obtained by changing the positions and angles of the blade parts used in the current diffuser. The applied flow rate is kept constant. However, by increasing the gaps between the blades, the grill outlet blowing speed is reduced. The speed of air in the comfort zone has a limit and should not exceed the $1.2 m/s$ in comfort zone [70]. There are two different angles for the blades. While one section aims to blow Zone 1, the others are directed to the Zone 2. The new diffuser and air flow distribution are shown in Figure 5.5.

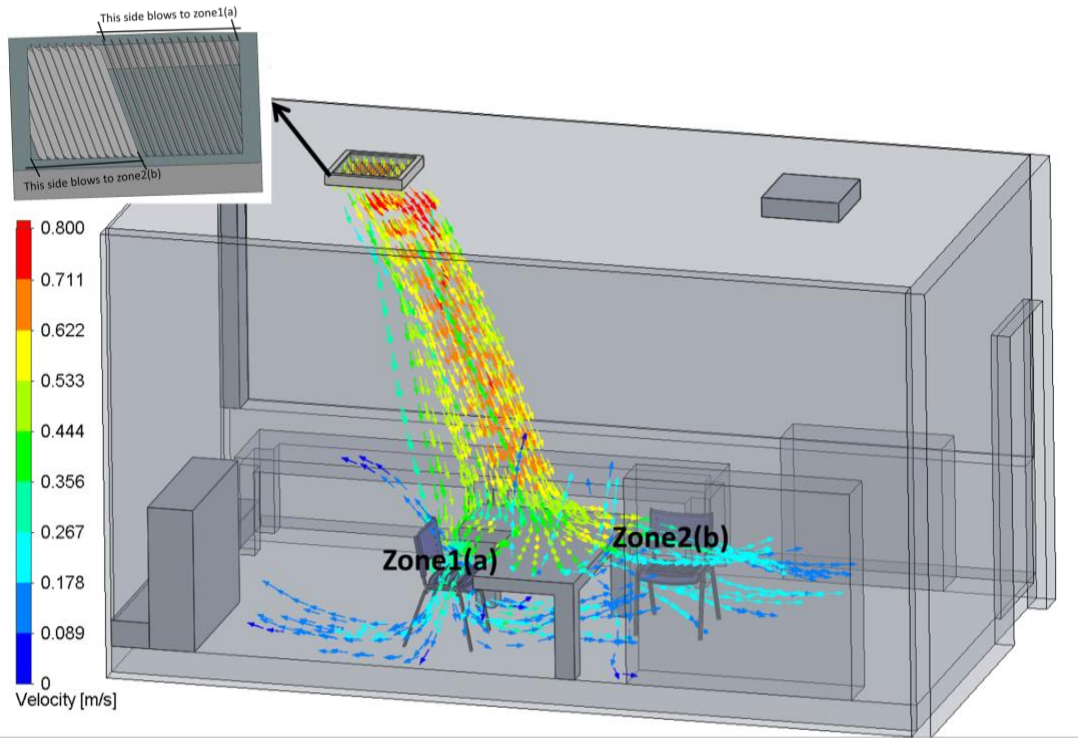


Figure 5.5 New diffuser type and air flow distribution. The visualization of flow path's length is constrained up to 5 m in figure. The angle of blades of diffuser gives advantages to blow the air directly to occupant's zone.

5.4. Comparison of the scenarios in Comfort Zone 1

The average values of air velocity, air temperature, MRT, OT, Fanger Comfort Parameters PMV and PPD are calculated for four different scenarios of comfort Zone 1. Results are shown comparatively in the graphs showed below, respectively. The aim of these comparisons is to understand the effect of different glass properties and different air distribution on TC.

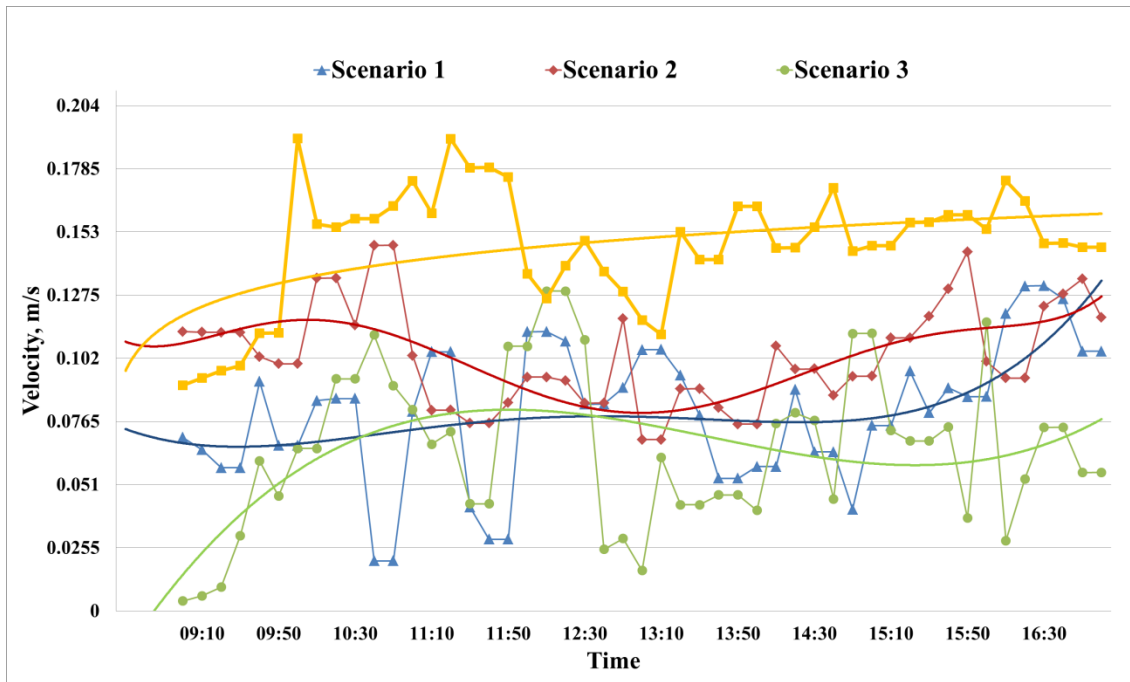


Figure 5.6 Results of four different scenarios with average velocity fluctuation in comfort Zone 1 from 09:00 to 17:00. Velocity value of first three scenarios' are close to each other, but intensity of new designed diffuser is higher. Flow freezing option generates the flow data in every 30 minutes, so curve fit is shown with data.

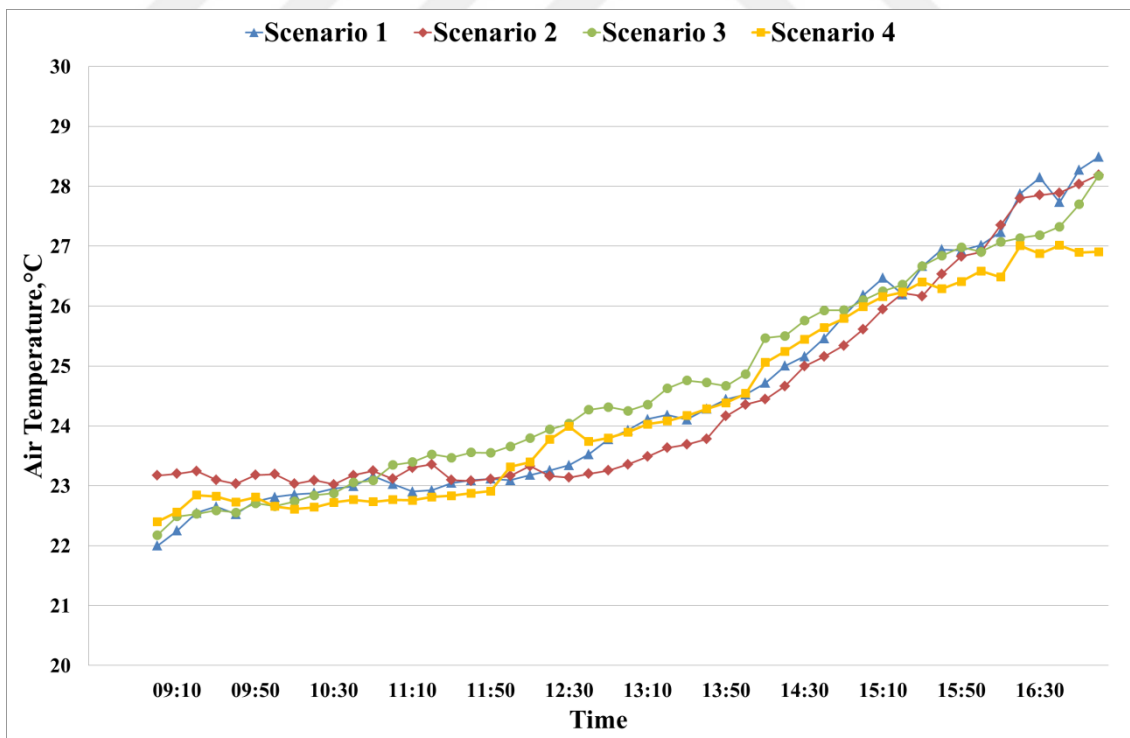


Figure 5.7 Results of four different scenarios with average air temperature in comfort Zone 1 from 09:00 to 17:00.

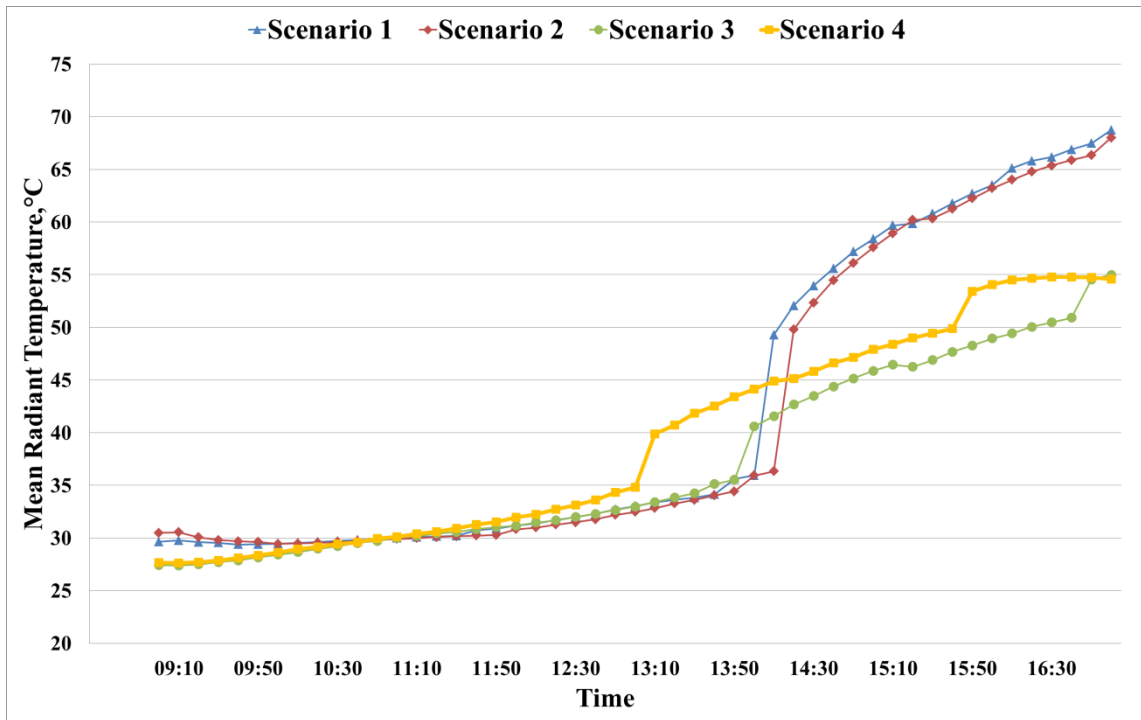


Figure 5.8 Results of four different scenarios with average mean radiant temperature in comfort Zone 1 from 09:00 to 17:00. Glass type and diffuser conditions for scenario 3 and 4 generate similar results for mean radiant temperature, but this value is much higher than others.

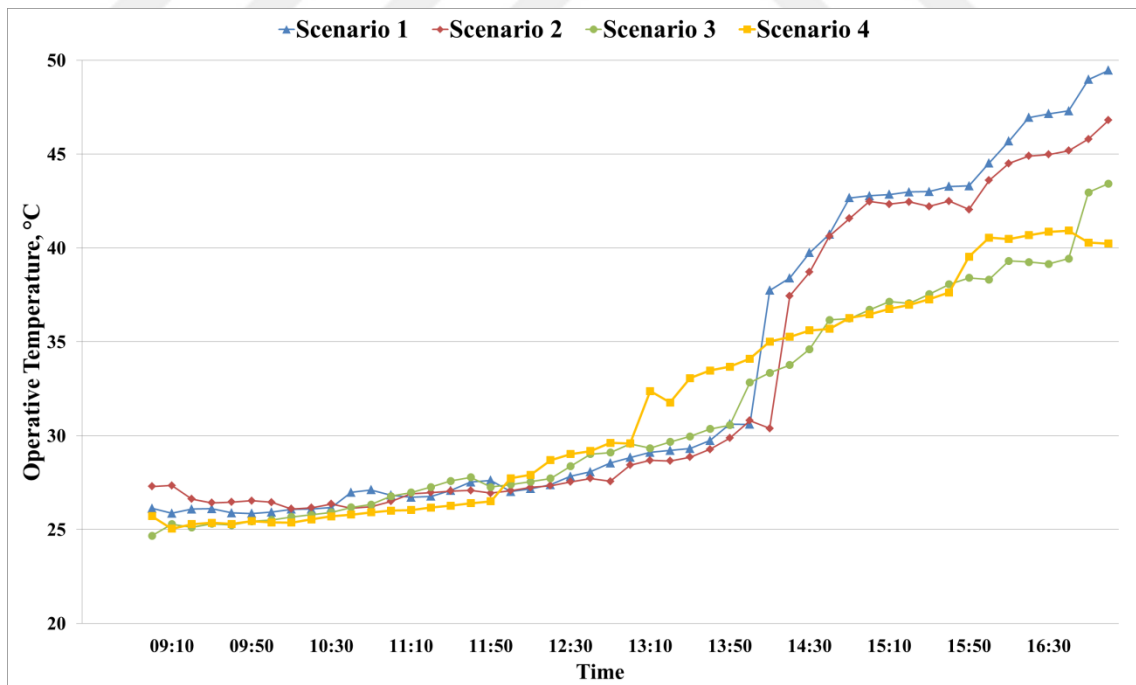


Figure 5.9 Results of four different scenarios with average operative temperature in comfort Zone 1 from 09:00 to 17:00. Operative temperatures have a linear relationship with mean radiant temperature in the scenario 1 and 2.

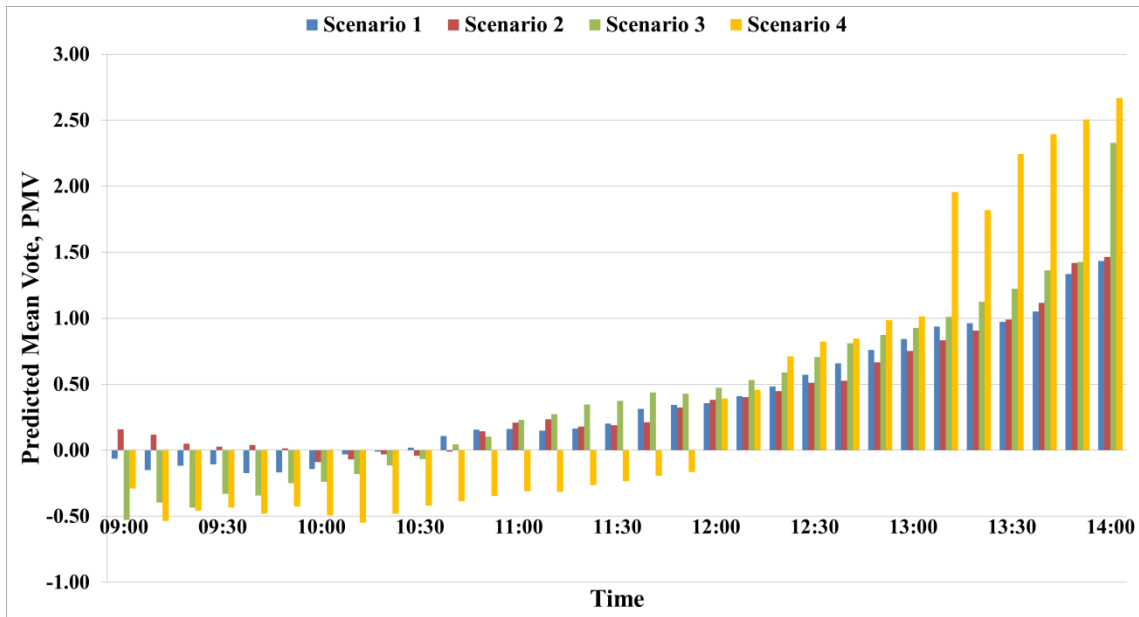


Figure 5.10 Results of four different scenarios with average predicted mean vote in comfort Zone 1 from 09:00 to 14:00. PMV values help to understand sensation range between determined scenarios. Feeling hot in comfort Zone 1 after 14.00 to 17.00 shows that PMV values don't correspond to any meaningful range on TC for Fanger Method.

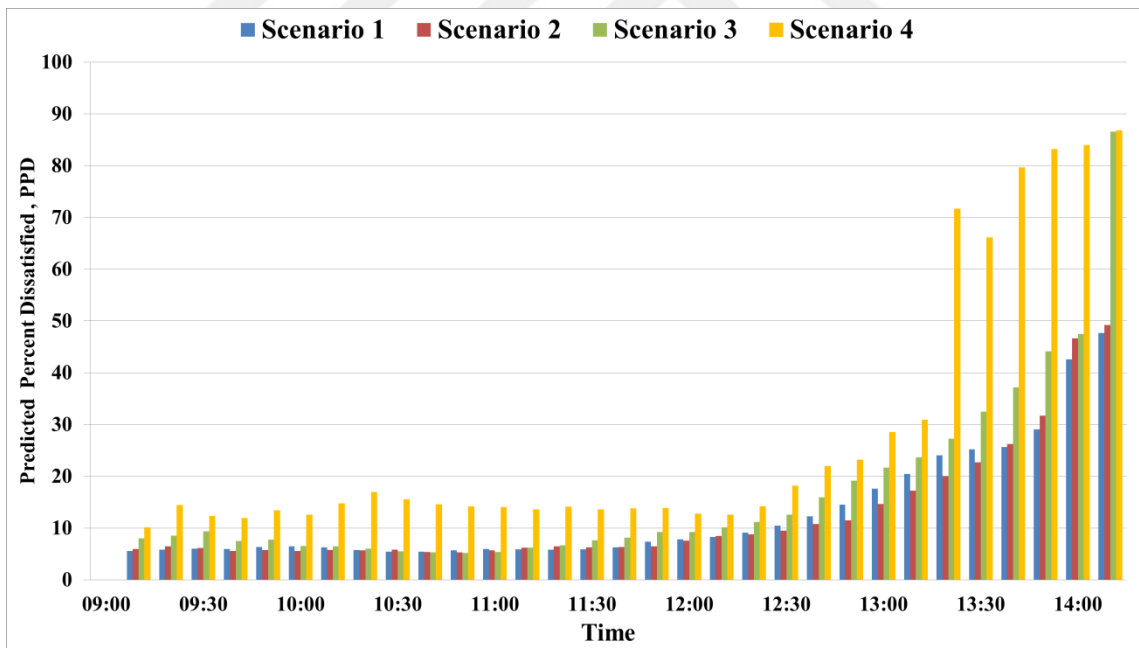


Figure 5.11 Results of four different scenarios with Predicted Percent Dissatisfied in comfort Zone 1 from 09:00 to 14:00. Predicted Percent Dissatisfied show that in comfort Zone 1, 100% of people are not satisfied after 14.00 in all scenarios.

5.5. Comparison of the scenarios in Comfort Zone 2

The average values of air velocity, air temperature, MRT, OT, Fanger Comfort Parameters PMV and PPD are calculated for four different scenarios of comfort Zone 2. Results are shown comparatively in the graphs showed below, respectively. The aim of these comparisons is to understand the effect of different glass properties and different air distribution on TC.

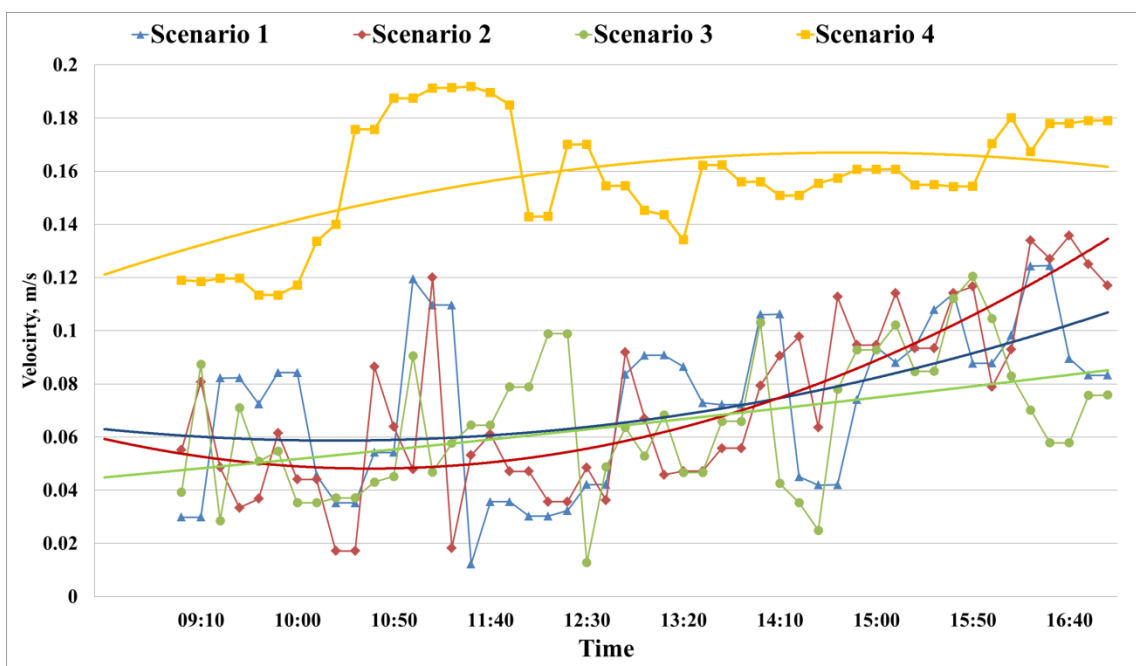


Figure 5.12 Results of four different scenarios with average velocity values in volume of comfort Zone 2 from 09:00 to 17:00. Intensity of velocity in all scenarios are closer to each other. Flow freezing option generates the flow data in every 30 minutes, so curve fit is shown with data. Zone 2 is able to take advantage of speed of air intensity reasonably more than comfort Zone 1.

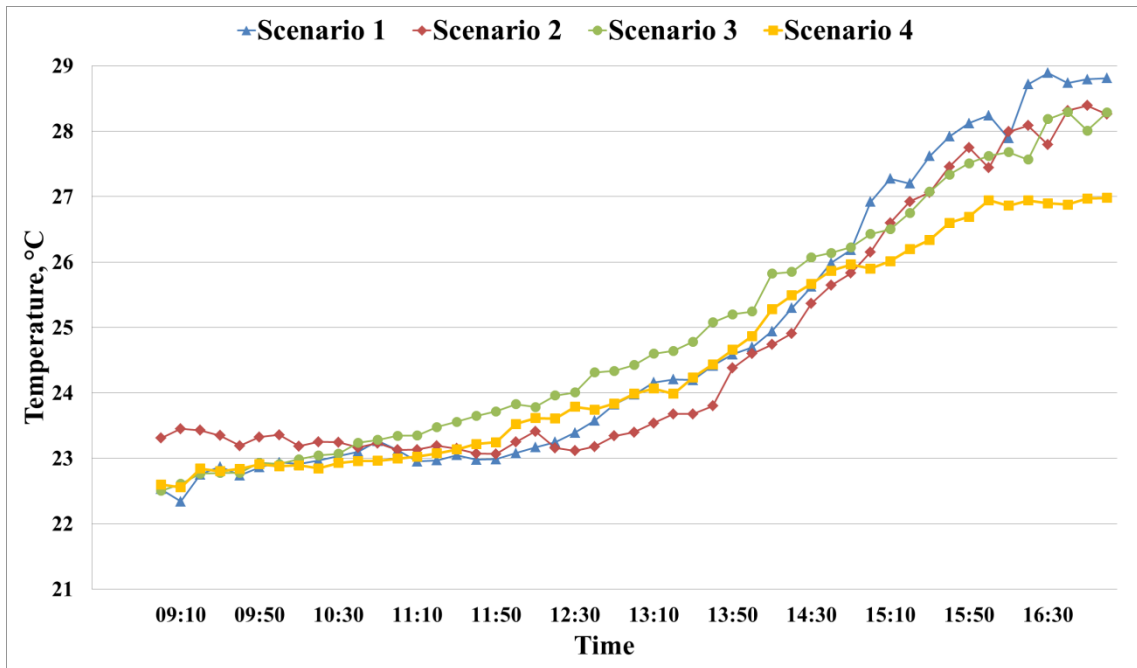


Figure 5.13 Results of four different scenarios with average air temperature in comfort Zone 2 from 09:00 to 17:00. Comparison of scenarios show that results of air temperature is similar in comfort zones with different scenarios.

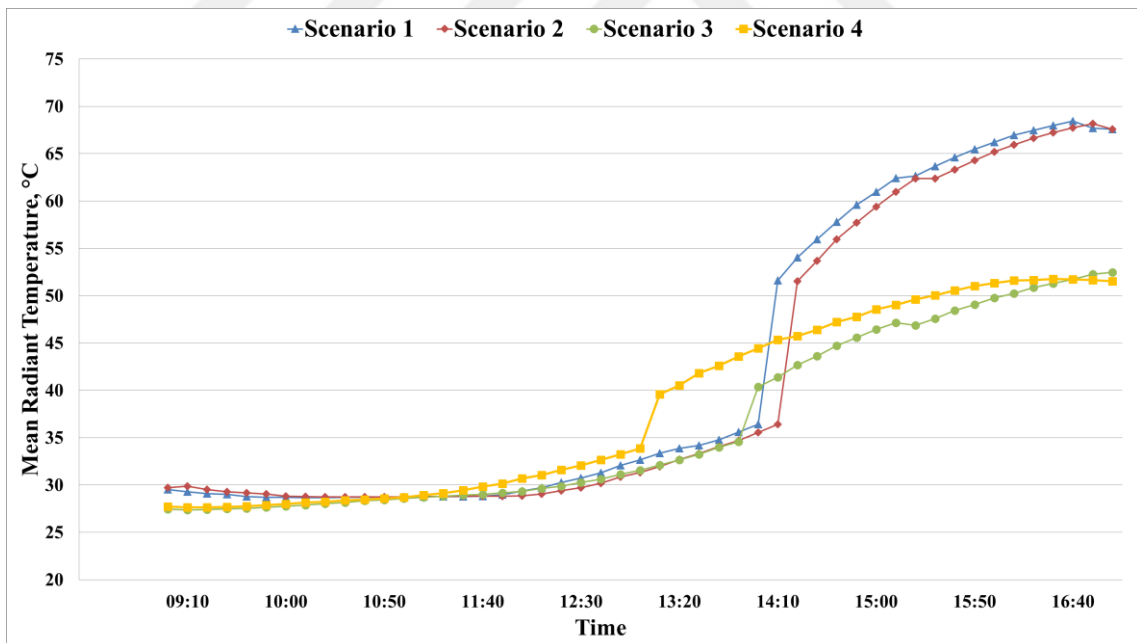


Figure 5.14 Results of four different scenarios with average mean radiant temperature in comfort Zone 2 from 09:00 to 17:00. Glass type and diffuser conditions for scenario 3 and 4 generate similar results for mean radiant temperature, but these values are much higher than other scenarios.

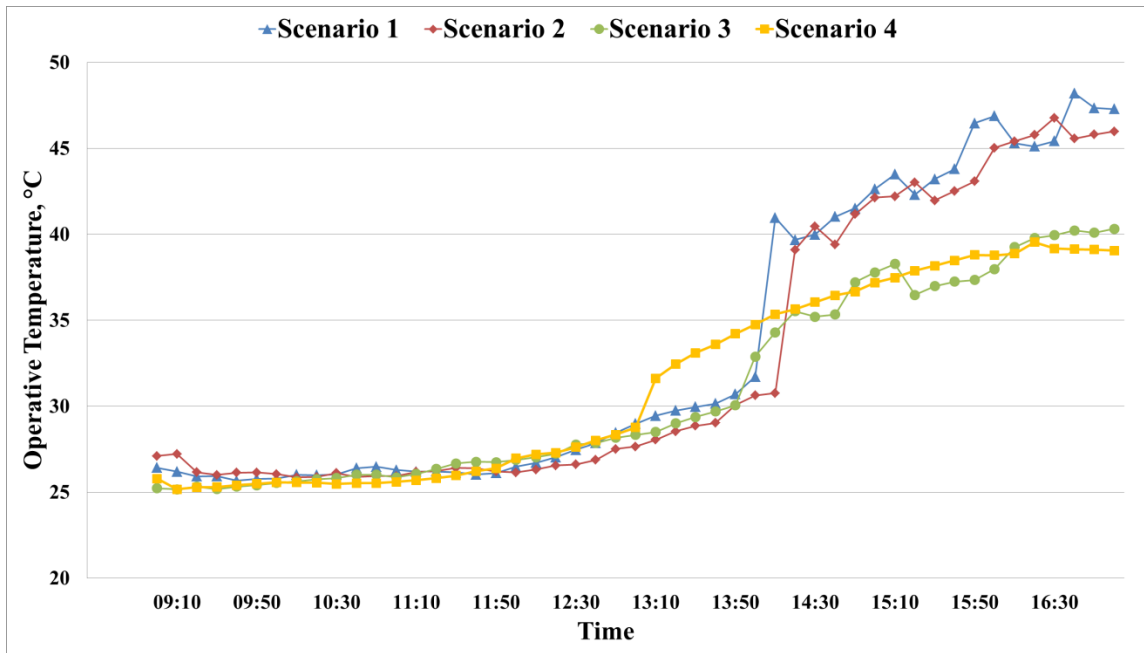


Figure 5.15 Results of four different scenarios with average operative temperature in comfort Zone 2 from 09:00 to 17:00. Operative temperature is lower than comfort Zone 1, especially for the scenarios 3 and 4.

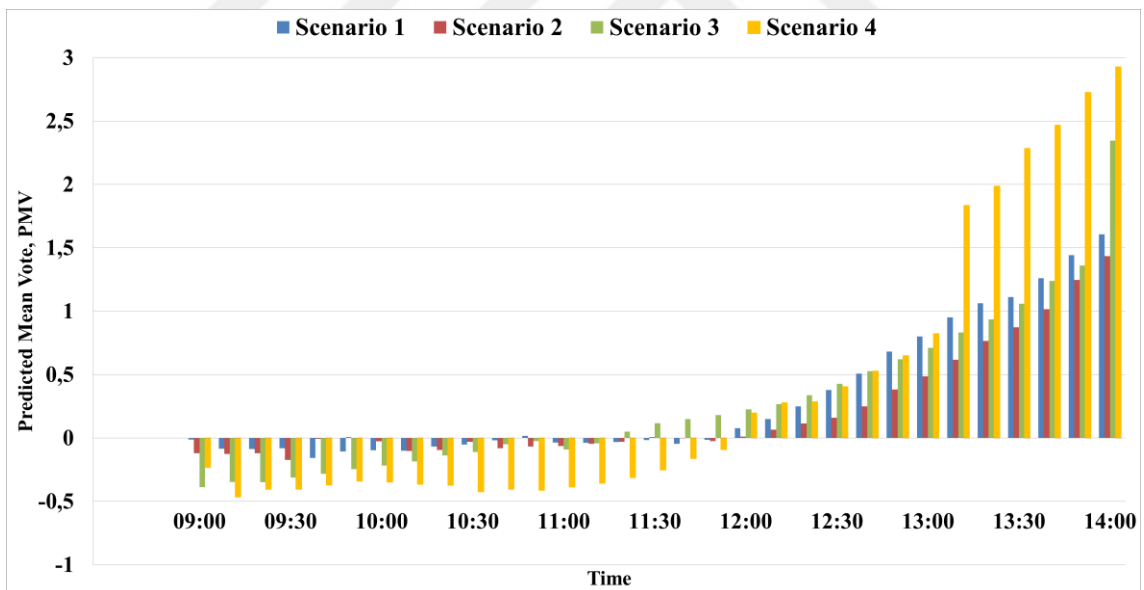


Figure 5.16 Results of four different scenarios with average predicted mean vote in comfort Zone 1 from 09:00 to 14:00. Predicted mean vote results are higher than the limit of Fanger comfort range after 14.00 in all scenarios.

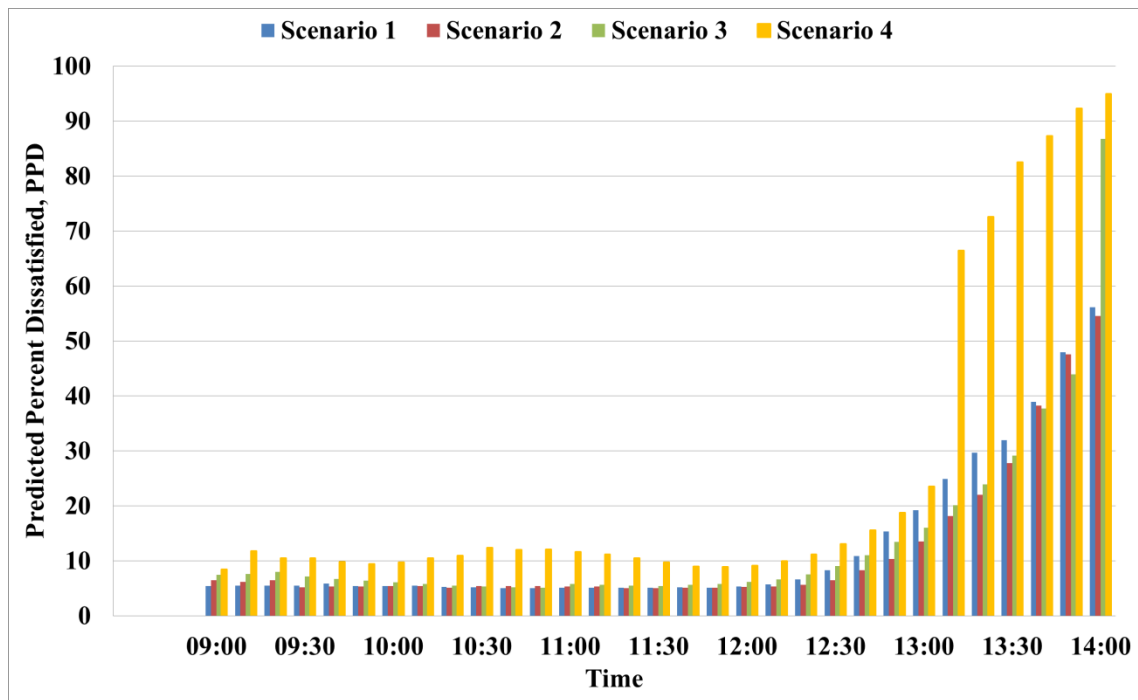


Figure 5.17 Results of four different scenarios with Predicted Percentage of Dissatisfied in comfort Zone 2 from 09:00 to 14:00. Higher PMV results generate higher dissatisfied sensation in comfort Zone 2 as Zone 1.

5.6. Discussions of Comparison Results

Based on the results obtained from the studied four scenarios, in terms of TC, the comfort zones are very hot on the day of July 21st, especially after 02:00 pm. According to the P.O. Fanger scale, level 3 thermal sensation ranges is used for hot situations, but any values above 3 are not defined.

Figure 5.10 and Figure 5.16 show that Glass 1 to Glass 3, TC increases in three scenarios. Decreasing transmissivity from Glass 3 to Glass 1 changes the direct and diffuse solar radiation and intensity of MRT in the room. Particularly, 50% of solar energy passes to room with the visible wavelength (380 nm – 700 nm). Therefore, transmissivity of glasses multiplication with solar heat flux value at visible range shows the importance of this calculation for TC. Glass 1 has highly transmissivity after the 700 nm wavelength but the MRT, also OP and PMV results are not much higher than

scenario of Glass 2 in the room. The solar radiation fluctuates and decreases after 700 nm on the earth. It can be observed in Figure 5.18 with the transmissivity of glasses. Despite 3 different glass attempts, the thermal comfort level is not preserved after 14.30. Glass 3 has the lowest transmissivity in the visible range and after. But, it is not adequate for TC and it will not be preferred. Because it will have a negative effect on visual comfort.

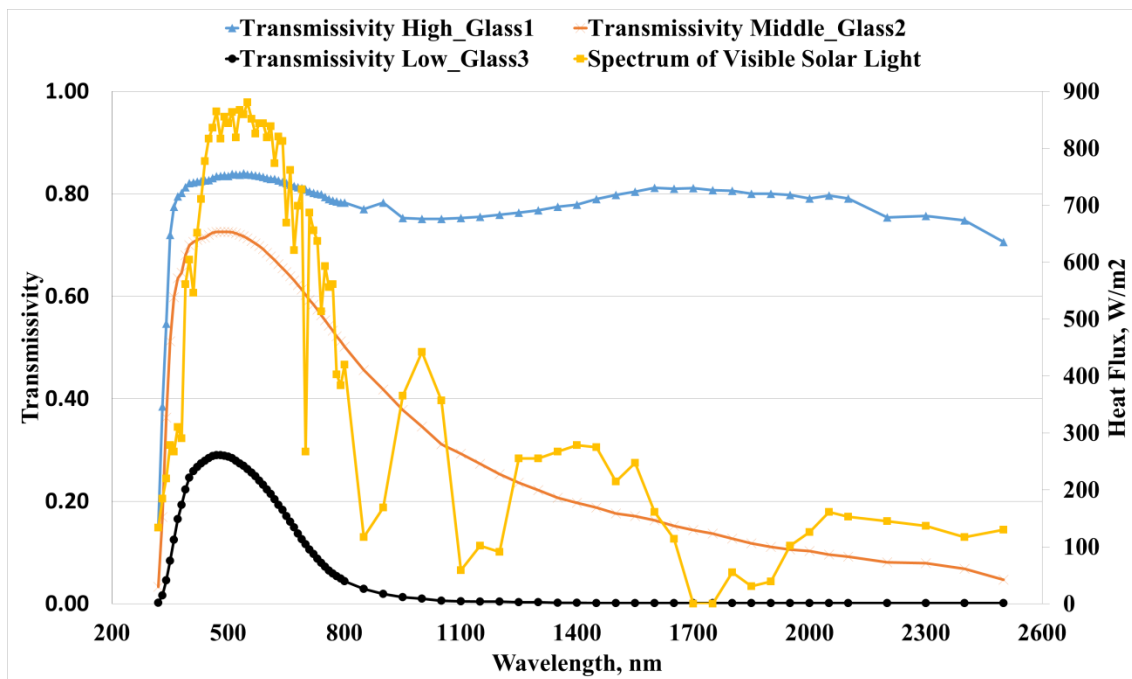


Figure 5.18 Spectral transmissivity of glass materials on the left axis and the spectrum of solar heat flux on the right axis.

Despite our efforts to increase the TC by changing the diffuser's angle of blades to direct the air flow into the whereabouts of the occupants of the room, it was observed that since MRT was too high, TC could not reach the expected desired level as depicted in Figures 5.10 and Figure 5.16. In fact, thanks to the increase in air speed, there is a local gain, but the MRT values are still very high.

In the first three scenarios, the diffusers blow cold air directly to the windows' glasses, allowing them to heat up more slowly, so that the MRT does not rise as much

as in scenario four, as shown in Figure 5.19. This is due to that fact that MRT is calculated according to main two intensities, $I_{diffuse}$ and $I_{sun} \cdot I_{sun}$ changes only with time in all scenarios and has the constant heat flux at each hour. However, $I_{diffuse}$ is high, especially after the 02:00 pm as presented in Figure 5.20 and Figure 5.21. The diffuse intensity leaving the wall to the Zone 1 and Zone 2 comfort zones is high due to less cooling of the wall and the windows (due to new diffuser's air flow direction in scenario four).

When the indoor air temperature is 22 °C or above, thermal discomfort increases due to exposure to direct solar radiation. In the summer season, TC is mostly unrelated with U-value but is closely correlated with solar radiation transmissivity. Lyons et al. (1999) also pointed out that using the low-E glasses (53% transmissivity) instead of normal clear glass (83% transmissivity) with the same thickness (3mm) can reduce the thermal discomfort to more than half [71]. In this thesis, we show that spectral distribution of glasses is very important for understanding thermal comfort should be considered in detail. Otherwise, the spectral distribution of solar intensity and the transmissivity of the glasses in visible range, decreasing the transmissivity cannot be an effective way to increase the TC.

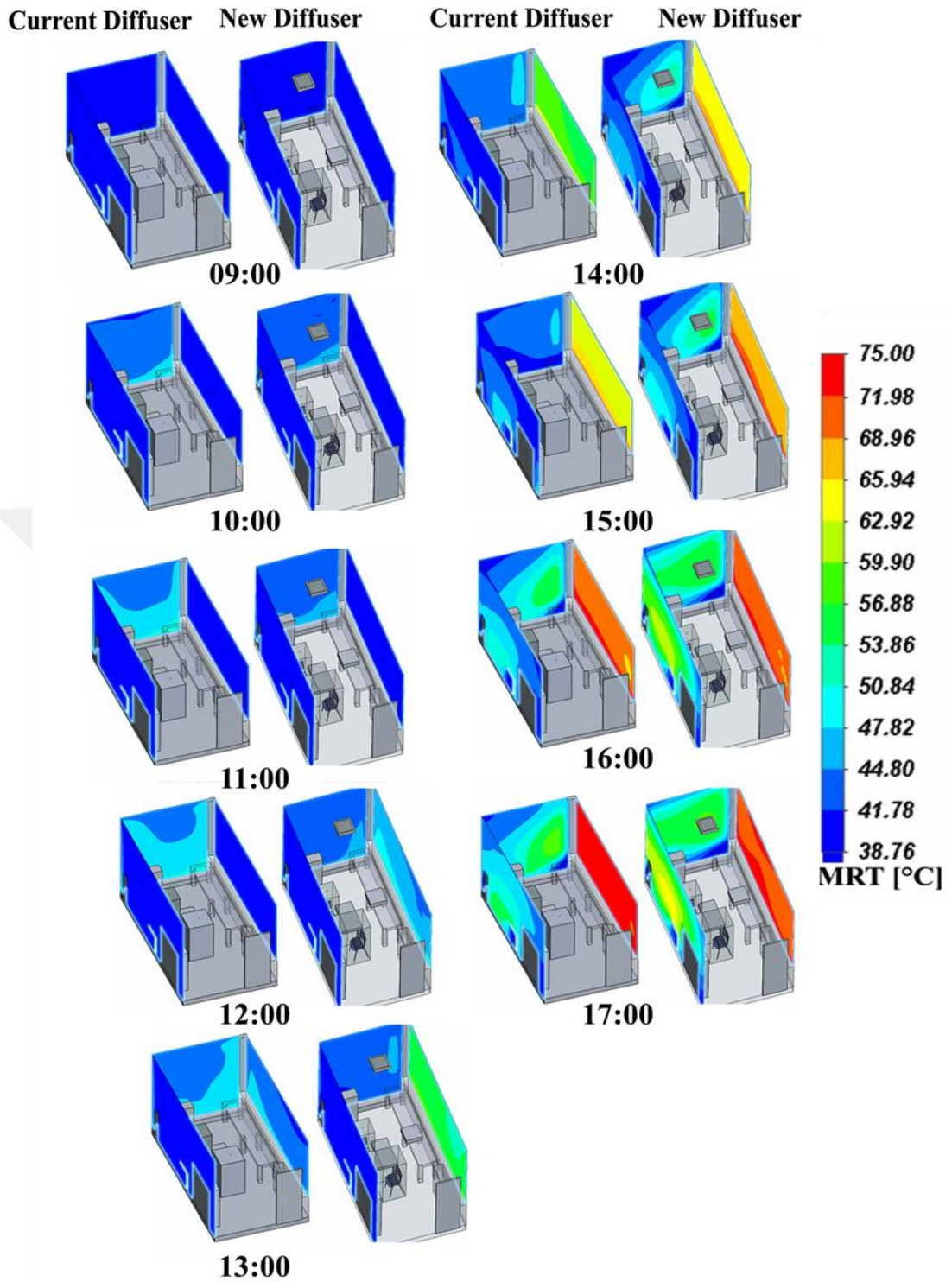


Figure 5.18 Variation of the average mean radiant temperature on the wall and glass surface from 09:00 to 17:00 in demonstration room.

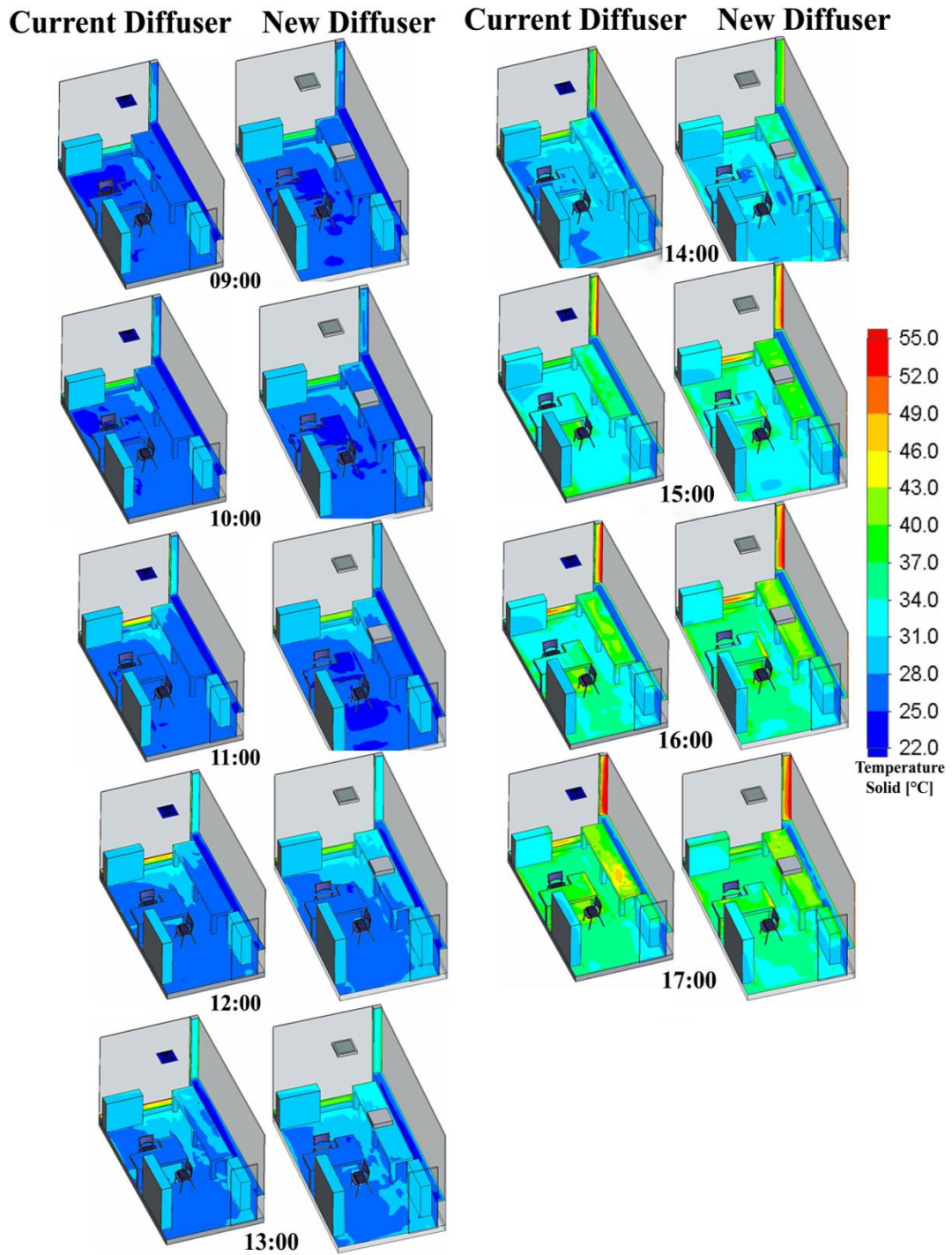


Figure 5.19 Variation of the temperature on the surface of solid material from 09:00 to 17:00. Comparison of the temperature differences results with the current diffuser and the designed new diffuser.

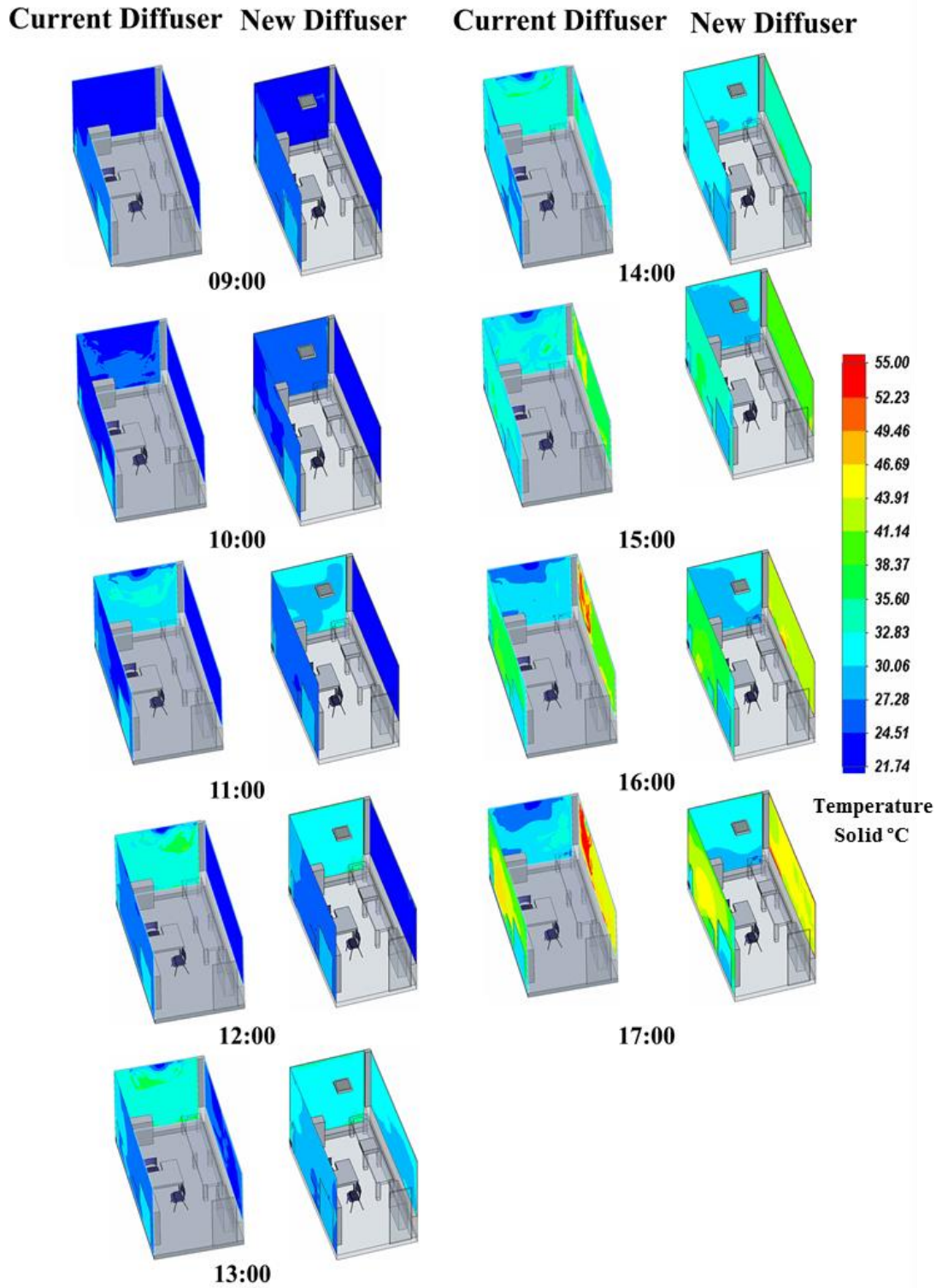


Figure 5.20 Temperature on the inside wall and glass surfaces from 09:00 to 17:00. New design diffuser effects on these surfaces from the perspective of temperature.

CHAPTER VI

CONCLUDING REMARKS

6.1 Conclusion

The extension of all these earlier studies constituted the present thesis. This thesis is focused on understanding the TC with CFD method in a room.

In Chapter I, general background of indoor environmental qualities with perspective of different comfort assumptions were estimated. The methodology of determining the TC in an environment before the construction phase of building was defined. The literature review, investigated the approaches to examine TC with the numerical solutions. We defined the four different factors which define the best living condition as Thermal Comfort (TC), Indoor Air Quality (IAQ), Visual Comfort (VC) and Acoustic Comfort (AC), which are essential in maintaining the health and productivity of people who live in crowded cities. We explained that these factors are not discussed in the design and construction phase of most buildings. In addition, their impact on energy efficient operation of buildings is hardly considered at all. Furthermore, we discussed that we focus only on TC.

In Chapter II, first the mathematical formulations are provided and the physics of the problem considered in thesis is explained. The equations of fluid flow (Navier-Stokes) and conservation of energy are considered next. Specialized turbulence model (k-epsilon) formulations are given in section 2.2.1 which covers both the equations considered by the FloEFD software and also the physics of fluid mechanics. Radiation heat transfer modelling for simulations, solar load model and environment temperature, discrete transfer model, discrete ordinates model, absorption and transmission,

reflection and radiation spectrum is discussed in details and Fanger's method's formulations for TC are given.

In Chapter III, the model considered in this thesis, which is an office room in Özyeğin University, dimensions of the room and the material properties of the furniture, walls and windows are provided in details. We explained that the most important factor in choosing this office for TC analysis was that about 66% of the facades facing south and west, have windows in this office. The two dimensional room drawings were provided by the architectural design office of Özyeğin University and prior to the CFD analysis, the three dimensional model of the study room was prepared using Solidworks software. The working principle of the HVAC systems and its schematic drawings of the diffusers were obtained from the mechanical installation design office.

In Chapter IV, first, CFD method and its step by step developmental procedures are provided. Next, these steps are applied to our scenarios. The numerical validation scenario is tackled in this chapter and its comparison with experimental tests is given. The error rate calculations were performed to investigate the correlation between numerical results and experimental studies. In comparing the velocity values in the seating area for simulations and experiments, the average error order was calculated to be 14%. When the same comparison was completed for the diffuser height measurements, the average error rate was calculated as 5%. The temperature values obtained on the surface of the glass after the simulation were also compared with the results measured by thermocouple on the inner glass surface on the south façade. The average error order is below 1% when compared to the experimental measurements and numerical analysis of the temperature of the glass surface.

In Chapter V, we provide a detailed transient analysis for comparison of TC scenarios in the demonstration room. Furthermore, all comparison results for the TC are given in determined comfort zones. The analyses were performed on 21st of July. The main reason for choosing this summer day is that due to the feedback obtained from the user of the room, the level of thermal discomfort on this day is very high, due to received intense solar radiation. During this period, all outdoor climate and indoor boundary conditions are considered fixed and the only varying factor is the change of the angle of the sun, which changes the intensity of the solar heat flux. In the following sections, we compare four different scenarios in three of which, three different glass materials (Glass 1, Glass 2, and Glass 3) are used. The difference of the glasses comes from their level of the transmissivity. It is realized that the Glass 1 material has the highest level of transmissivity. Glass 2 material has the middle level of transmissivity and Glass 3 has the lowest level of transmissivity. Among these materials, we chose Glass 2 for the benchmark scenario. The comfort level was investigated by trying to improve the TC in the entire room, instead of only focusing on the areas where the user is usually present at. In order to achieve this goal, a new diffuser has been designed to replace the existing diffuser, and the air has been directed towards the users' whereabouts. In the fourth scenario, Glass 3 material is used together with the new diffuser design. Finally, the comparison of the results was shown by investigating the PMV and PPD.

As a result of this completed study, I) air distribution, II) air temperature, III) average radiation temperature and IV) humidity profiles, which are the basic parameters affecting thermal comfort for the designated room, are numerically calculated. The consistency of numerical solutions, which are also supported by the measurement

results, is examined. The visualization of these four parameters are done by evaluation of the change of the material properties inside the room or the HVAC system. Subsequently, these values were interpreted as PMV and PPD for thermal comfort, depending on human clothing and metabolic rate. The outcome of this thesis can be used in highly façade cladding places for thermal comfort.

6.2. *Future Works*

In order to improve these numerical studies, to be able to use it in a room, environmental studies in the presence of the occupants and its thermoregulation affects should be carried out. From the literature, we know that P.O. Fanger PMV and PPD indices overestimate the TC values, when calculated without consideration of thermoregulation method. In a future extension of this work, they shall be investigated together. CFD method can generate the heat transfer coefficient by flow distribution and other three environmental parameters. After that, results of numerical thermoregulation calculations can be implemented.

BIBLIOGRAPHY

- [1] EC, “Greenhouse gas emission statistics.,” 2015
<http://ec.europa.eu/eurostat/statisticsexplained/index.php/Greenhousegasemissionstatistics>
- [2] L. Pe, “A Review on Buildings Energy Consumption Information ’,” vol. 40, pg. 394–398, 2008.
- [3] Y. Somuncu, M. P. Mengüç, The “Energy-Efficiency-Core” Concept for a New Building, PLEA 2015-31th International PLEA Conference Architecture in Revolution, Bologna, Italy,9-11 September 2015
- [4] J. L. M. Hensen, “On The Thermal Interaction of Building Structure And Heating And Ventilating System.”, 1991.
- [5] CEN (2005). European Committee for Standardization. EN ISO 7730:2005, “Ergonomics of the thermal environment - Analytical determination and interpretation of thermal comfort using calculation of the PMV (predicted mean vote) and PPD (predicted percent of dissatisfied) indices and local thermal comfort,” 2006.
- [6] Ashrae, “Chapter 13: Indoor Environmental Modeling,” 2009 ASHRAE Handbook—Fundamentals, 2009.
- [7] J. Lefevre, “Lefevre: Chaleur animale et bioénergétique - Google Academic,” Book, 1911. [Online]. [https://scholar.google.com/scholar_lookup?title=Chaleur animale et bioénergétique&author=J Lefèvre&publication_year=1911](https://scholar.google.com/scholar_lookup?title=Chaleur+animale+et+bioénergétique&author=J+Lefèvre&publication_year=1911).
- [8] A. C. Burton, “The Application of the Theory of Heat Flow to the Study of Energy Metabolism,” *J. Nutr*, vol. 7, pp. 497–533, 1934.
- [9] R. J. Crosbie, J. D. Hardy, and E. Fessenden, “Electrical Analog Simulation of Temperature Regulation in Man,” *Bio-Medical Electron. IRE Trans.*, vol. 8, no. 4, pp. 245–252, 1961.
- [10] J. a. Stolwijk, “A Mathematical Model of Physiological Temperature Regulation in Man,” August, pg. 83, 1971.
- [11] E. A. Arens and H. Zhang, “The Skin’s Role in Human Thermoregulation and Comfort Book,” *ASHRAE Trans.*, vol. 104, no. Pt 1B, pp. 1153–1171, 1998.
- [12] G. Fu and B. W. Jones, “Combined Finite Element Human Thermal Model and Finite Difference Clothing Model,” *Enviromental Ergon.*, pp. 166–169, 1996.
- [13] D. Fiala, K. J. Lomas, and M. Stohrer, “A Computer Model of Human Thermoregulation for A Wide Range of Environmental Conditions: The Passive System” *J. Appl. Physiol.*, vol. 87, no. 5, pp. 1957–1972, 1999.

- [14] C. Huizenga, Z. Hui, and E. Arens, "A Model of Human Physiology and Comfort for Assessing Complex Thermal Environments," *Build. Environ.*, vol. 36, no. 6, pp. 691–699, 2001.
- [15] D. South African Institution of Civil Engineers. and F. A. Engelbrecht, *Journal of the South African Institution of Civil Engineers = Joernaal van die Suid-Afrikaanse Instituut van Siviele Ingenieurs.*, vol. 47, no. 2. The Institution, 1993.
- [16] H. Chappells and E. Shove, "Comfort paradigms and practices," 2004. [Online]. <http://www.lancaster.ac.uk/fass/projects/futcom/documents/webpaper.htm>.
- [17] A. C. Ogbonna and D. J. Harris, "Thermal comfort in sub-Saharan Africa: Field Study Report in Jos-Nigeria," *Appl. Energy*, vol. 85, no. 1, pp. 1–11, 2008.
- [18] A. Wagner, E. Gossauer, C. Moosmann, T. Gropp, and R. Leonhart, "Thermal Comfort and Workplace Occupant Satisfaction-Results of Field Studies in German Low Energy Office Buildings," *Energy Build.*, vol. 39, no. 7, pp. 758–769, 2007.
- [19] A. Pasupathy, R. Velraj, and R. V. Seeniraj, "Phase Change Material-Based Building Architecture for Thermal Management in Residential and Commercial establishments," *Renew. Sustain. Energy Rev.*, vol. 12, no. 1, pp. 39–64, 2008.
- [20] M. A. Ealiwa, A. H. Taki, A. T. Howarth, and M. R. Seden, "Investigation into Thermal Comfort in the Summer Season of Ghadames, Libya," *Build. Environ.*, vol. 36, no. 2, pp. 231–237, 2001.
- [21] K. W. H. Mui and W. T. D. Chan, "Adaptive comfort temperature model of air-conditioned building in Hong Kong," *Build. Environ.*, vol. 38, no. 6, pp. 837–852, 2003.
- [22] B. W. Zingano, "Discussion on Thermal Comfort With Reference to Bath Water Temperature To Deduce A Midpoint of The Thermal Comfort Temperature Zone" *Renew. energy*, vol. 23, no. 1, pp. 41–47, 2001.
- [23] N. Djongyang, R. Tchinda, and D. Njomo, "Thermal Comfort: A Review Paper," *Renew. Sustain. Energy Rev.*, vol. 14, no. 9, pp. 2626–2640, 2010.
- [24] G. S. Brager, "Thermal Adaptation in The Built Environment: A Literature Review," *Energy Build.*, vol. 27, no. 1, pp. 83–96, 1998.
- [25] M. A. Humphreys and J. Fergus Nicol, "The Validity of ISO-PMV for Predicting Comfort Votes in Every-day Thermal Environments," *Energy Build.*, vol. 34, no. 6, pp. 667–684, 2002.

- [26] T. Kim, S. Kato, and S. Murakami, "Indoor Cooling / Heating Load Analysis Based on Coupled Simulation of Convection , Radiation and HVAC Control," *Build. Environ.*, vol. 36, pp. 901–908, 2001.
- [27] H. Koskela and J. Heikkinen, "Calculation of Thermal Comfort From Cfd-Simulation Results," vol. 62, no. 1, pp. 712–717, 2002.
- [28] C. Van Treeck, P. Wenisch, M. Pfaffinger, M. Egger, O. Wenisch, and E. Rank, "Towards Interactive Indoor Thermal Comfort," pp. 1–15, 2006.
- [29] I. Atmaca and A. Yigit, "Predicting the Effect of Relative Humidity on Skin Temperature and Skin Wettedness," *J. Therm. Biol.*, vol. 31, no. 5, pp. 442–452, 2006.
- [30] R. C. Resources, "F09 SI: Thermal Comfort," *ASHRAE Handb. Fundam.*, p. 9.1-9.30, 2009.
- [31] D. Lampe and E. Bjerg, "Verification of CFD-based Computation of Thermal Comfort Indices," *Easc.Ansys.Com*, pp. 1–16, 2007.
- [32] P. D. McQuiston FC, "No," in *Heating, Ventilating, and Air Conditioning Analysis and Design*, 4th ed, 1994, pp. 100–36.
- [33] C. YA., *Heat Transfer A Practical Approach*. New York: McGraw- Hill, 1998.
- [34] *ASHRAE: Fundamentals, Load Calculation Data and Procedures*. 1993.
- [35] I. Atmaca, O. Kaynakli, and A. Yigit, "Effects of Radiant Temperature on Thermal Comfort," *Build. Environ.*, vol. 42, no. 9, pp. 3210–3220, 2007.
- [36] T. Catalina, J. Virgone, and F. Kuznik, "Evaluation of Thermal Comfort Using Combined CFD and Experimentation Study in a Test Room Equipped with A Cooling Ceiling," *Build. Environ.*, vol. 44, no. 8, pp. 1740–1750, 2009.
- [37] T. Wu, A. D. Clark, G. L. Mitchell, C. Lin, and H. Raymond, "Application of CFD Predictions to Quantify Thermal Comfort for Indoor Environments," pp. 347–354, 2012.
- [38] T. Nadu, "Development of Modified Thermal Comfort Equation for a Room With Window Openings At Adjacent Walls," no. 6, pp. 1670–1677, 2012.
- [39] M. Webb, "Building Energy and Cfd Simulation To Verify Thermal Comfort in Under Floor Air Distribution (Ufad) Design," *Build. Simul.*, pp. 1885–1892, 2013.
- [40] V. Gooje, "Impact of Radiant Asymmetry of Thermal Comfort Comparison of Real Data with Simulated Data," *PLEA 2013 Sustain. Archit. a Renew. Futur.*, no. September, 2013.

- [41] I. Bonefacic, I. Wolf, and B. Frankovic, “Numerical Modelling of Thermal Comfort Conditions in An Indoor Space with Solar Radiation Sources,” *Strojniški Vestn. - J. Mech. Eng.*, vol. 61, no. 11, pp. 641–650, 2015.
- [42] Frank. M. White, *Fluid Mechanics Book*, 8th Edition, Boston, Mass: WCB/McGraw-Hill
- [43] H. Lomax, T. H. Pulliam, and D. W. Zingg, “Fundamentals of Computational Fluid Dynamics,” *Sci. Comput.*, p. 249p., 2001.
- [44] “Anderson J.D.- Computational Fluid Dynamics: The Basics with Applications” Berlin: Springer-Verlag, 1992.
- [45] F. Moukalled, L. Mangani, and M. Darwish, *The Finite Volume Method in Computational Fluid Dynamics - An Advanced Introduction with OpenFOAM and Matlab*, vol. M. 2016.
- [46] *An-Introduction-to-Computational-Fluid-Dynamics: The Finite Volume Approach- H.K. Versteeg.*
- [47] R. C. Resources, “Health Care Facilities,” 2007.
- [48] B. J. A. Clark and F. Ashrae, “Kitchen Ventilation Problems,” July, 2009.
- [49] F. J. Wang, M. J. Lee, C. M. Lai, and C. Y. Hsu, “Energy Efficient HVAC System by Reducing Air Change Rate for an Unoccupied Operating Room.”
- [50] Ashrae, “Chapter 03: Fluid Flow,” 2009 ASHRAE Handbook—Fundamentals, no. 1, 2009.
- [51] C. Methods, A. Mech, S. Guillas, N. Glover, and L. Malki-epshtein, “ScienceDirect Bayesian Calibration of The Constants of the $k - \epsilon$ Turbulence Model for a CFD Model of Street Canyon Flow,” *Computer Methods Applied Mech. Eng.*, vol. 279, pp. 536–553, 2014.
- [52] M. G. Corporation, “Technical Reference Software Version 16,” 2016.
- [53] H. JR, M. MP, and S. R., *Thermal Radiation Heat Transfer*, 6th ed. Boca Raton: Taylor and Francis, 2016.
- [54] USGS, “USGS Spectroscopy Lab - Clark and others, 2007 Spectral Library splib06a, <https://speclab.cr.usgs.gov/spectral.lib06/ds231/datatable.html>.
- [55] California Institute of Technology - Jet Propulsion Laboratory, “ASTER Spectral Library - Version 2.0 — Spectral Library.” <https://speclib.jpl.nasa.gov/>.
- [56] M. Heier, “Daylight and Thermal Comfort in a Residential Passive House,” 2012.

- [57] J. A. Palyvos, "A survey of Wind Convection Coefficient Correlations for Building Envelope Energy Systems' Modeling," *Appl. Therm. Eng.*, vol. 28, no. 8–9, pp. 801–808, 2008.
- [58] H. Bulut, "Generation of Typical Solar Radiation Data for Istanbul, Turkey," *Int. J. Energy Res.*, vol. 27, no. 9, pp. 847–855, 2003.
- [59] J. Pilhagen, "Master Thesis: A Literature Review of the Stainless Steel 21-6-9 and its Potential for Sandwich Nozzles," *Rev. Lit. Arts Am.*, 2007.
- [60] S. Sawaf, P. J. F. Barlow, and E. Essah, "Impact of Uncontrolled Ventilation on Food Supermarkets."
- [61] L. Rong, E. F. Pedersen, and G. Zhang, "Application of Hybrid Ventilation System in A Pig House – Study Of Winter Case Department of Engineering, Aarhus University Inge Lehmanns Gade 10 , 8000 Aarhus C , Denmark AgriFarm A / S Niels Pedersens Alle 2 , 8830 Tjele , Denmark," *Build. Simul. Conf.*, pp. 863–869, 2015.
- [62] Y. Zhang, J. Li, H. Sun, J. Liu, and Q. Chen, "Evaluation of Different Air Distribution Systems For Sleeping Spaces In Transport Vehicles," *Build. Environ.*, vol. 94, pp. 665–675, 2015.
- [63] S. Bolineni, S. Stratbücker, and C. van Treeck, "Development Of Reduced Order Flow Responsive Models Of Convective Heat Transfer For Human Body Segments," *Build. Simul.*, vol. 8, no. 4, pp. 393–404, 2015.
- [64] Y. Zhang, D. Novieto, and Y. Ji, "Human Environmental Heat Transfer Simulation With Cfd – The Advances and Challenges," *Elev. Int. IBPSA Conf.*, pp. 2162–2168, 2009.
- [65] S. C. Chapra and R. P. Canale, "Numerical Methods For Engineers," *Math. Comput. Simul.*, vol. 33, no. 3, p. 260, 2015.
- [66] G. Heidarinejad, M. Heidarinejad, and S. Delfani, "Outdoor Design Conditions Data For The Cities Of Iran," *6th Int. Energy Convers. Eng. Conf. IECEC*, pp. 1–12, 2008.
- [67] "Istanbul Weather Averages | Monthly Average High and Low Temperature World Weather, <https://www.worldweatheronline.com/istanbul-weather-averages/istanbul/tr.aspx>.
- [68] ASHRAE Standard 55P, "Thermal Environmental Conditions For Human Occupancy," vol. 2013, 2003.
- [69] DIN EN, "Ventilation for Residential Building - Performance Requirements for Ventilation and Room-Conditioning Systems," *Management*, p. 72, 2007.

- [70] L. J. Schoen and P. F. Alspach, “Thermal Environmental Conditions for Human Occupancy,” vol. 2013, pp. 1–7, 2013.
- [71] C. Huizenga, P. Mattelaer, E. Arens, and W. Hall, “Window Performance for Final Report To the National Fenestration Rating Council,” no. February, 2006.



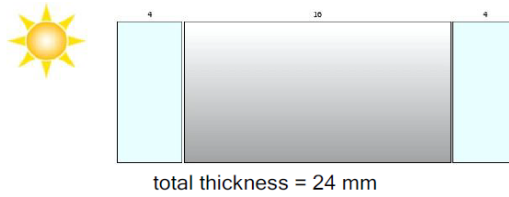
APPENDIX A

CONFIGURATOR SOFTWARE AND SOLAR PROPERTIES OF GLASSES

The physical properties of glass materials, used in the simulations were obtained by the software Guardian Configurator. This program has been developed by the technical team of Guardianguass Company. It provides us to generate the light and energy performance of any single glass or combination of glass types and thickness for double and triple glass units. After the choosing types of the glasses and put them in order, it gives the users a few papers about the glass performance in accordance with the norm of EN 410 and EN 673. The calculation methodology of software has been verified by KIWA which is an independent organization. They provide high-quality certification activities with review, assessment, research, technical knowledge and data services.

All of the physical properties of glasses, which used in this thesis listed below:

Details of Glass 1



Glazing from external to internal:

<p>Pane 1</p> <p>4 mm Float Glass ExtraClear Plus</p>		<p>Pane 2</p> <p>4 mm Float Glass ExtraClear Plus</p>
<p>Spacer 1 - 16 mm</p> <p>10% Air</p> <p>90% Argon</p>		

Results

Visible light (EN 410 - 2011)	Solar energy (EN 410 - 2011)
transmittance [%] $\tau_v = 83,5$	solar factor [%] $g = 81,6$
reflectance external [%] $\rho_v = 15,1$	shading coefficient [g/0.87] $sc = 0,94$
reflectance internal [%] $\rho_v = 15,1$	direct transmittance [%] $\tau_e = 79,3$
general colour rendering index [%] $R_a = 99,2$	direct reflectance external [%] $\rho_e = 14,2$
	direct reflectance internal [%] $\rho_e = 14,2$
Thermal properties (EN 673 - 2011)	direct absorption [%] $a = 6,5$
U-value [W/(m ² K)] $U_g = 2,6$	UV transmittance [%] $\tau_{uv} = 61,6$
slope $\alpha = 90^\circ$	secondary internal heat transfer factor [%] $q_i = 2,2$
	Other data
	estimated sound reduction index [dB] $R_w = \text{NPD}$
	(EN 717-1) $C = \text{NPD}$
	$C_{tr} = \text{NPD}$

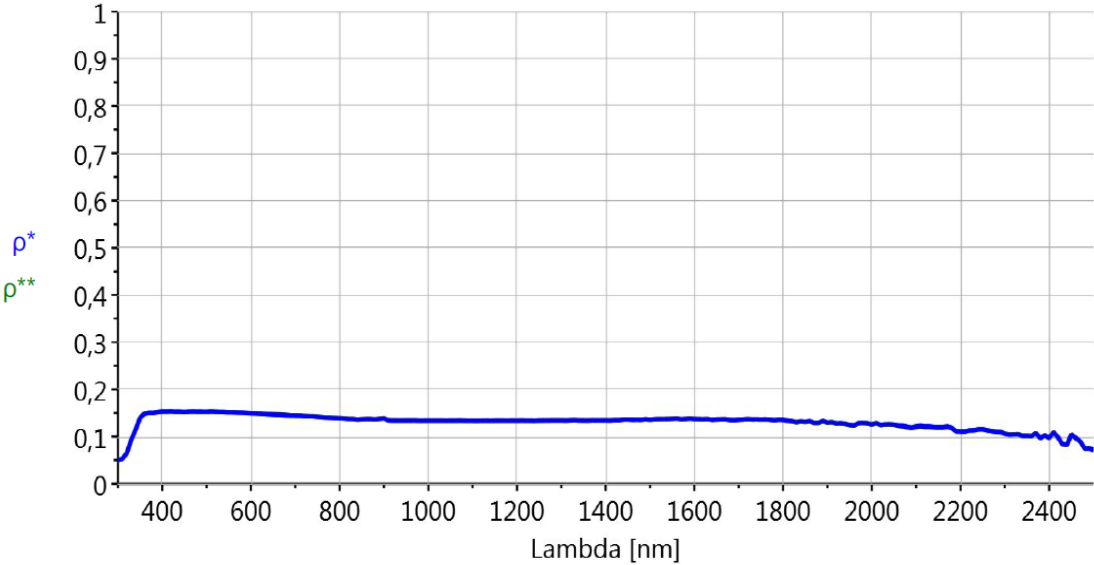
Glass 1 Spectral Values

λ [nm]	τ	ρ^*	ρ^{**}	λ [nm]	τ	ρ^*	ρ^{**}
300	0,001	0,052	0,052	710	0,805	0,144	0,144
310	0,024	0,053	0,053	720	0,802	0,143	0,143
320	0,150	0,065	0,065	730	0,800	0,143	0,143
330	0,385	0,093	0,093	740	0,799	0,143	0,143
340	0,547	0,115	0,115	750	0,794	0,142	0,142
350	0,720	0,140	0,140	760	0,790	0,141	0,141
360	0,775	0,149	0,149	770	0,787	0,140	0,140
370	0,795	0,151	0,151	780	0,785	0,140	0,140
380	0,802	0,151	0,151	790	0,783	0,139	0,139
390	0,813	0,152	0,152	800	0,783	0,139	0,139
400	0,821	0,153	0,153	850	0,770	0,137	0,137
410	0,822	0,153	0,153	900	0,783	0,139	0,139
420	0,824	0,153	0,153	950	0,753	0,134	0,134
430	0,825	0,153	0,153	1000	0,751	0,134	0,134
440	0,826	0,153	0,153	1050	0,751	0,134	0,134
450	0,827	0,152	0,152	1100	0,753	0,133	0,133
460	0,831	0,153	0,153	1150	0,755	0,134	0,134
470	0,834	0,153	0,153	1200	0,759	0,134	0,134
480	0,835	0,153	0,153	1250	0,763	0,134	0,134
490	0,836	0,153	0,153	1300	0,768	0,135	0,135
500	0,835	0,153	0,153	1350	0,775	0,134	0,134
510	0,839	0,153	0,153	1400	0,779	0,135	0,135
520	0,838	0,153	0,153	1450	0,790	0,137	0,137
530	0,837	0,152	0,152	1500	0,798	0,136	0,136
540	0,840	0,152	0,152	1550	0,804	0,138	0,138
550	0,838	0,152	0,152	1600	0,812	0,138	0,138
560	0,837	0,152	0,152	1650	0,810	0,137	0,137
570	0,836	0,151	0,151	1700	0,811	0,136	0,136
580	0,835	0,151	0,151	1750	0,807	0,137	0,137
590	0,833	0,150	0,150	1800	0,806	0,136	0,136
600	0,831	0,150	0,150	1850	0,800	0,131	0,131
610	0,829	0,150	0,150	1900	0,800	0,129	0,129
620	0,829	0,149	0,149	1950	0,798	0,125	0,125
630	0,826	0,149	0,149	2000	0,791	0,126	0,126
640	0,823	0,148	0,148	2050	0,797	0,126	0,126
650	0,821	0,147	0,147	2100	0,791	0,121	0,121
660	0,818	0,147	0,147	2200	0,754	0,111	0,111
670	0,815	0,146	0,146	2300	0,757	0,106	0,106
680	0,813	0,145	0,145	2400	0,748	0,098	0,098
690	0,811	0,144	0,144	2500	0,706	0,072	0,072
700	0,808	0,144	0,144				

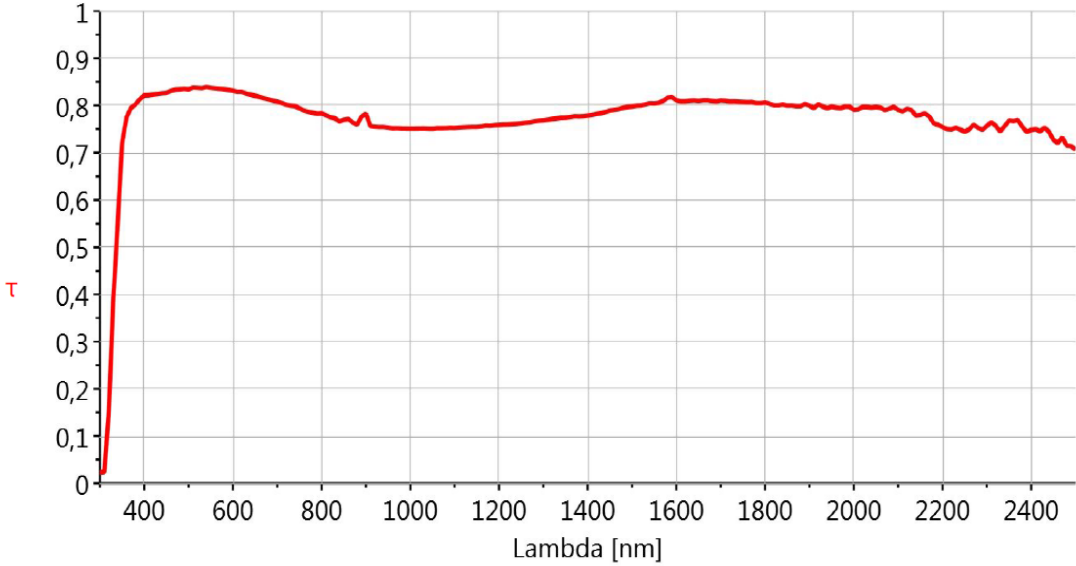
(*) incident radiation from the outside

(**) incident radiation from the inside

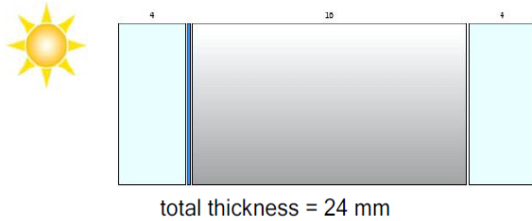
Glass 1 Spectral Values Graphical Demonstration



(*) incident radiation from the outside
(**) incident radiation from the inside



Details of Glass 2



Glazing from external to internal:

<p>Pane 1</p> <p>4 mm Float Glass ExtraClear ClimaGuard NT</p>		<p>Pane 2</p> <p>4 mm Float Glass ExtraClear ClimaGuard Dry</p>
<p>Spacer 1 - 16 mm</p> <p>10% Air 90% Argon</p>		

Results

Visible light (EN 410 - 2011)	Solar energy (EN 410 - 2011)
transmittance [%] $\tau_v = 78,4$	solar factor [%] $g = 58,7$
reflectance external [%] $\rho_v = 13,0$	shading coefficient [g/0.87] $sc = 0,67$
reflectance internal [%] $\rho_v = 13,2$	direct transmittance [%] $\tau_e = 54,8$
general colour rendering index [%] $R_a = 97,2$	direct reflectance external [%] $\rho_e = 26,8$
	direct reflectance internal [%] $\rho_e = 24,1$
Thermal properties (EN 673 - 2011)	direct absorption [%] $a = 18,4$
Design U-value [W/(m ² K)] $U_g = 1,0$	UV transmittance [%] $\tau_{uv} = 46,7$
slope $\alpha = 90^\circ$	secondary internal heat transfer factor [%] $q_i = 3,9$
	Other data
	estimated sound reduction index [dB] $R_w = \text{NPD}$
	(EN 717-1) $C = \text{NPD}$
	$C_{tr} = \text{NPD}$

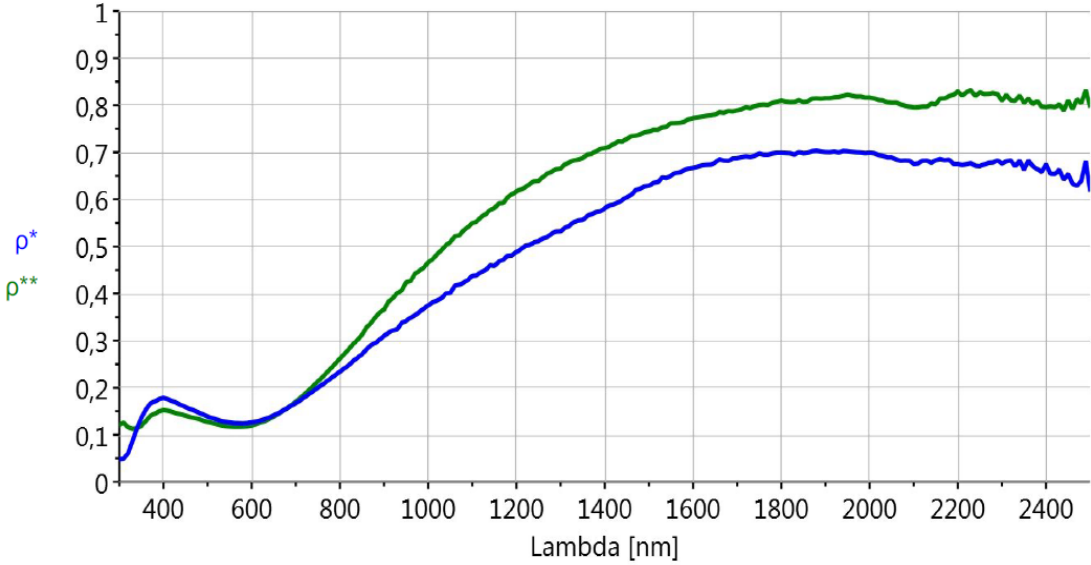
Glass 2 Spectral Values

λ [nm]	τ	ρ^*	ρ^{**}	λ [nm]	τ	ρ^*	ρ^{**}
300	0,000	0,049	0,140	710	0,662	0,173	0,178
310	0,004	0,050	0,126	720	0,650	0,180	0,187
320	0,057	0,061	0,116	730	0,637	0,187	0,195
330	0,207	0,087	0,113	740	0,624	0,193	0,204
340	0,389	0,114	0,114	750	0,611	0,200	0,213
350	0,527	0,136	0,119	760	0,597	0,206	0,222
360	0,615	0,153	0,129	770	0,584	0,213	0,232
370	0,659	0,166	0,140	780	0,572	0,220	0,242
380	0,673	0,171	0,145	790	0,559	0,227	0,252
390	0,700	0,176	0,150	800	0,545	0,234	0,262
400	0,719	0,178	0,152	850	0,487	0,271	0,312
410	0,726	0,176	0,151	900	0,433	0,310	0,366
420	0,732	0,172	0,149	950	0,391	0,342	0,424
430	0,736	0,168	0,146	1000	0,348	0,375	0,466
440	0,742	0,163	0,143	1050	0,316	0,401	0,510
450	0,751	0,159	0,141	1100	0,284	0,438	0,550
460	0,759	0,155	0,138	1150	0,252	0,459	0,582
470	0,767	0,151	0,136	1200	0,230	0,488	0,617
480	0,774	0,147	0,133	1250	0,203	0,511	0,640
490	0,780	0,143	0,130	1300	0,189	0,533	0,666
500	0,785	0,139	0,127	1350	0,168	0,556	0,688
510	0,789	0,136	0,125	1400	0,155	0,581	0,709
520	0,793	0,133	0,123	1450	0,144	0,605	0,729
530	0,794	0,130	0,121	1500	0,133	0,629	0,744
540	0,796	0,128	0,119	1550	0,122	0,651	0,762
550	0,795	0,126	0,118	1600	0,113	0,667	0,773
560	0,792	0,125	0,117	1650	0,102	0,678	0,781
570	0,791	0,124	0,117	1700	0,094	0,687	0,789
580	0,785	0,124	0,117	1750	0,085	0,697	0,801
590	0,779	0,125	0,118	1800	0,079	0,699	0,810
600	0,773	0,126	0,120	1850	0,071	0,698	0,807
610	0,767	0,128	0,123	1900	0,065	0,701	0,815
620	0,759	0,131	0,126	1950	0,061	0,703	0,822
630	0,748	0,133	0,129	2000	0,056	0,699	0,817
640	0,740	0,137	0,134	2050	0,053	0,689	0,805
650	0,730	0,141	0,139	2100	0,048	0,676	0,795
660	0,720	0,146	0,144	2200	0,040	0,676	0,830
670	0,709	0,151	0,150	2300	0,034	0,676	0,809
680	0,698	0,156	0,157	2400	0,038	0,675	0,796
690	0,687	0,162	0,164	2500	0,016	0,616	0,795
700	0,674	0,167	0,170				

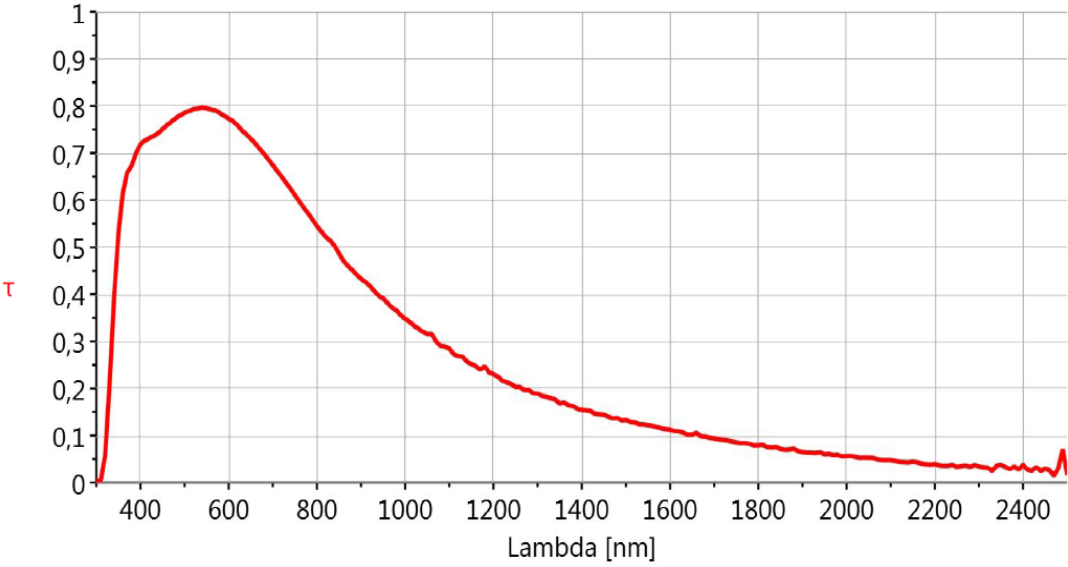
(*) incident radiation from the outside

(**) incident radiation from the inside

Glass 2 Spectral Values Graphical Demonstration



(*) incident radiation from the outside
(**) incident radiation from the inside



Details of Glass 3



total thickness = 24 mm

Glazing from external to internal:

Pane 1		Pane 2	
4 mm	Float Glass ExtraClear SunGuard SN 51/28	4 mm	SunGuard HP Amber 41/29 Float Glass ExtraClear
Spacer 1 - 16 mm			
10%	Air		
90%	Argon		

Results

Visible light (EN 410 - 2011)		Solar energy (EN 410 - 2011)	
transmittance [%]	$\tau_v = 25,3$	solar factor [%]	$g = 25,3$
reflectance external [%]	$\rho_v = 13,1$	shading coefficient [g/0.87]	$sc = 0,29$
reflectance internal [%]	$\rho_v = 27,4$	direct transmittance [%]	$\tau_e = 12,8$
general colour rendering index [%]	$R_a = 83,4$	direct reflectance external [%]	$\rho_e = 40,2$
		direct reflectance internal [%]	$\rho_e = 41,5$
		direct absorption [%]	$a = 47,0$
Thermal properties (EN 673 - 2011)		UV transmittance [%]	$\tau_{uv} = 9,4$
U-value [W/(m ² K)]	$U_g = 1,0$	secondary internal heat transfer factor [%]	$q_i = 12,5$
slope $\alpha = 90^\circ$		Other data	
		estimated sound reduction index [dB]	$R_w = \text{NPD}$
		(EN 717-1)	$C = \text{NPD}$
			$C_{tr} = \text{NPD}$

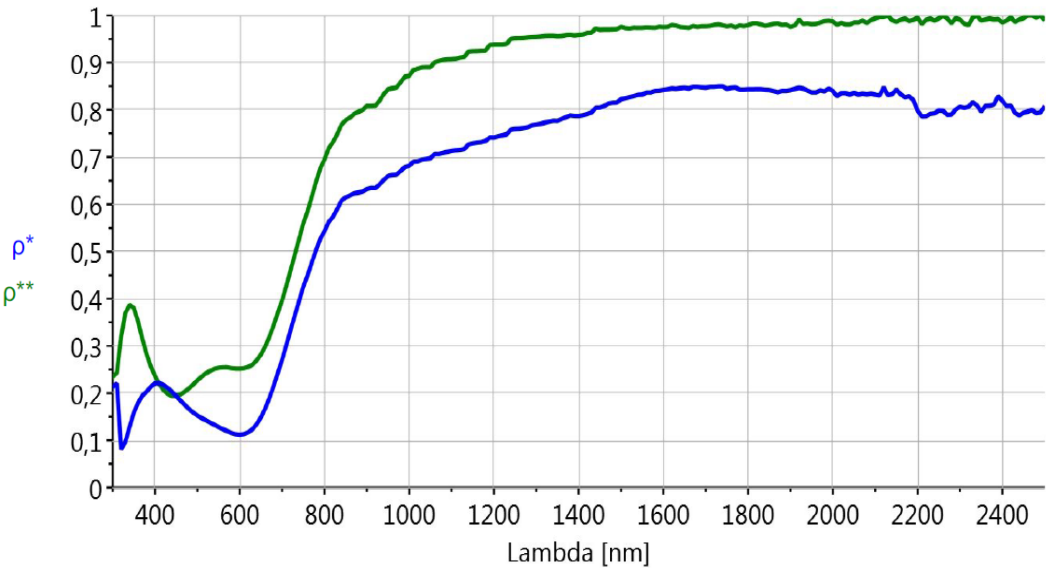
Glass 3 Spectral Values

λ [nm]	τ	ρ^*	ρ^{**}	λ [nm]	τ	ρ^*	ρ^{**}
300	0,000	0,360	0,186	710	0,106	0,302	0,427
310	0,000	0,221	0,243	720	0,097	0,334	0,461
320	0,002	0,081	0,319	730	0,088	0,365	0,493
330	0,016	0,097	0,370	740	0,080	0,395	0,527
340	0,046	0,129	0,387	750	0,072	0,425	0,560
350	0,084	0,159	0,381	760	0,065	0,449	0,585
360	0,125	0,179	0,352	770	0,059	0,477	0,616
370	0,165	0,195	0,315	780	0,054	0,503	0,647
380	0,193	0,203	0,283	790	0,049	0,527	0,676
390	0,223	0,214	0,257	800	0,044	0,543	0,695
400	0,246	0,221	0,236	850	0,029	0,615	0,778
410	0,259	0,221	0,220	900	0,019	0,632	0,808
420	0,267	0,217	0,207	950	0,013	0,660	0,843
430	0,274	0,211	0,199	1000	0,010	0,682	0,872
440	0,279	0,203	0,194	1050	0,006	0,698	0,890
450	0,284	0,194	0,194	1100	0,005	0,714	0,908
460	0,288	0,184	0,197	1150	0,004	0,729	0,925
470	0,290	0,175	0,203	1200	0,004	0,741	0,938
480	0,290	0,167	0,210	1250	0,003	0,760	0,952
490	0,289	0,159	0,218	1300	0,003	0,769	0,954
500	0,287	0,153	0,227	1350	0,002	0,777	0,956
510	0,284	0,147	0,235	1400	0,002	0,787	0,959
520	0,279	0,142	0,242	1450	0,001	0,805	0,970
530	0,274	0,138	0,247	1500	0,001	0,823	0,976
540	0,269	0,133	0,251	1550	0,001	0,832	0,974
550	0,263	0,128	0,254	1600	0,001	0,842	0,975
560	0,256	0,124	0,254	1650	0,001	0,847	0,975
570	0,249	0,120	0,255	1700	0,001	0,847	0,977
580	0,240	0,116	0,253	1750	0,000	0,844	0,977
590	0,232	0,113	0,252	1800	0,001	0,843	0,979
600	0,223	0,112	0,252	1850	0,001	0,842	0,980
610	0,214	0,113	0,253	1900	0,000	0,842	0,976
620	0,204	0,117	0,255	1950	0,000	0,837	0,982
630	0,193	0,124	0,261	2000	0,001	0,840	0,988
640	0,183	0,135	0,270	2050	0,000	0,837	0,985
650	0,171	0,149	0,282	2100	0,001	0,832	0,994
660	0,160	0,168	0,299	2200	0,001	0,798	0,996
670	0,149	0,190	0,319	2300	0,000	0,806	0,991
680	0,137	0,215	0,344	2400	0,000	0,819	0,985
690	0,126	0,243	0,371	2500	0,000	0,808	0,990
700	0,116	0,271	0,396				

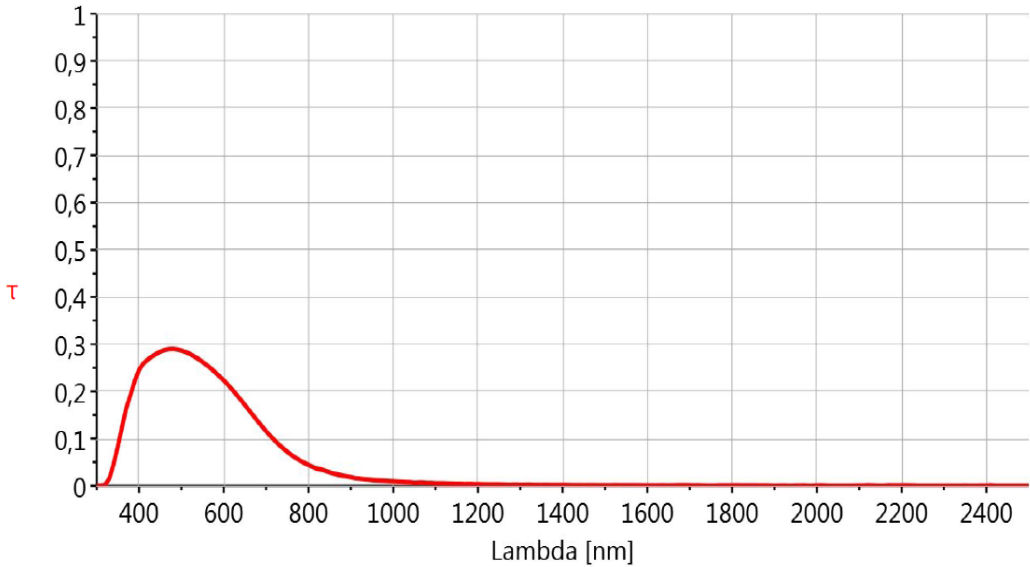
(*) incident radiation from the outside

(**) incident radiation from the inside

Glass 3 Spectral Values Graphical Demonstration



(*) incident radiation from the outside
(**) incident radiation from the inside



APPENDIX B

List of Figures

Figure 1.1 Air temperature distribution with “Glass 1” windows, from 09:00 to 17:00 on cross-sectional view at the height of 1.8 m.	107
Figure 1.2 Mean radiant temperature distribution with “Glass 1” windows, from 09:00 to 17:00 on cross-sectional view at the height of 1.8 m.	108
Figure 1.3 Operative temperature distribution with “Glass 1” windows, from 09:00 to 17:00, on cross-sectional view at the height of 1.8 m.	109
Figure 1.4 Relative Humidity with “Glass 1” windows, from 09:00 to 17:00 on cross-sectional view at the height of 1.8 m.	110
Figure 1.5 Predicted mean vote distribution with “Glass 1” windows, from 09:00 to 17:00 on cross-sectional view at the height of 1.8 m.	111
Figure 1.6 Predicted percent dissatisfied distribution with “Glass 1” windows, from 09:00 to 14:00 on cross-sectional view at the height of 1.8 m.	112
Figure 2.1 Air temperature distribution with “Glass 2” windows, from 09:00 to 17:00 on cross-sectional view at the height of 1.8 m.	113
Figure 2.2 Mean radiant temperature distribution with “Glass 2” windows, from 09:00 to 17:00 on cross-sectional view at the height of 1.8 m.	114
Figure 2.3 Operative temperature distribution with “Glass 2” windows, from 09:00 to 17:00, on cross-sectional view at the height of 1.8 m.	115
Figure 2.4 Relative humidity with “Glass 2” windows, from 09:00 to 17:00 on cross-sectional view at the height of 1.8 m.	116
Figure 2.5 Predicted mean vote distribution with “Glass 2” windows, from 09:00 to 17:00 on cross-sectional view at the height of 1.8 m.	117
Figure 2.6 Predicted percent dissatisfied distribution with “Glass 2” windows, from 09:00 to 14:00 on cross-sectional view at the height of 1.8 m.	118
Figure 3.1 Air temperature distribution with “Glass 3” windows, from 09:00 to 17:00 on cross-sectional view at the height of 1.8 m.	119
Figure 3.2 Mean radiant temperature distribution with “Glass 3” windows, from 09:00 to 17:00 on cross-sectional view at the height of 1.8 m.	120
Figure 3.3 Operative temperature distribution with “Glass 3” windows, from 09:00 to 17:00, on cross-sectional view at the height of 1.8 m.	121

Figure 3.4 Relative humidity with “Glass 3” windows, from 09:00 to 17:00 on cross-sectional view at the height of 1.8 m.	122
Figure 3.5 Predicted mean vote distribution with “Glass 3” windows, from 09:00 to 17:00 on cross-sectional view at the height of 1.8 m.	123
Figure 3.6 Predicted percent dissatisfied distribution with “Glass 3” windows, from 09:00 to 14:00 on cross-sectional view at the height of 1.8 m.	124
Figure 4.1 Air Temperature distribution with “Glass 3 and new diffuser” from 09:00 to 17:00 on cross-sectional view at the height of 1.8 m.	125
Figure 4.2 Mean radiant temperature distribution with “Glass 3 and new diffuser” from 09:00 to 17:00 on cross-sectional view at the height of 1.8 m.	126
Figure 4.3 Operative temperature distribution with “Glass 3 and new diffuser” from 09:00 to 17:00 on cross-section view at the height of 1.8 m.	178
Figure 4.4 Relative humidity distribution with “Glass 3 and new diffuser” from 09:00 to 17:00 on cross-sectional view at the height of 1.8 m.	128
Figure 4.5 Predicted mean vote distribution with “Glass 3 and new diffuser” from 09:00 to 17:00 on cross-sectional view at the height of 1.8 m.	129
Figure 4.6 Predicted percent dissatisfied distribution with “Glass 3 and new diffuser” from 09:00 to 14:00 on cross-sectional view at the height of 1.8 m.	130

CROSS-SECTIONAL IMAGES IN COMFORT ZONE

The cross-sectional images parallel to floor are visualized according to the numerical results obtained at one hour intervals within the comfort zone. Images in the sequence, air temperature, mean radiant temperature, operative temperature, relative humidity, predicted mean vote and predicted percent of dissatisfied distribution are given below. These figures show results of four different scenarios. These scenarios are;

1. First Scenario: Highly Transmittance, Glass 1
2. Second Scenario: Middle Transmittance, Glass 2
3. Third Scenario: Low Transmittance, Glass 3
4. Fourth Scenario: Low Transmittance, Glass 3 and New Designed Diffuser

In Chapter 5, numerical results for the comfort Zone 1 and Zone 2 was given in graphics. In these figures, the results are visualized for all comfort areas with the zones.

First Scenario: Highly Transmittance, Glass 1

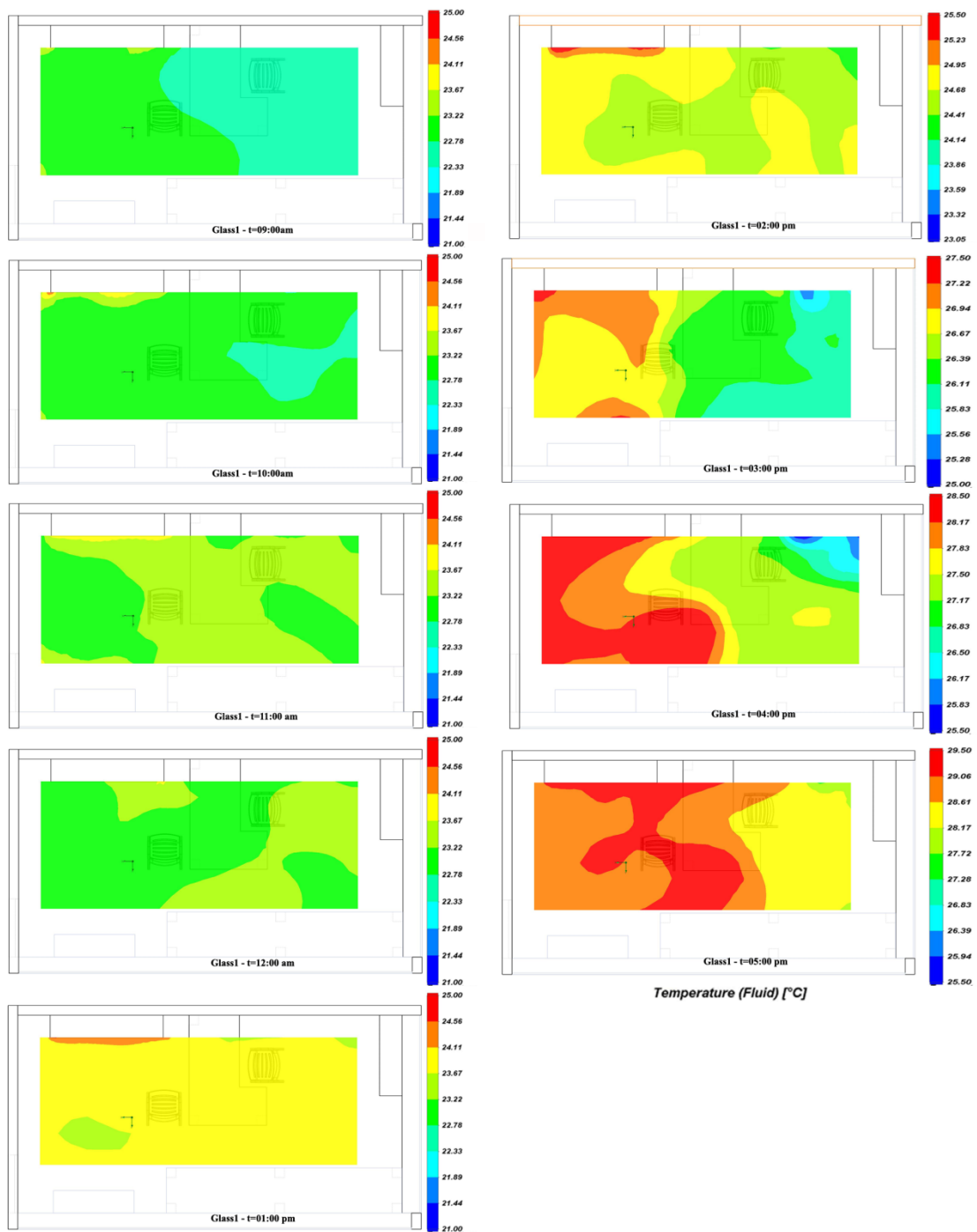


Figure 1.1 Air temperature distribution with “Glass 1” windows, from 09:00 to 17:00 on cross-sectional view at the height of 1.8 m.

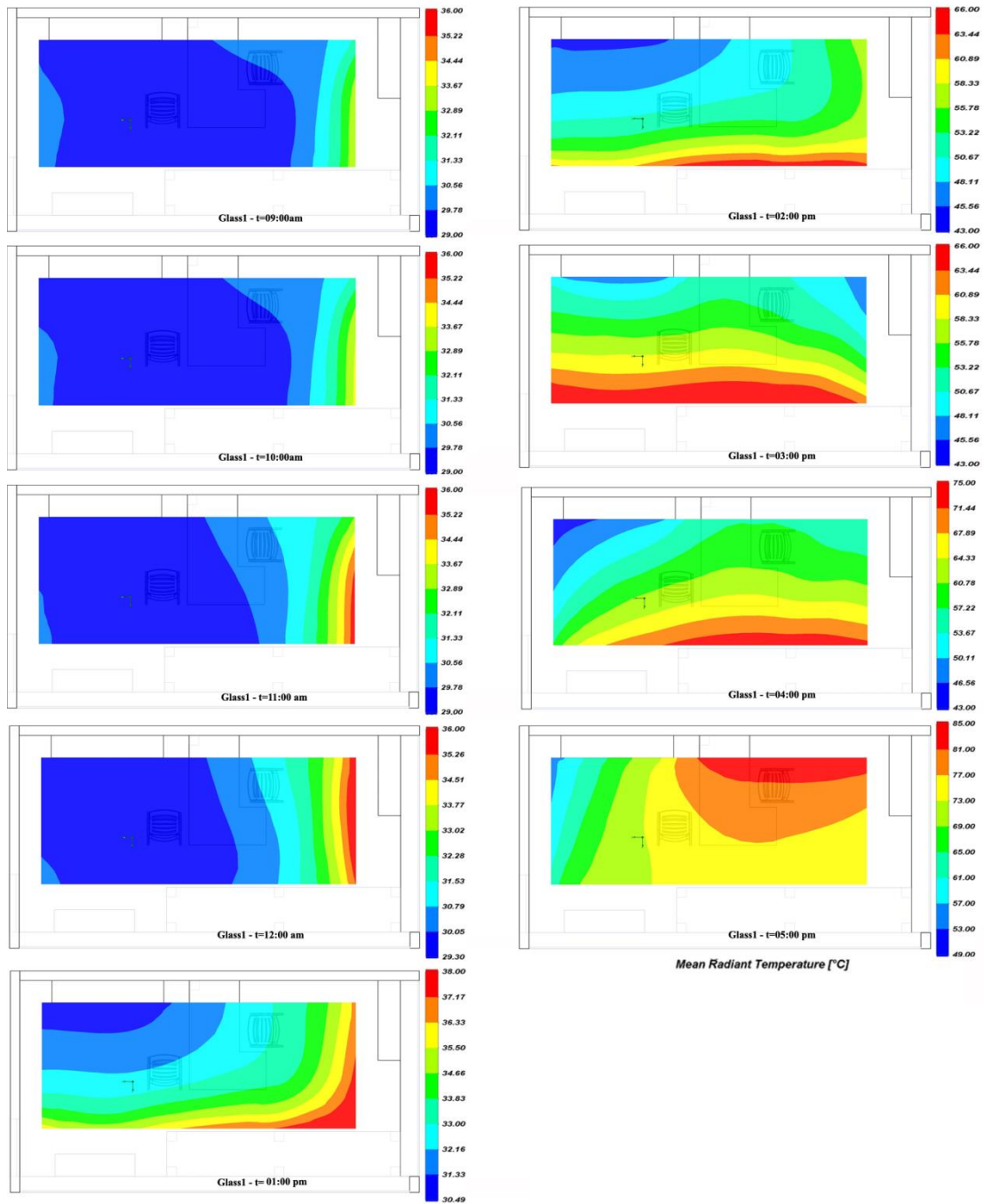


Figure 1.2 Mean radiant temperature distribution with “Glass 1” windows, from 09:00 to 17:00 on cross-sectional view at the height of 1.8 m.

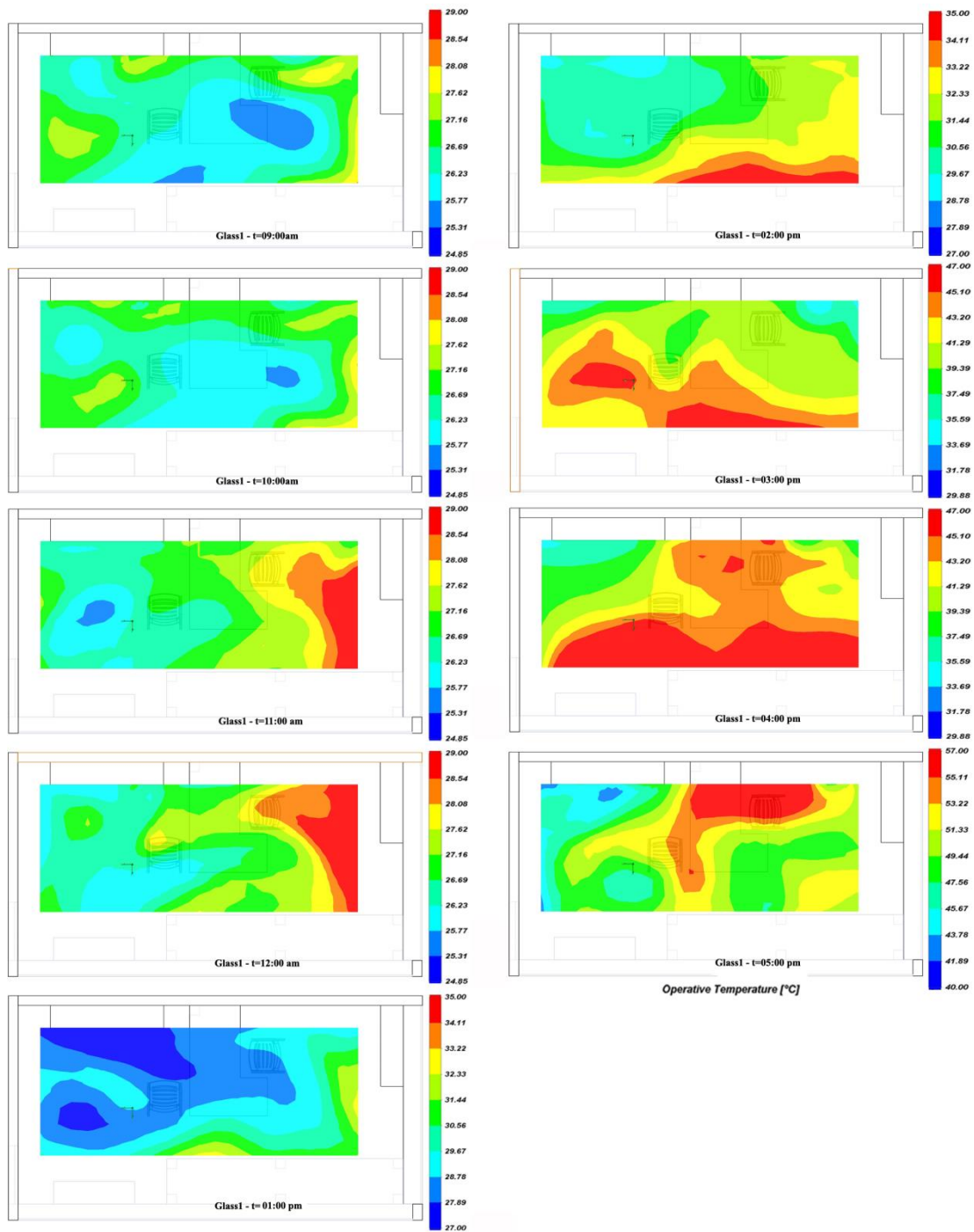


Figure 1.3 Operative temperature distribution with “Glass 1” windows, from 09:00 to 17:00, on cross-sectional view at the height of 1.8 m.

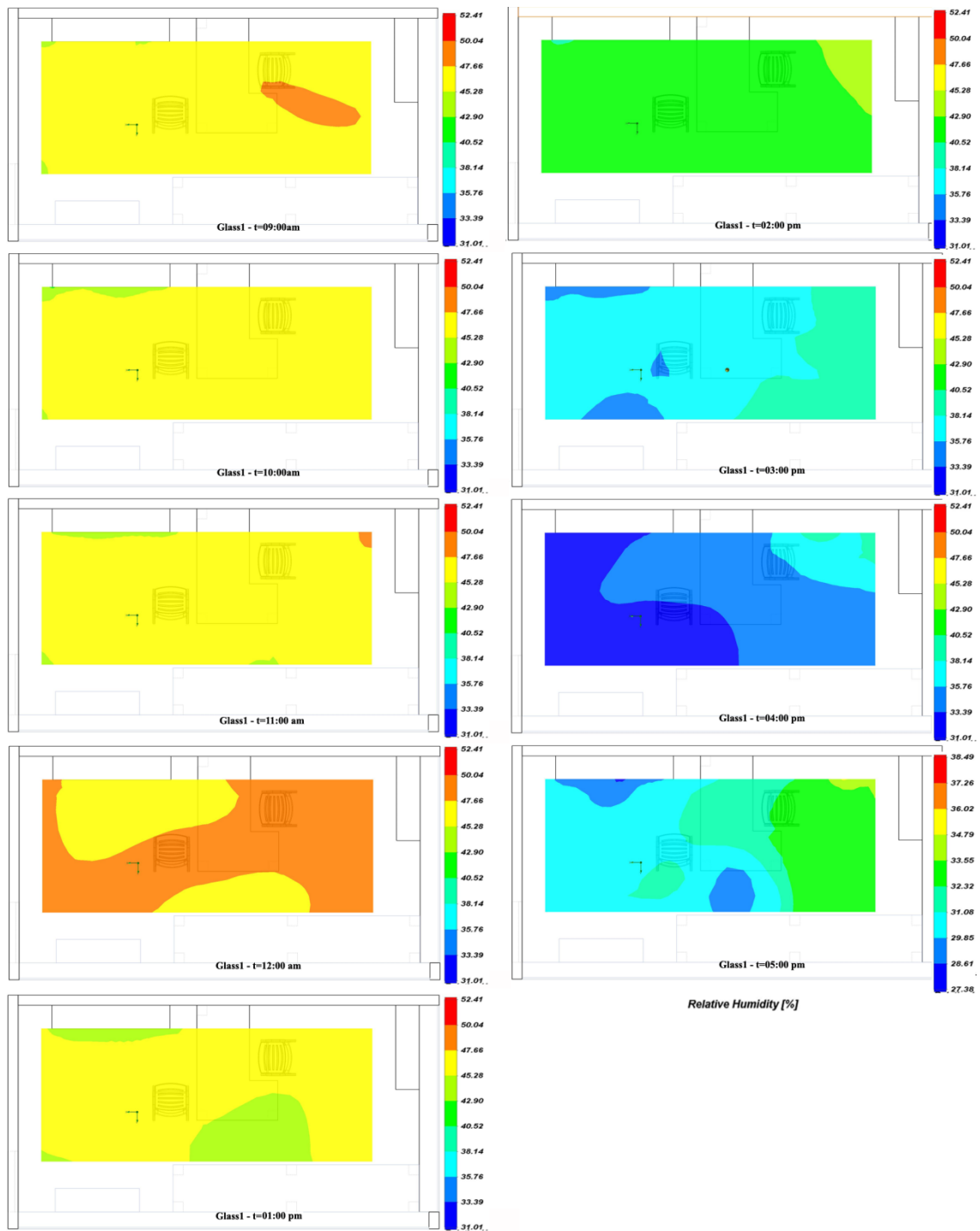


Figure 1.4 Relative humidity with “Glass 1” windows, from 09:00 to 17:00 on cross-sectional view at the height of 1.8 m.

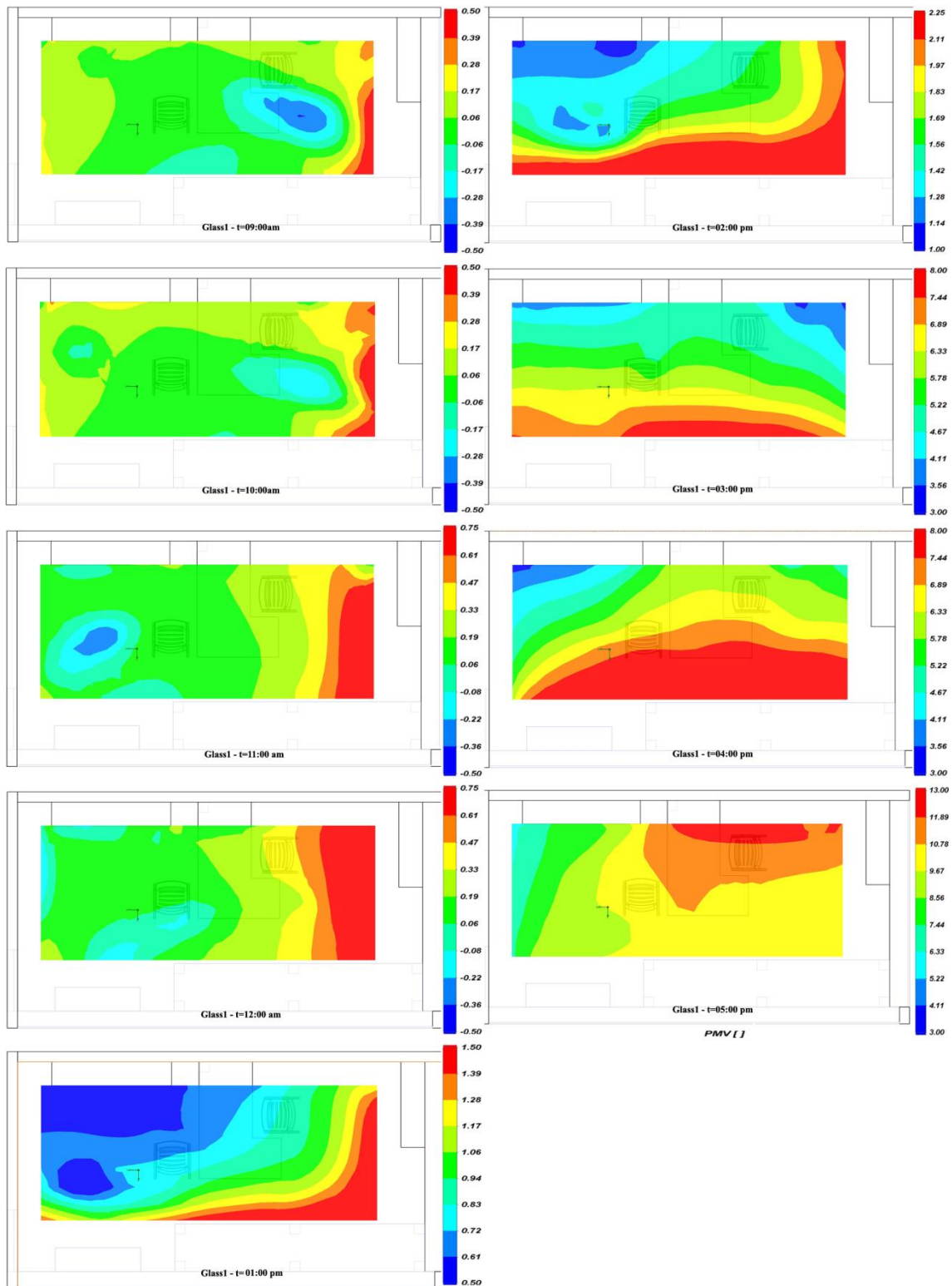


Figure 1.5 Predicted mean vote distribution with “Glass 1” windows, from 09:00 to 17:00 on cross-sectional view at the height of 1.8 m.

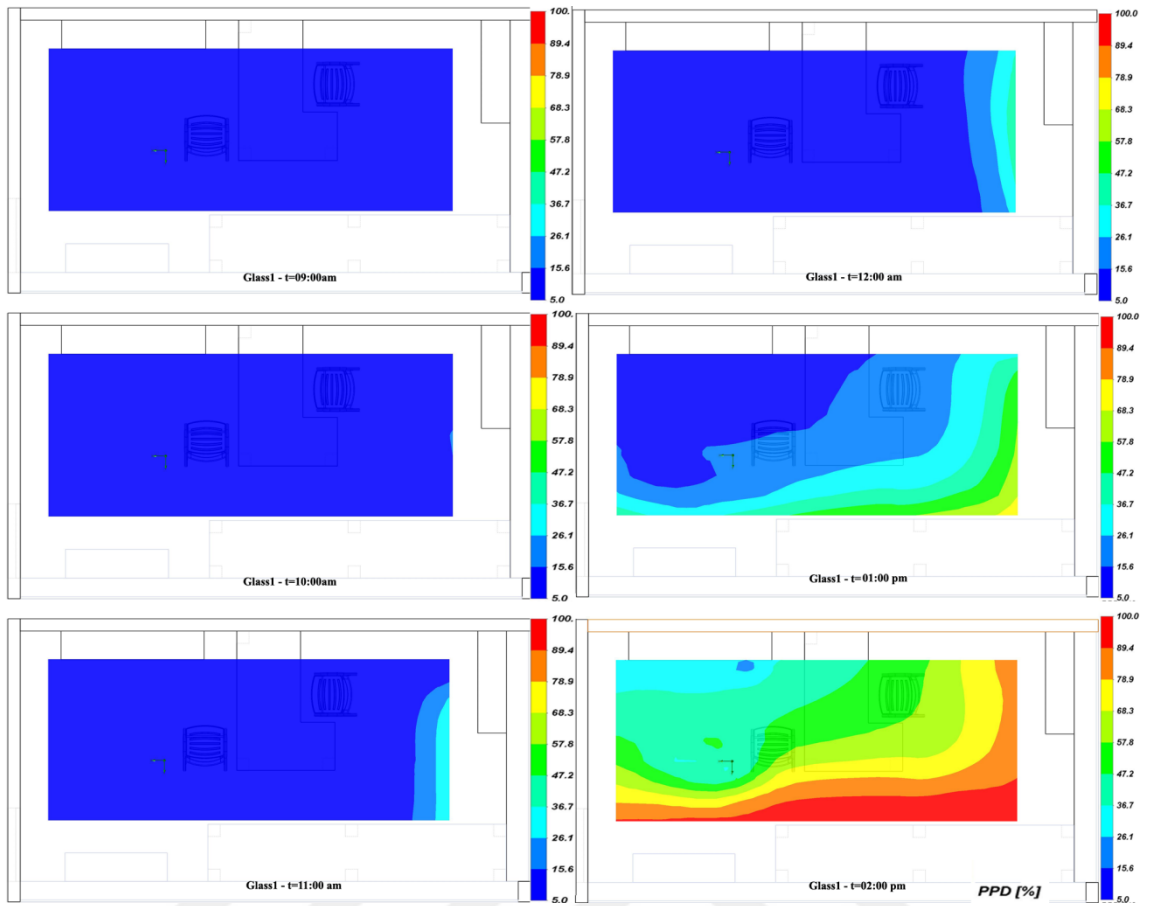


Figure 1.6 Predicted percent dissatisfied distribution with “Glass 1” windows, from 09:00 to 14:00 on cross-sectional view at the height of 1.8 m.

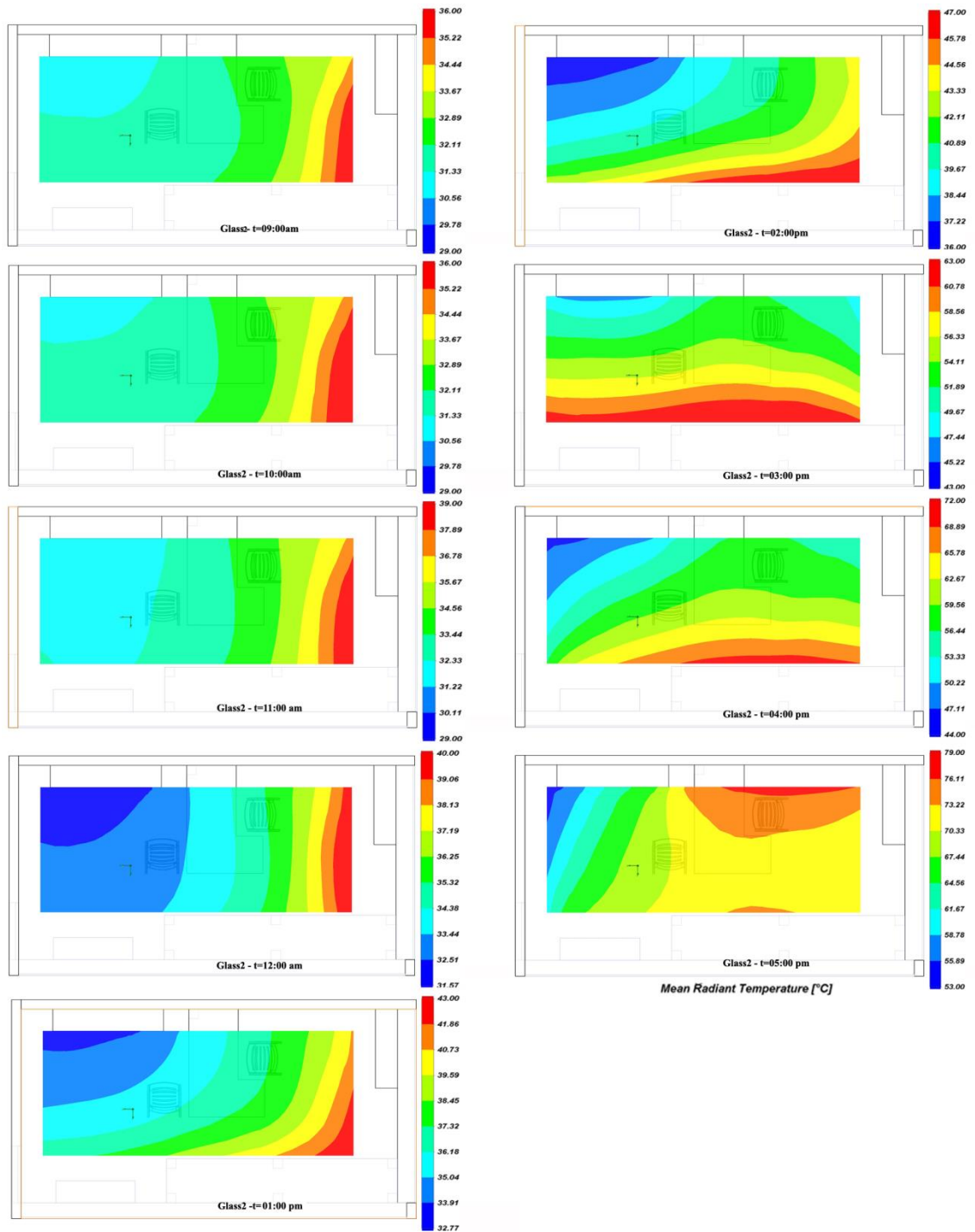


Figure 2.2 Mean radiant temperature distribution with “Glass 2” windows, from 09:00 to 17:00 on cross-sectional view at the height of 1.8 m.

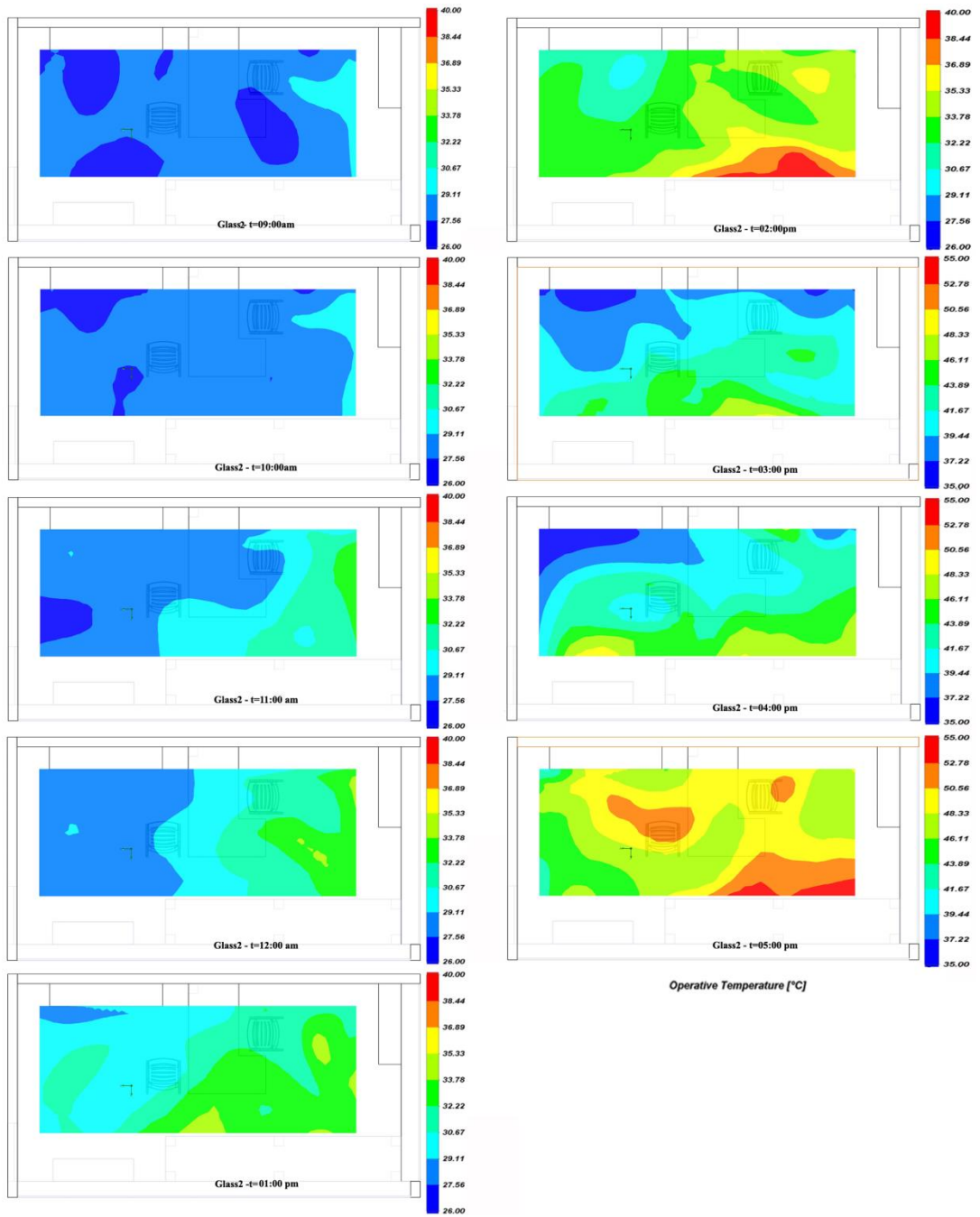


Figure 2.3 Operative temperature distribution with “Glass 2” windows, from 09:00 to 17:00, on cross-sectional view at the height of 1.8 m.

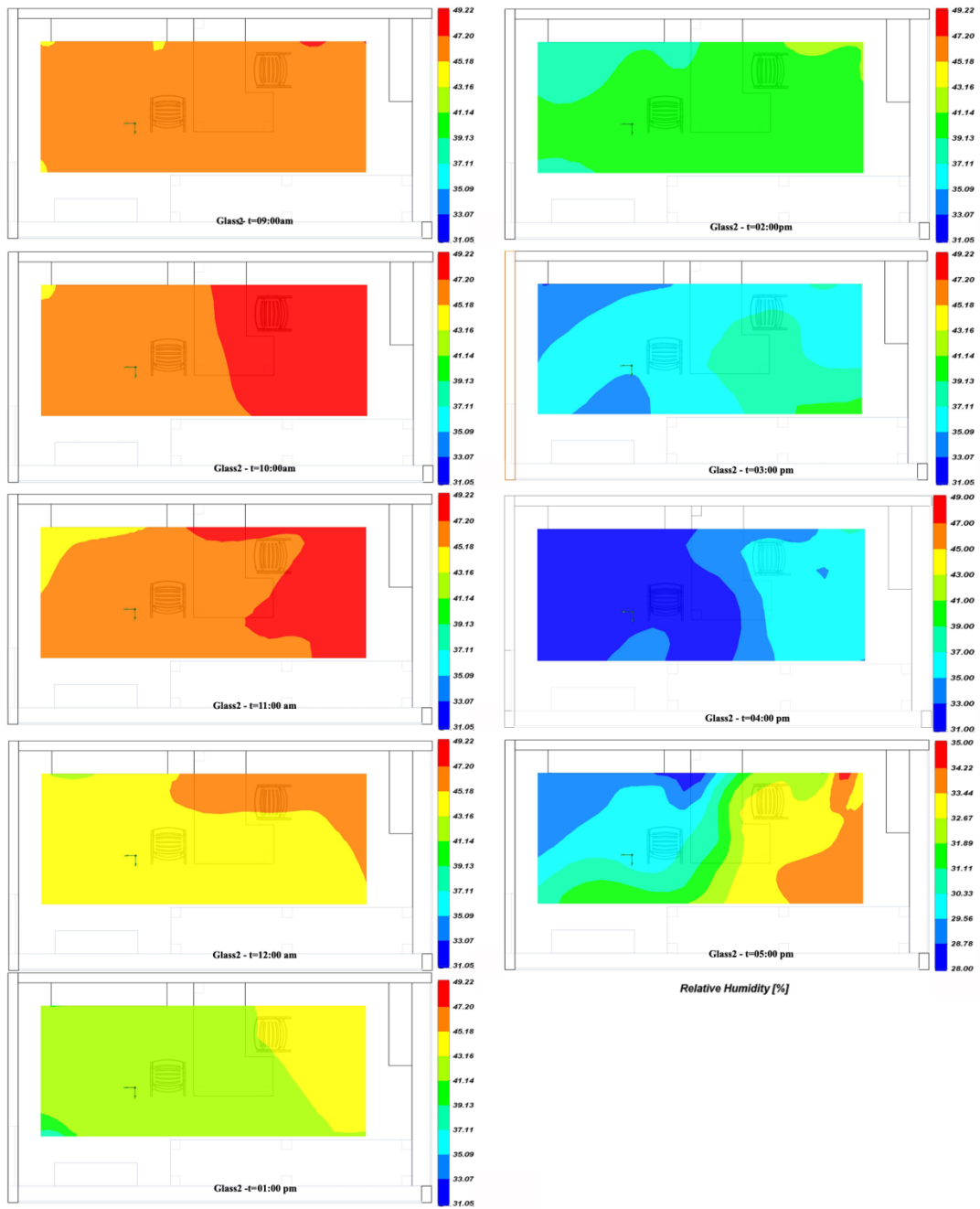


Figure 2.4 Relative Humidity with “Glass 2” windows, from 09:00 to 17:00 on cross-sectional view at the height of 1.8 m.

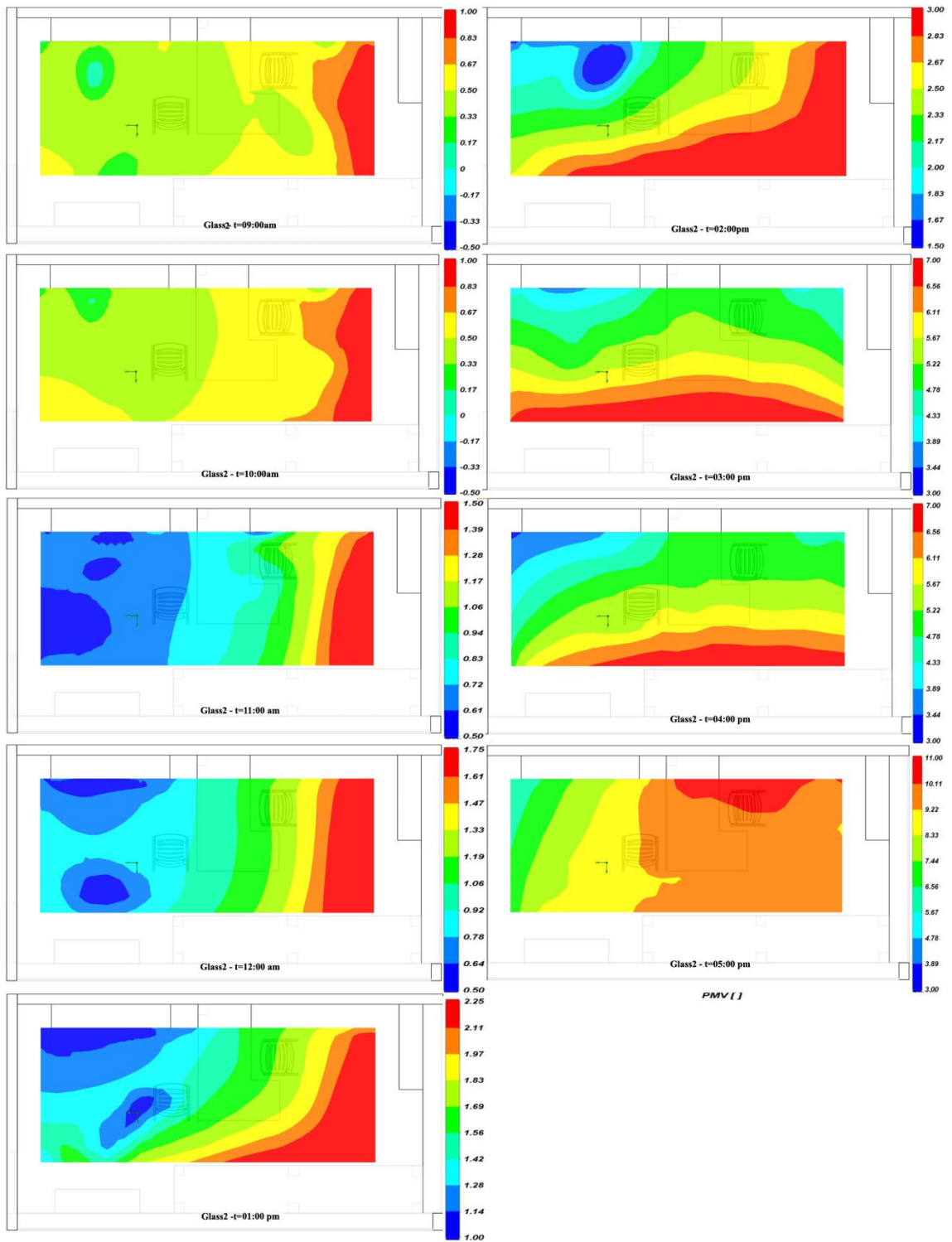


Figure 2.5 Predicted mean vote distribution with “Glass 2” windows, from 09:00 to 17:00 on cross-sectional view at the height of 1.8 m.

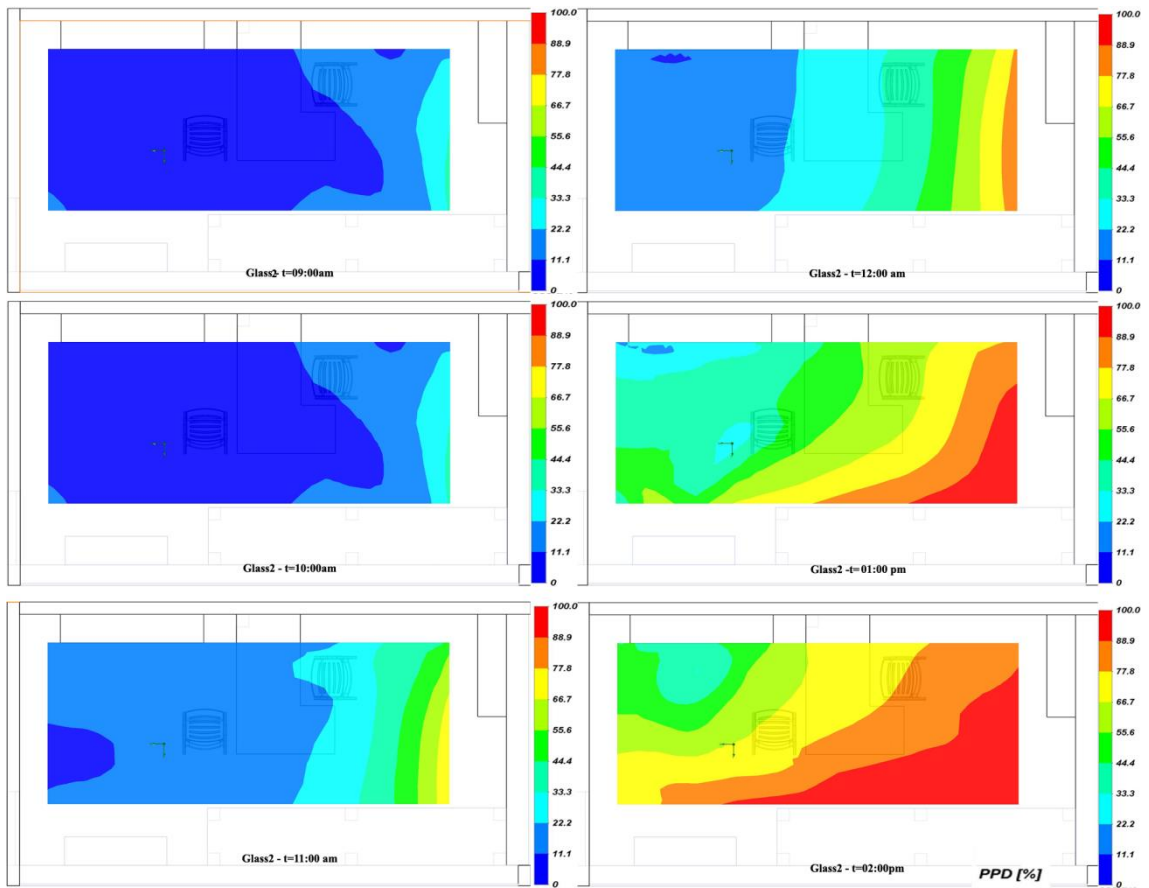


Figure 2.6 Predicted percent dissatisfied distribution with “Glass 2” windows, from 09:00 to 14:00 on cross-sectional view at the height of 1.8 m.

Third Scenario: Low Transmittance, Glass 3

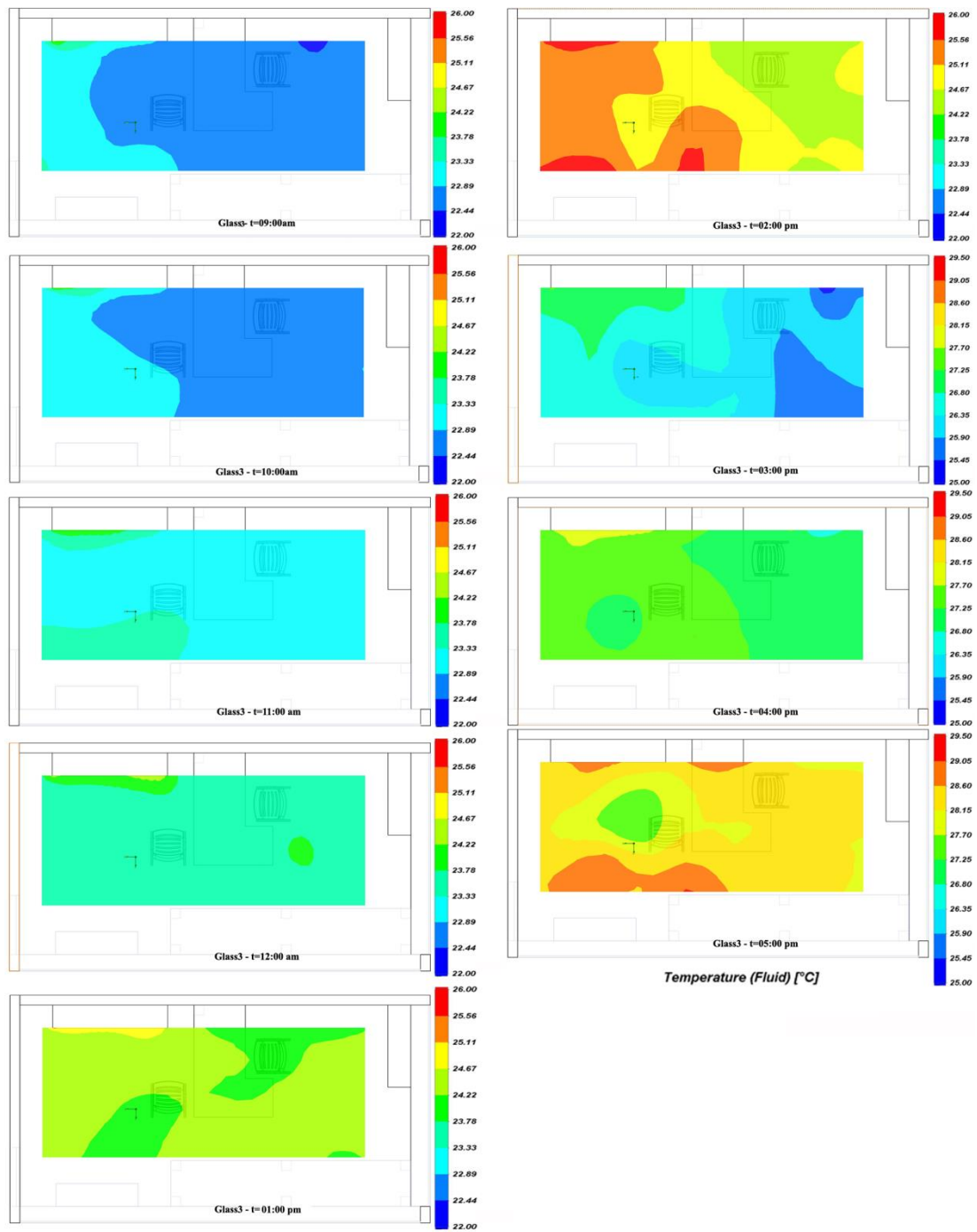


Figure 3.1 Air temperature distribution with “Glass 3” windows, from 09:00 to 17:00 on cross-sectional view at the height of 1.8 m.

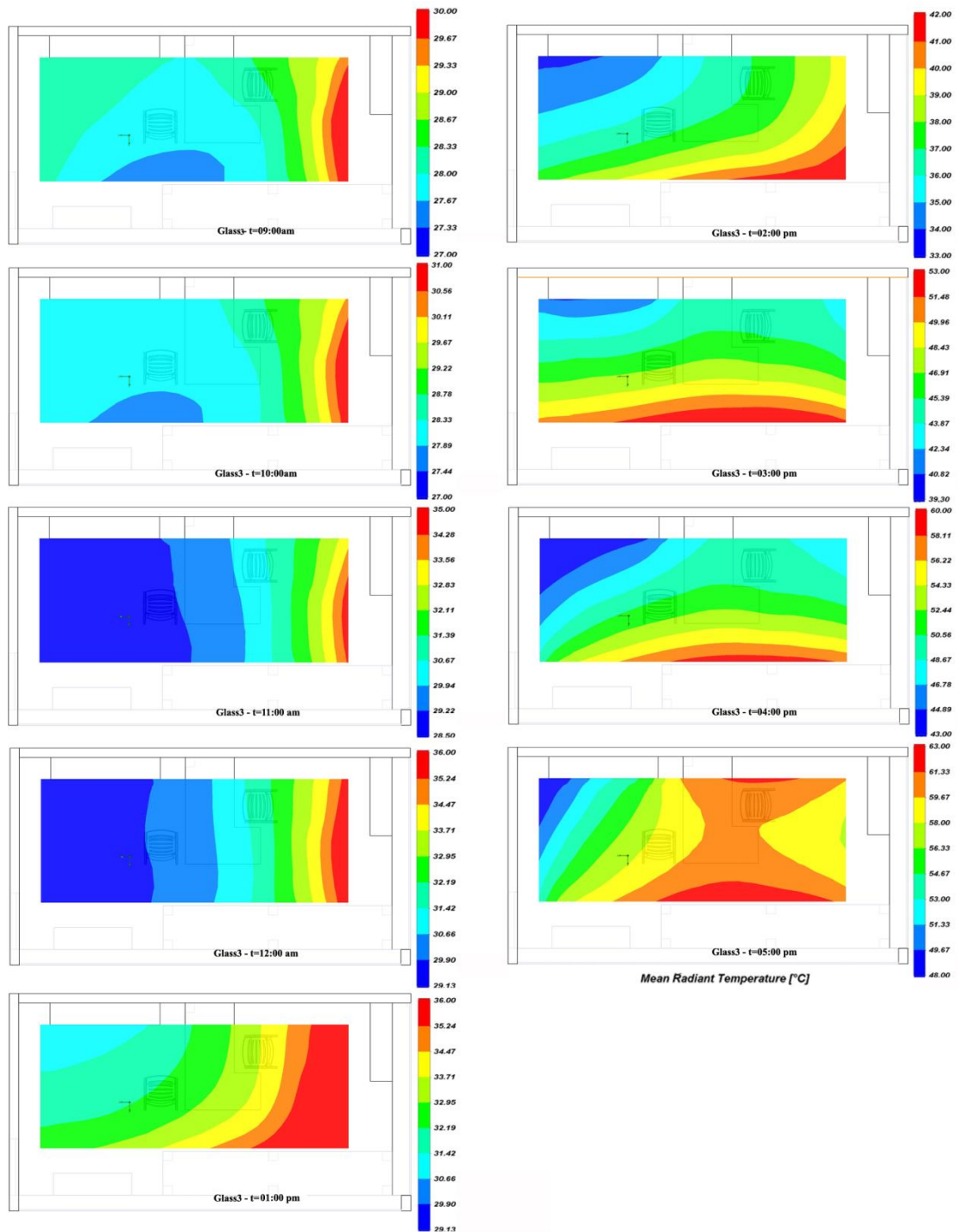


Figure 3.2 Mean radiant temperature distribution with “Glass 3” windows, from 09:00 to 17:00 on cross-sectional view at the height of 1.8 m.

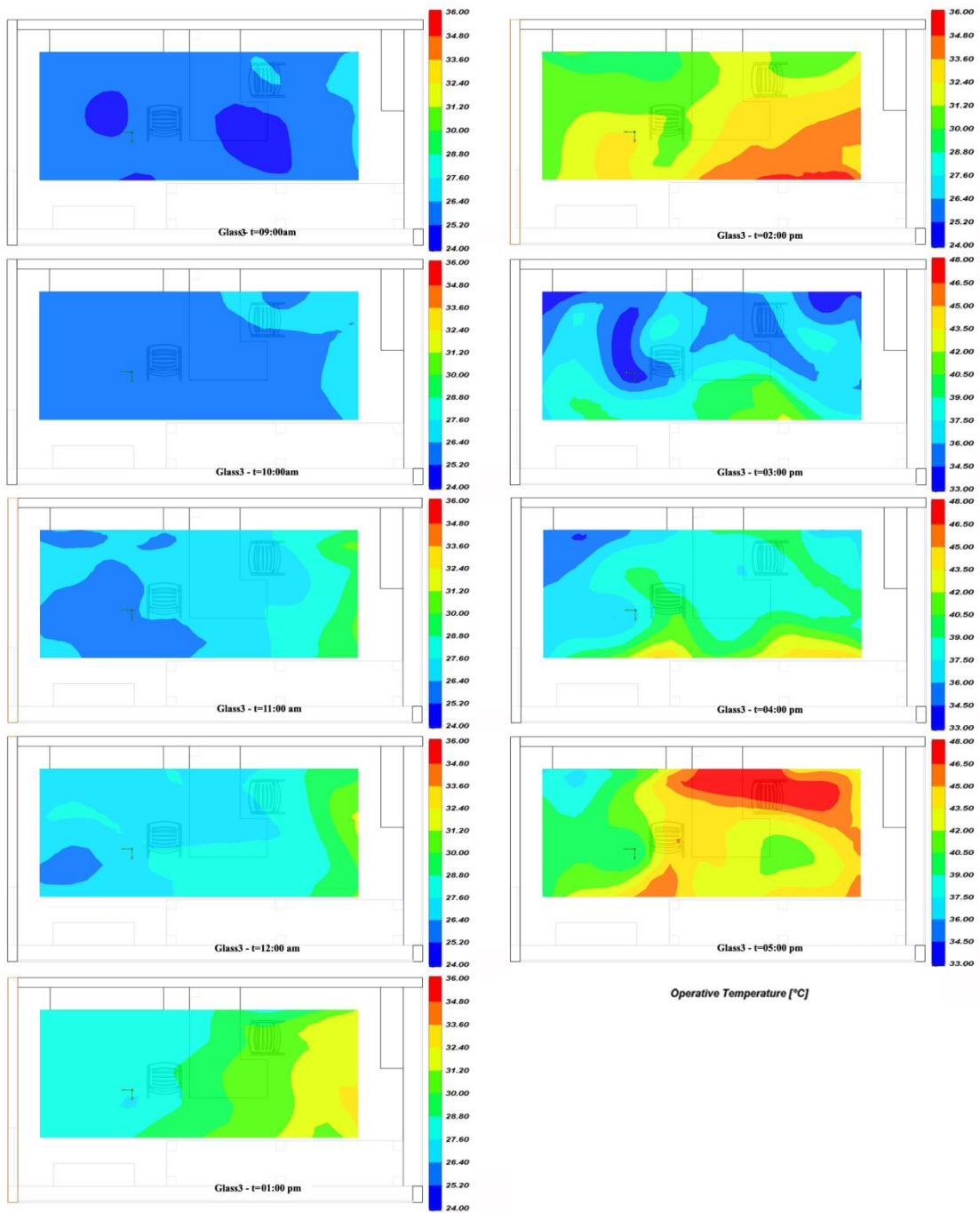


Figure 3.3 Operative temperature distribution with “Glass 3” windows, from 09:00 to 17:00, on cross-sectional view at the height of 1.8 m.

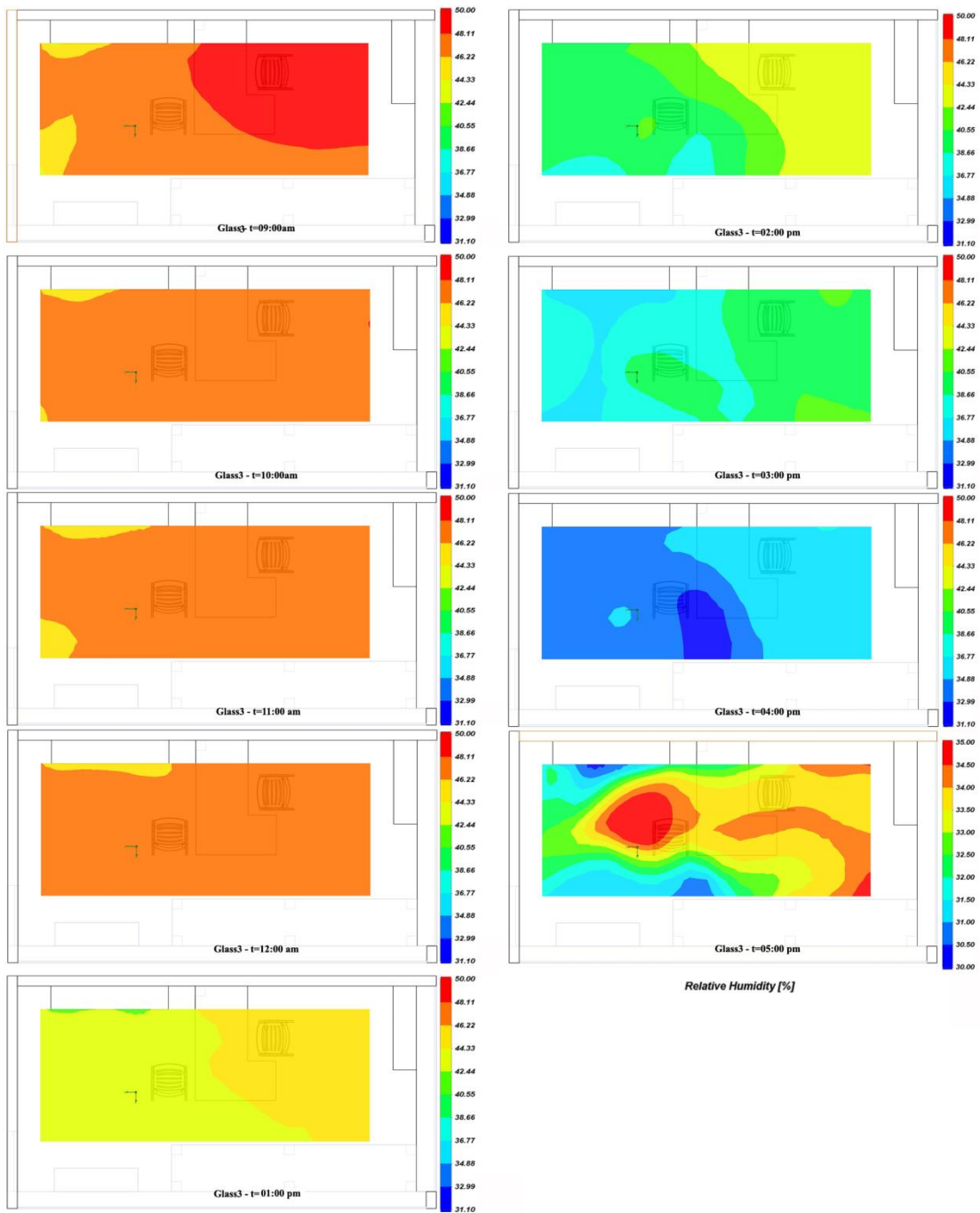


Figure 3.4 Relative Humidity with “Glass 3” windows, from 09:00 to 17:00 on cross-sectional view at the height of 1.8 m.

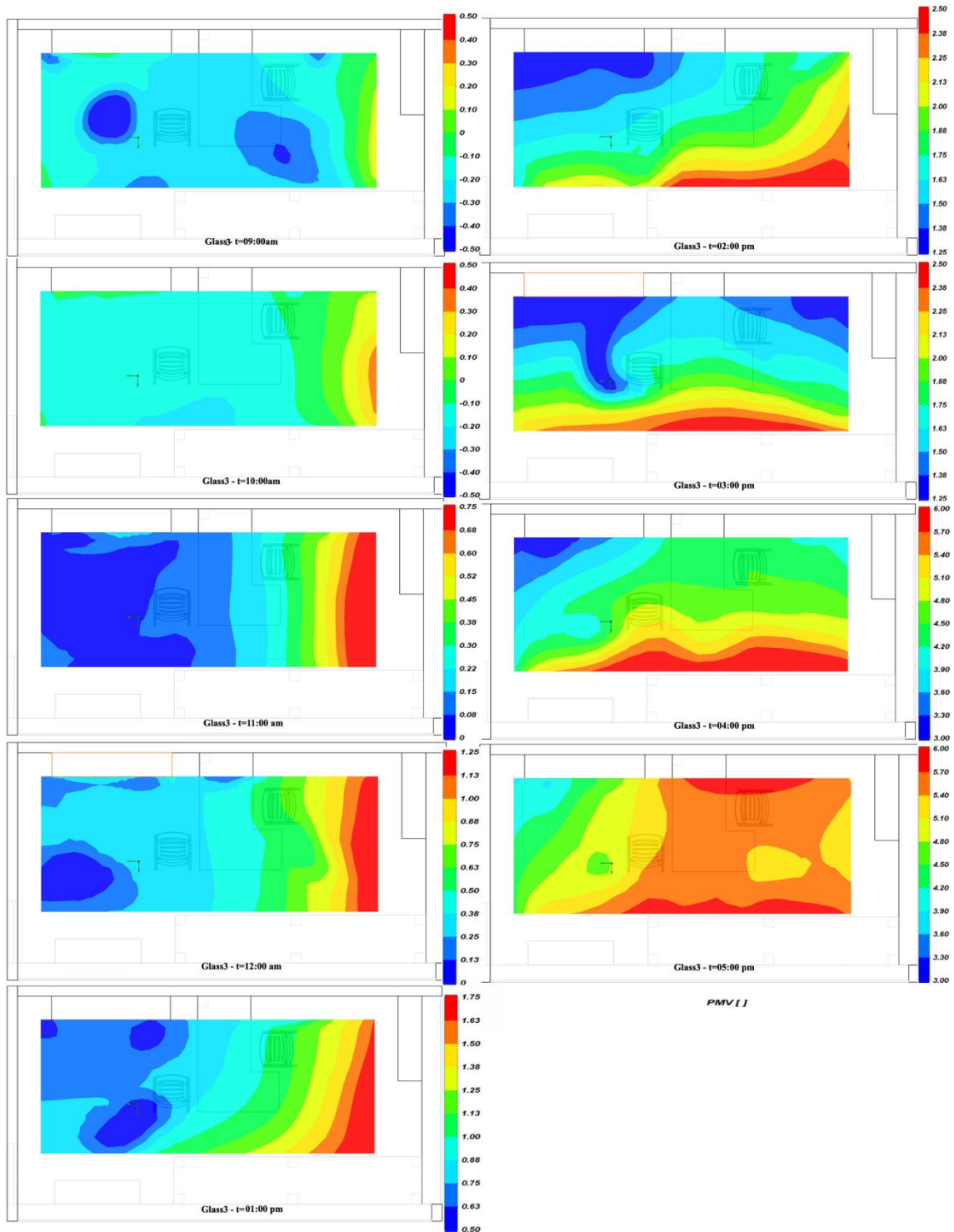


Figure 3.5 Predicted mean vote distribution with “Glass 3” windows, from 09:00 to 17:00 on cross-sectional view at the height of 1.8 m.

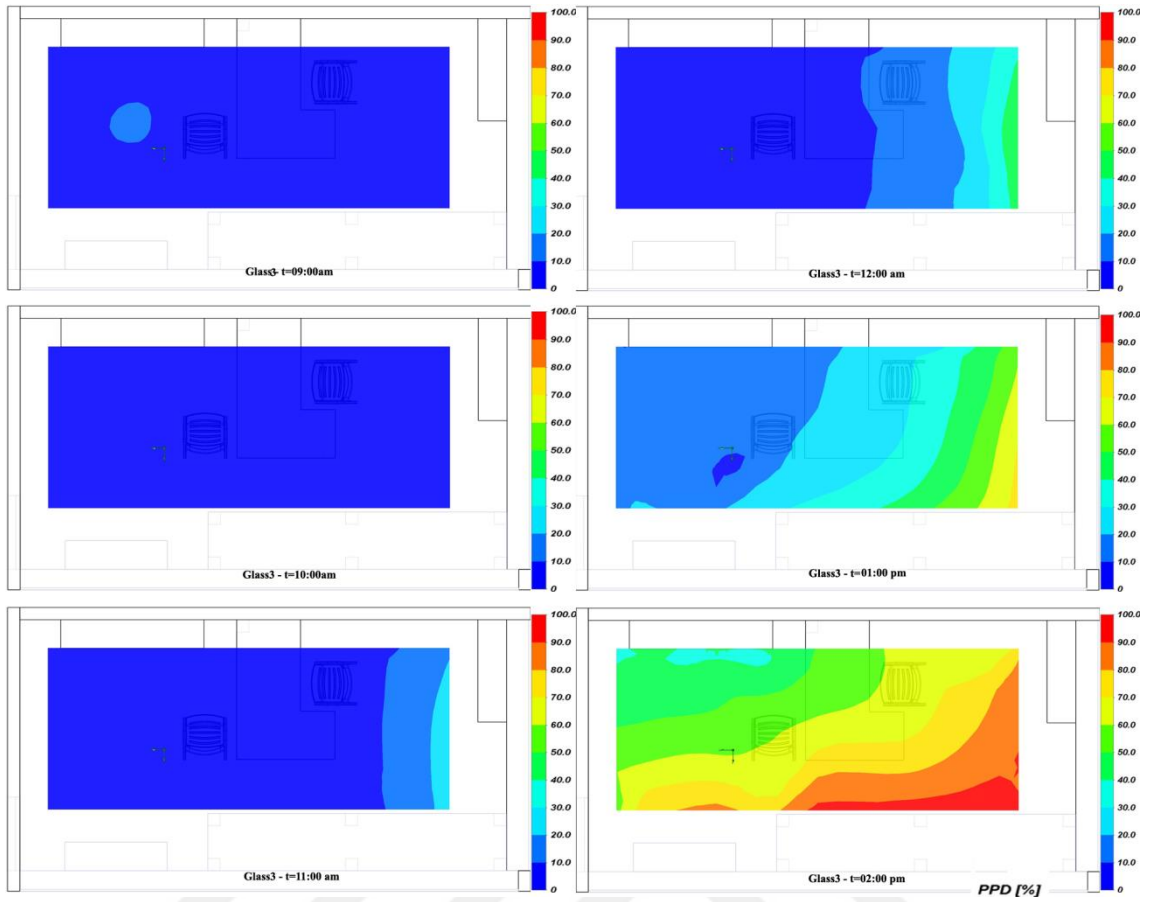


Figure 3.6 Predicted percent dissatisfied distribution with “Glass 3” windows, from 09:00 to 14:00 on cross-sectional view at the height of 1.8 m.

Fourth Scenario: Low Transmittance, Glass 3 and New Designed Diffuser

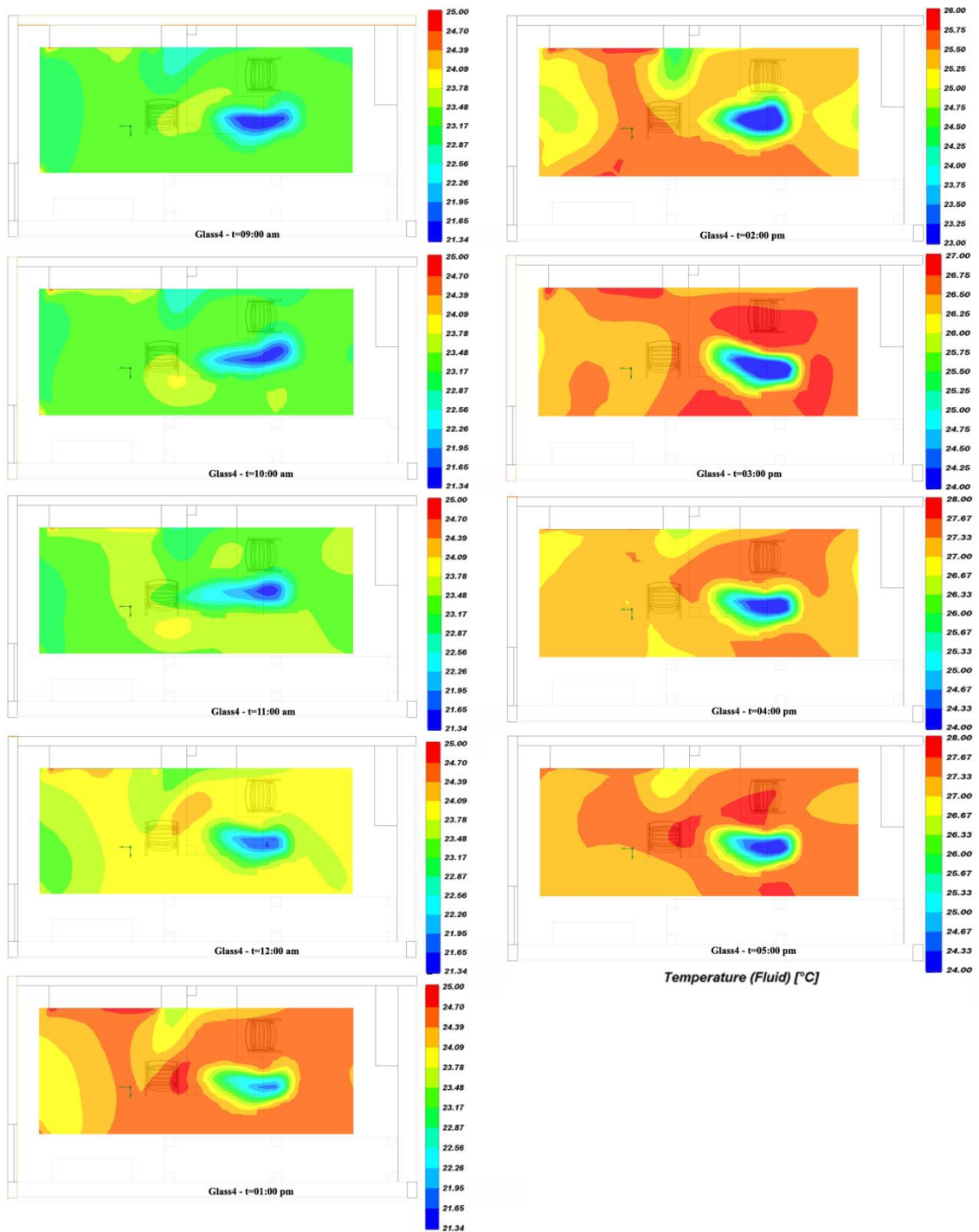


Figure 4.1 Air temperature distribution with “Glass 3 and new diffuser” from 09:00 to 17:00 on cross-sectional view at the height of 1.8 m.

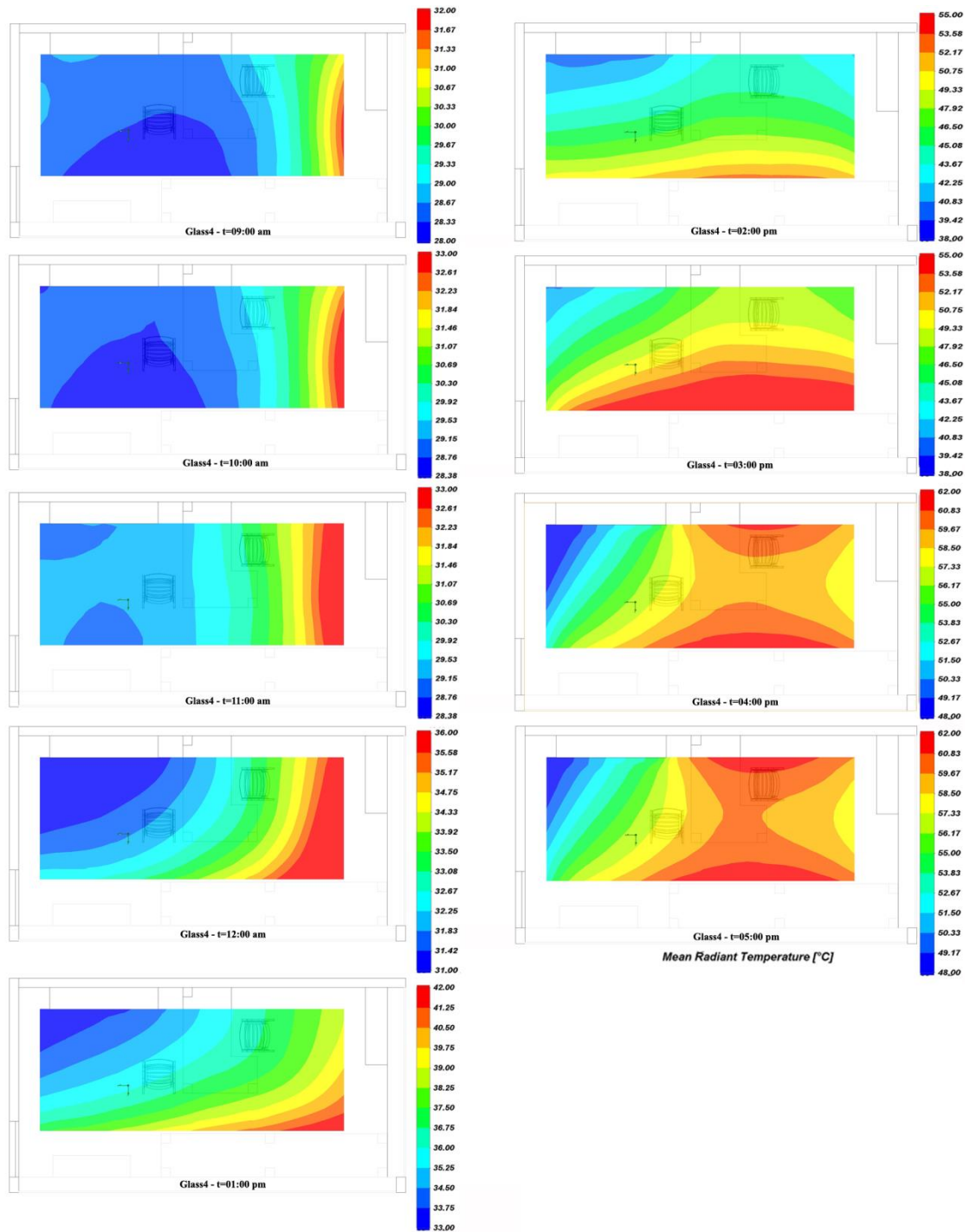


Figure 4.2 Mean radiant temperature distribution with “Glass 3 and new diffuser” from 09:00 to 17:00 on cross-sectional view at the height of 1.8 m.

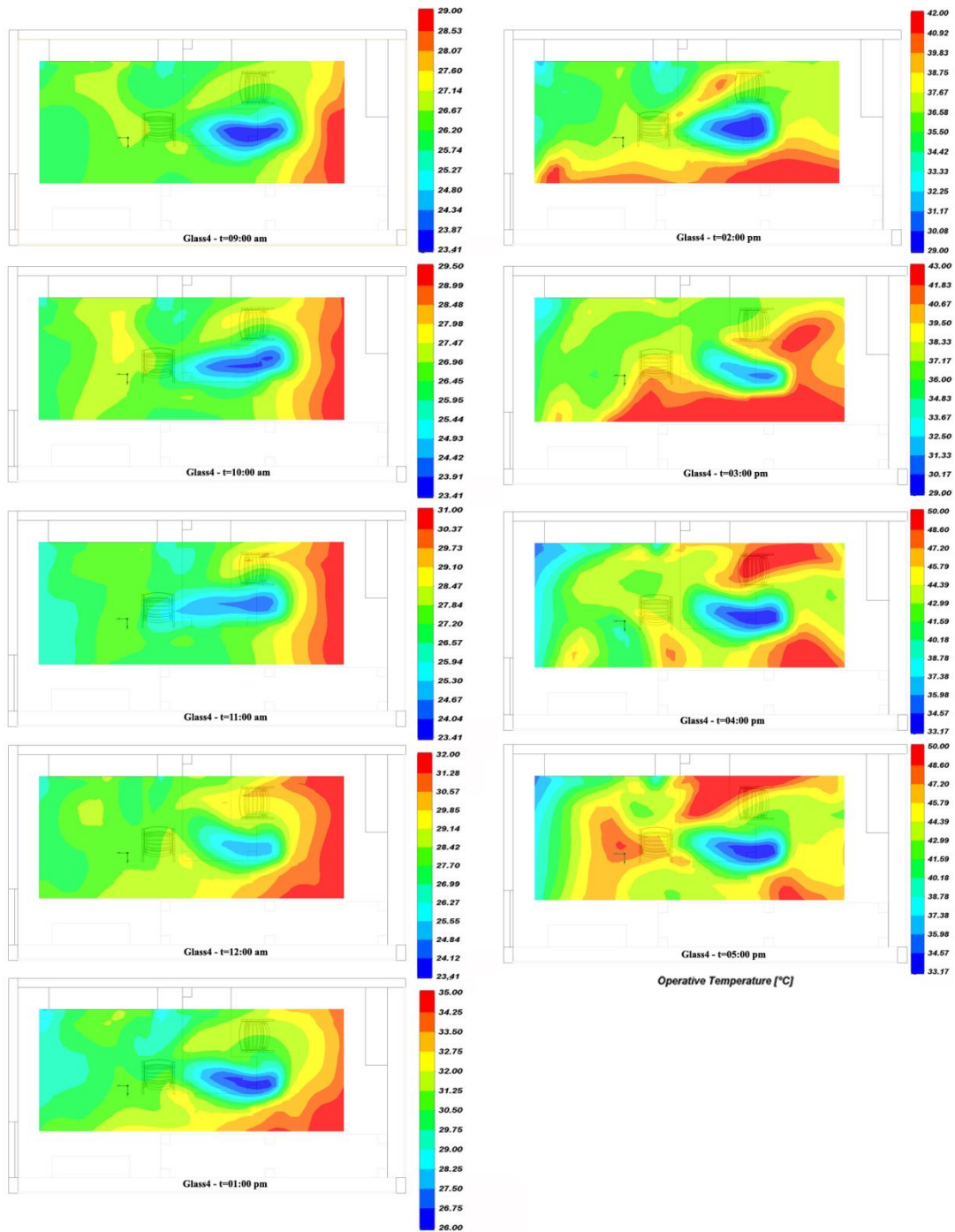


Figure 4.3 Operative temperature distribution with “Glass 3 and new diffuser” from 09:00 to 17:00 on cross-section view at the height of 1.8 m.

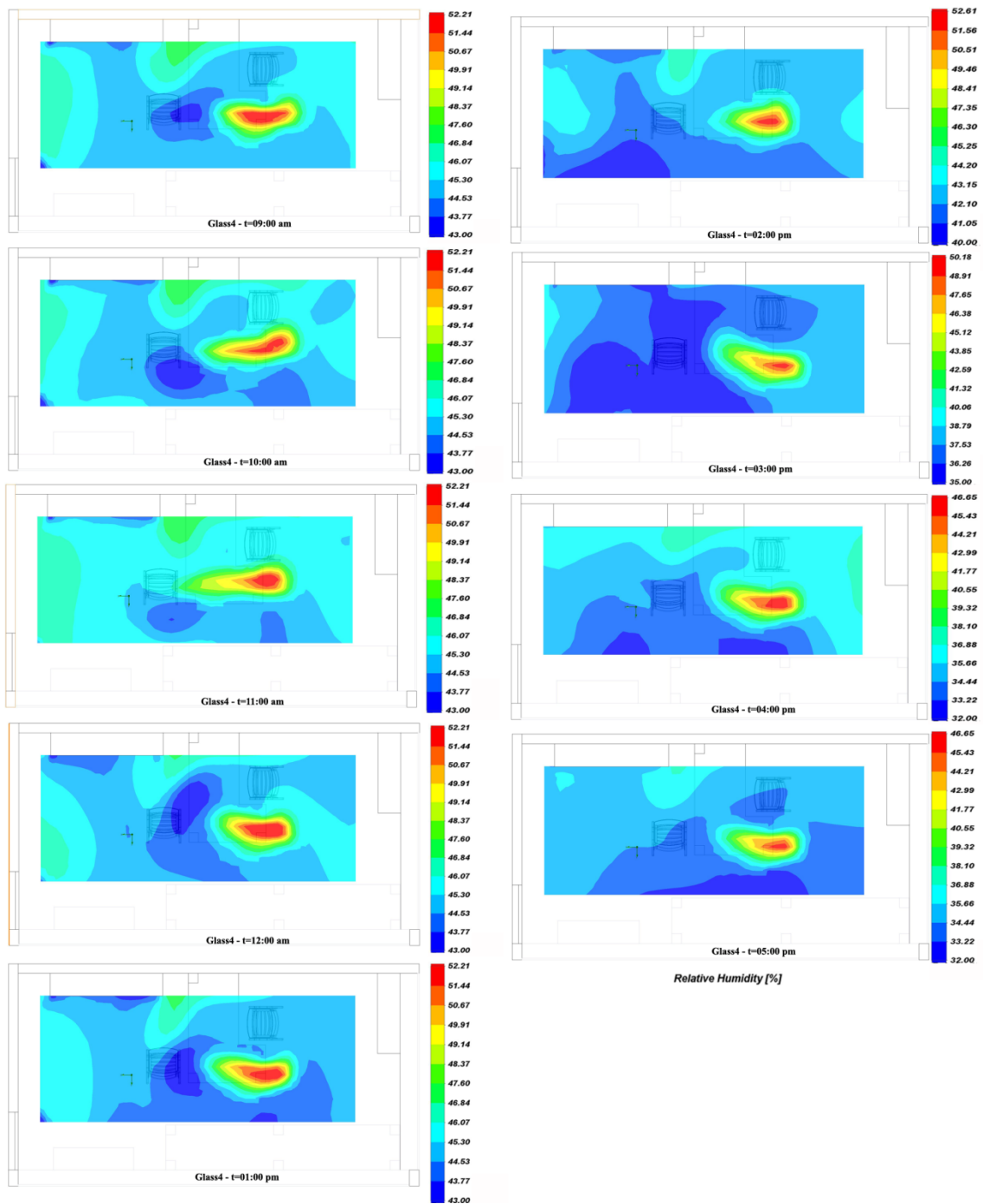


Figure 4.4 Relative humidity distribution with “Glass 3 and new diffuser” from 09:00 to 17:00 on cross-sectional view at the height of 1.8 m.

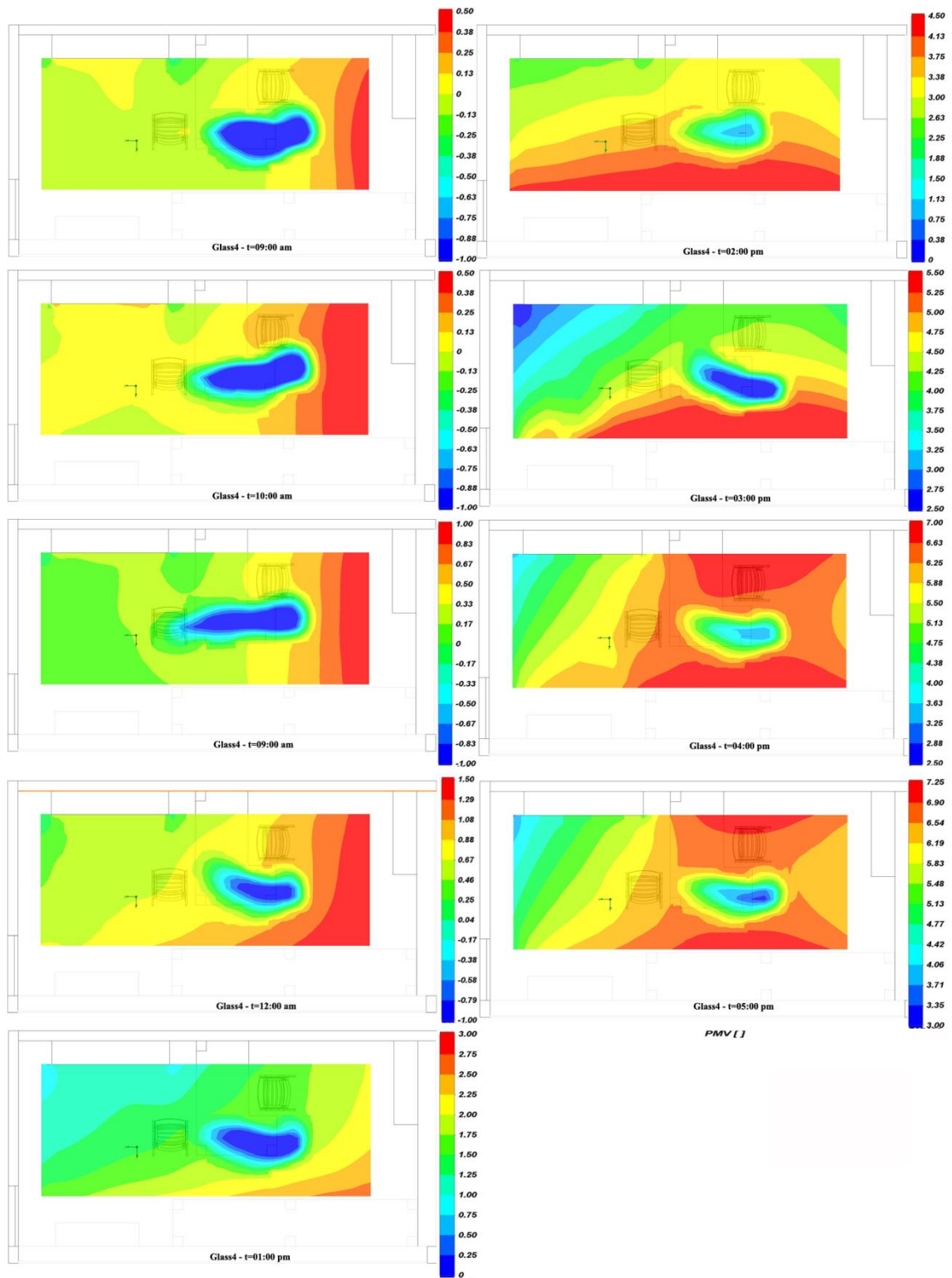


Figure 4.5 Predicted mean vote distribution with “Glass 3 and new diffuser” from 09:00 to 17:00 on cross-sectional view at the height of 1.8 m.

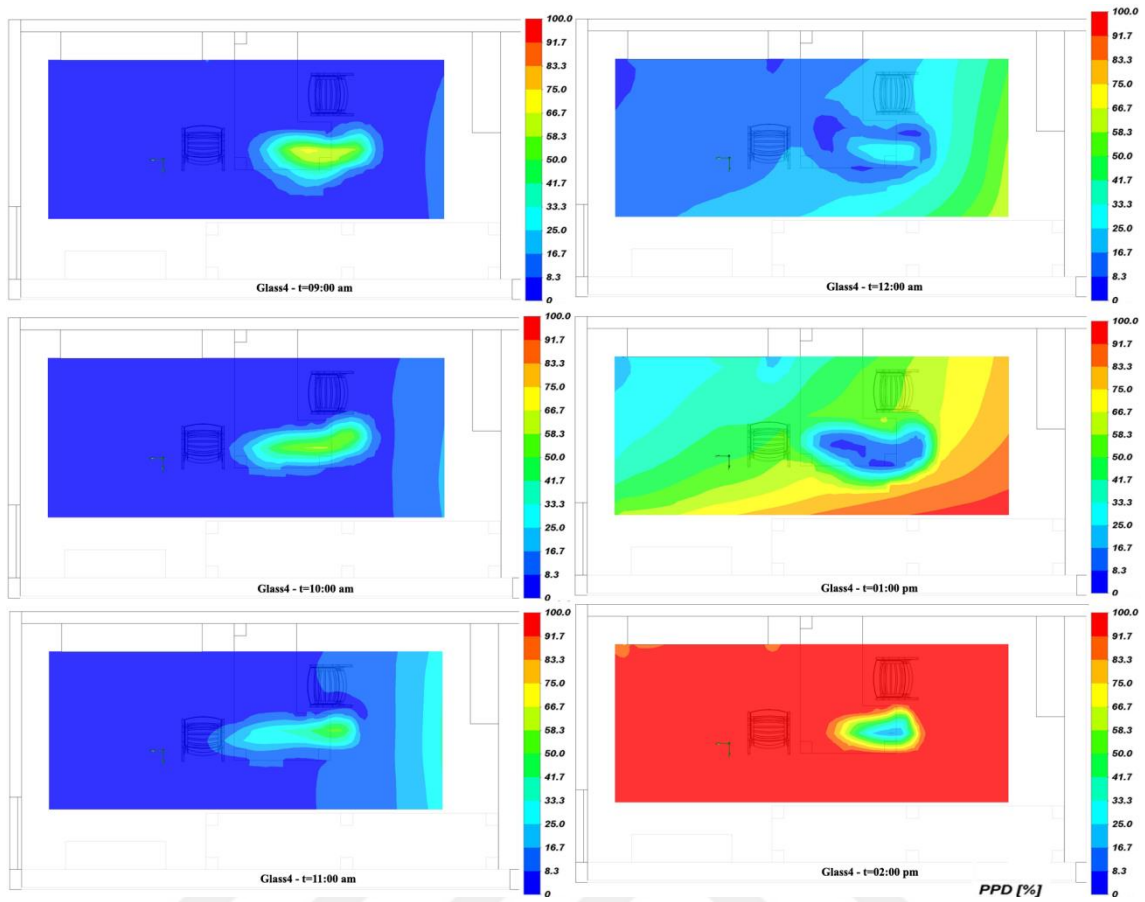


Figure 4.6 Predicted percent dissatisfied distribution with “Glass 3 and new diffuser” from 09:00 to 14:00 on cross-sectional view at the height of 1.8 m.